TECHNISCHE UNIVERSITÄT MÜNCHEN

Lehrstuhl für Halbleitertechnologie

Walter Schottky Institut

Multi-Alloy Structures for Injectorless Quantum Cascade Lasers

Casimir Richard Simeon Katz

Vollständiger Abdruck der von der Fakultät für Elektrotechnik und Informationstechnik der Technischen Universität München zur Erlangung des akademischen Grades eines

Doktor-Ingenieurs

genehmigten Dissertation.

Vorsitzender:	Univ.-Prof. Dr. E. Biebl
Prüfer der Dissertation:	1. Univ.-Prof. Dr. M.-Chr. Amann
	2. Univ.-Prof. P. Lugli, Ph.D.

Die Dissertation wurde am 04.03.2010 bei der Technischen Universität München eingereicht und durch die Fakultät für Elektrotechnik und Informationstechnik am 24.11.2010 angenommen.

Index

Abstract

Since the first realization of quantum cascade lasers in 1994, they have been steadily improved and reach more than 3 W continuous-wave output power at room temperature. Nearly all devices today use an intermediate superlattice, which creates an artificial miniband for moderating the electron injection. This injector was necessary for the first successful devices, as all concepts without had failed. The original concept, as suggested by Suris and Kazarinov, discards this injector and requires direct injection of electrons from the ground state into the subsequent upper laser level, and is therefore called injectorless. With this more compact design, the gain and the slope efficiency can be strongly improved, although the complexity of designs increases.

This work continues the successful work of the previous doctoral candidates G. Scarpa and A. Friedrich, who developed very good pulsed injectorless devices, with pulsed threshold current densities of 0.73 kA/cm² and threshold power densities of 70 MW/cm^3 at room temperature for an emission wavelength of 6.8 µm. Samples with higher threshold current density reached pulsed optical output powers of 240 mW, yielding an overall efficiency of 2.4 %. Devices with shorter wavelengths achieved pulsed threshold current densities of 2.75 kA/cm^2 at 5.8 µm and more than 3 kA/cm^2 at 4.6 µm, as high electric fields decrease the performance. At 7.9 µm the best pulsed threshold current density was found to be 2.4 kA/cm^2 at 300 K.

As all of the previous designs only used the two alloys $Al_xIn_{1-x}As$ and $Ga_xIn_{1-x}As$, with the exception of AlAs enhanced barriers, the concept of structures using multiple materials was the starting idea of this thesis. Using more than two alloys for the design increases the degree of freedom and should therefore lead to an improvement in performance. Similar approaches with injectorbased devices could improve neither threshold current density nor output power performance.

With the full range of materials in the AlGaInAs system being in consideration, the complexity in design strongly increases and the growth becomes more challenging. Therefore the first goal of this thesis was the development of an algorithm for optimizing the designs, which have a degree of freedom equal to twice the number of layers, as each layer can have a variable thickness and a variable composition.

The only suitable solution was found in applying an evolutionary algorithm in combination with a quick evaluation of structures using the one-dimensional Schrödinger equation and neglecting the Poisson equation. The possible freedom of material choice was limited by the capabilities of the molecular beam epitaxy. As flux rates cannot be changed during the active region growth and strain compensation had to be maintained, the number of materials dependents on the number of material cells inside the growth chamber. Therefore the material system had to be reduced to the following five compositions: AlAs, $Al_{0.635}In_{0.365}As$, $Al_{0.16}Ga_{0.31}In_{0.56}As$, $Ga_{0.4}In_{0.6}As$ and InAs. While AlAs enhances barriers to decrease losses and suppress leakage paths, InAs can be used not only for strain compensation but also for improved optical transitions, due to its low effective in-plane mass.

Using this new approach, a design with InAs enhanced active well was developed for an emission wavelength of 6.96 µm. Using the same waveguide, number of stages and doping levels as in the previously best performing injectorless device, a world record low threshold current densities of 0.57 kA/cm^2 and threshold power densities of 54 MW/cm^3 in pulsed operation was achieved. Devices with high reflective coatings reached values of 0.45 kA/cm^2 and 38 MW/cm^3, respectively. Although being low doped, the optical output power reached 240 mW with an overall efficiency of 3.7 %. And the maximum temperature of operation was increased from 340 K to 410 K at this low doping level by improving the characteristic temperature from 90 K to 150 K.

For further improving the output performance the design of short wavelength devices was considered, using more InAs enhanced optical transitions. The emission energy of injectorless devices is directly dependent to the applied electric field, as no intermediate section can be used to regain the transition energy between two transitions. Because of larger fields and strain issues for very short wavelength devices, the best performance was not achieved at 4.6 µm, as injectorbased devices do, but at 5.6 µm. The devices produced more than 1.3 W of optical output power, corresponding to an overall efficiency of 7.1 %. The threshold current density was found to be 1.1 kA/cm^2 at 300 K, which shows a strong improvement compared to previous injectorless short wavelength devices.

Besides these advances in threshold and output performance, the thermal management was investigated to achieve continuous wave operation. First, an ultra narrow stripe process was developed using a combination of dry and wet etching and combined silicon oxide and nitride passivation. Second, the setup technology was investigated regarding thermal resistances of different setups, as the setup can contributed between a factor 1.5 and more to the overall thermal resistance. The first devices, requiring more than 5 W of threshold power, yielded thermal resistances of 20-25 K/W, enabling only low temperature continuous wave operation. With advances in process, like reducing the mesa width from 10 µm to 4 µm and improving the lateral loss management, the threshold power got reduced to 3 W, enabling above room temperature continuous wave operation. The threshold current density was found to be relatively high with 2.4 kA/cm^2 at 293 K, due to the comparably large thermal resistance of 16 K/W. Further reduction of the overall thermal resistance down to 10 K/W, without using overgrowth techniques, improved the continuous wave operation at room temperature. The threshold current densities was measured as 1.76 kA/cm^2 at 293 K, while the output power was increased from 9 mW to 27 mW at 280 K.

Continuous wave operation of high performance designs enabled detailed measurements of gain spectra and gain coefficients. The Hakki-Paoli-method was applied, using a high resolution FTIR spectrometer, long focal length optics and a lasers operating in fundamental mode only. As expected, it could be proven that injectorless devices exhibit averaged gain coefficients by a factor of two larger than injectorbased devices. Besides their better performance, the complex gain current dependency was investigated, which is caused by the field current density dependence and field dependent lifetimes. Long resonators reach threshold before their applied internal field reaches the design field with the maximum gain. Shorter resonators, which exhibit higher losses, require larger current threshold current

densities, which push the field closer to the design field. This reduces leakage paths and increases also the relative inversion, which improves the gain coefficient itself.

For further improvements and a more efficient use of carriers, the injection behavior and tunneling lifetimes were investigated. The key idea was to increase the dynamic current range, defined by the threshold current density and the current density of the negative differential roll-over, which should increase the output power. Increasing the doping is the simplest method for improving the negative differential current density, but also induces larger waveguide loss and smaller slope efficiency. Alternatively one can decrease the lifetime on all states but the upper laser level to increase the maximum current for a given doping. Unfortunately, the quality of the optical transition, the different loss mechanisms of carriers and the transit time are all design dependent and strongly affiliated with each other. Therefore the main goal was to increase the maximum current density without decreasing the laser performance. This was achieved by increasing the coupling energy between the ground state and the following upper laser level from 5 meV to 10 meV, while keeping other parameters of the design identical. A stronger coupling should decrease the transit time between the lower laser level and the subsequent upper laser level for electrons, resulting in a larger dynamic range. The threshold performance and slope efficiency were maintained, while the transit time for carriers under lasing operation was reduced from 3.0 ps to 2.4 ps, increasing the overall efficiency from 3.7 % to 5.1 %.

When comparing injectorless devices with two alloys and multiple alloys, a significant performance improvement was achieved. The threshold current and power density reached record low values while the output power became comparable to injectorbased devices.

Introduction to Quantum Cascade Lasers

With the discovery and possible control of electromagnetic waves, many different applications were prospective and developed, and today every modern society is relying on it. At the low frequency side, the development of electronics enabled radio, radar and most communication systems. On the optic side with its high frequencies, there have always been classical full radiators, which have a broad spectrum, but also emitters with a discrete spectrum, like gas discharge lamps. All of these emitters have been using spontaneous emission, until 1955 the first demonstration of stimulated emission within the microwave regime was accomplished by Townes et al. [Gor55]. Five years later the first stimulated emission in the optical range had been demonstrated by Maiman [Mai60], giving birth to the era of light amplification by stimulated emission radiation, also called *LASER*.

The working principle of lasers, requiring a gain exhibiting material, achieved by carrier inversion, and an optical resonator for feedback, offered multiple device principles in which it could be applied. From 1960 onwards, it quickly spread to gas lasers, with HeNe as first demonstration [Jav61], liquid phase lasers [Sch66] and semiconductor lasers, with its first coherent emission in 1962 [Hal62]. In 1977, the first double heterostructure laser, using quantization effects, was realized [Rez77]. The light emitting transition occurred between a confined state in the conduction band and another confined state in the valence band. Figure 1-1 shows a large range of electromagnetic wavelengths and the corresponding devices.

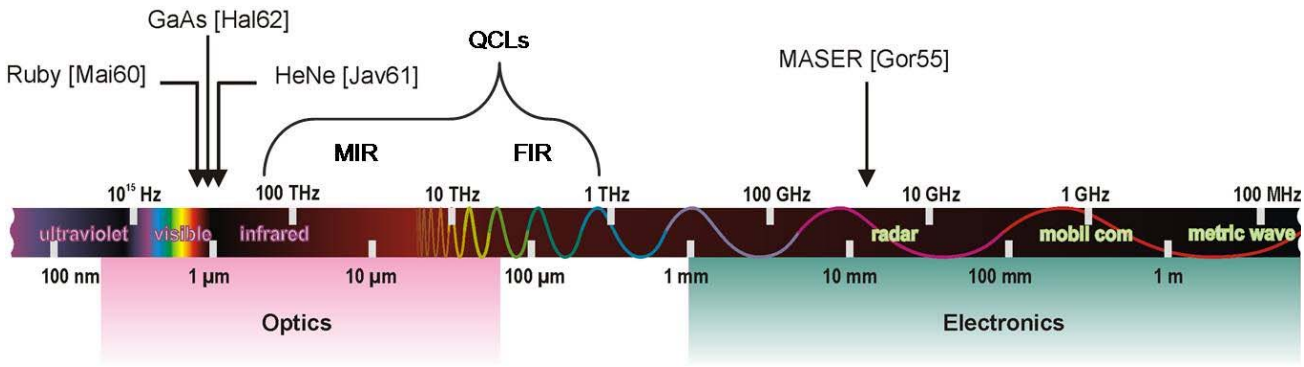

Fig 1-1: spectrum of electromagnetic waves from electronics towards optics. Arrows indicate the emission wavelengths of the first MASER and LASERs, while a curly brace indicates the two decades quantum cascade lasers can access today.

Later, in 1970, Esaki and Tsu discovered the negative differential resistance within a semiconductor superlattice structure [Esa70], leading to tunneling diodes [Cha74]. In 1971, Suris and Kazarinov suggested to use intersubband transition between two confined states of the same band [Kaz71]. Alternating materials, also called superlattice, should result into these confined states, which are more dependent on the well and barrier thickness than the actual material properties. The key

difference, in comparison to all other laser types, is the material independence, which allows quantum cascade lasers (*QCL*) to access a wide wavelength range from 2.75 µm [Dev07b] to 250 µm [Wal07].

Applications for lasers

Lasers in general enabled multiple applications from consumer electronics to military engineering. And every application has different laser requirements, regarding emission wavelength, output power, power consumption, price, stability, single mode operation, lifetime and device size, just to name the most important ones. In Table 1.1 different application regimes and their main criteria are shown.

application	main criteria	possible laser types
consumer electronics (i.e. DVD,Printers,LAN)	price, lifetime, size (power consumption)	diode laser
telecommunication (i.e. Internet, Free Space)	wavelength, single mode operation, lifetime, price	diode laser
material processing (i.e. welding, cutting)	output power, lifetime, size (power consumption)	CO_2-laser, Nd:YAG diode laser
controlling & positioning (i.e. LIDAR, gyroscope)	single mode operation, stability, price (strongly depending on application)	diode laser
military technology (i.e. marking, blinding)	output power, device size lifetime, wavelength	chemical laser, diode laser quantum cascade laser
spectroscopy & sensor technology (i.e. materials & human analysis)	wavelength, single mode operation (device size, power consumption)	quantum cascade laser diode laser

Tab 1.1: applications and their main criteria's and possible laser solutions

When looking for applications for quantum cascade lasers, their fundamental limitations should be considered. Intersubband transitions result into shorter lifetimes (for details see chapter 2.1), which reduce the performance and output power on one side. On the other side, the emission wavelength is much more dependent on the growth parameters compared to interband diode lasers, making it harder to hit a specific wavelength. Both of these issues increase the price per device drastically, although quantum cascade lasers are semiconductor based devices. The high price and the complexity of design, render them unprofitable for consumer electronics and simple controlling systems, while most material processing applications require higher efficiencies and output powers. Their main advantage is found in the wide wavelength range they can access, as no bulk material has stable interband transitions within a few meV or tenths of meV. Additionally many important fundamental vibration modes lie in the mid and far infrared (*THz* or *FIR*) range, offering the highest absorption coefficients and therefore the best detectivity [Kos02][Lew09]. It is possible to sense warfare agents and explosives and distinguish between them with quantum cascade laser arrays [Pat08] as well as atmospheric investigations, [Nel08]

which are sensitive enough for isotopic ratio detection. The far infrared wavelengths also enable, in combination with the detection of large molecules like drugs and explosives, the scanning of parcels, suspects and other soft targets [Lee06a][Lee06b]. This is a result of terahertz waves being able to penetrate biological materials without ionization effects unlike Xrays, while getting reflected from metals and ceramics. These properties have raised lately massive interest for security, military and medical applications [Bak07][Loe07][Lam08], although some severe issues have to be overcome, like weak output powers and strong atmospheric absorptions [App07] with at least a few dB/km and up to 1000 dB/km attenuations. Still the prospects for the future are optimistic on the potential of these new sources. Investigations of human breath, revealing diseases by trace gasses, are already in clinical trials [Sho10]. Figure 1-2 shows some absorption spectra for three different gases and retinoic acid, an important biological molecule. The highest absorption coefficients for the most common molecules can be found in the mid infrared above 4 µm (below 2500 cm^{-1}).

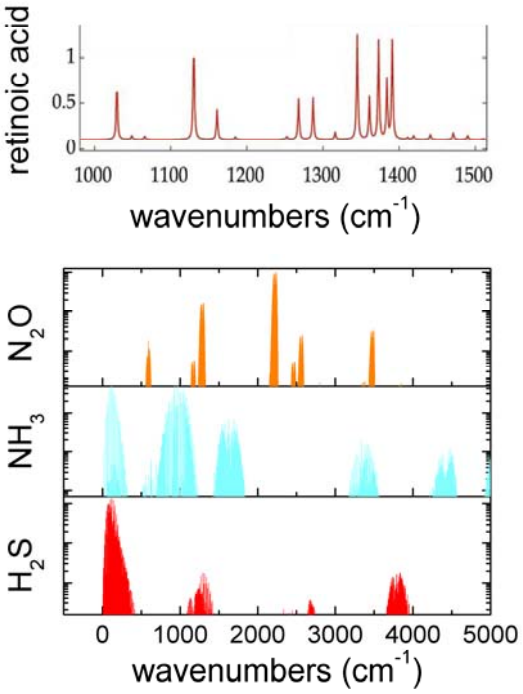

Fig 1-2: absorption spectra of H_2S, NH_3 and N_2O (bottom) for the mid and far infrared wavelength range in logarithmic scale. A focus of the 6.7 to 10 µm range and the corresponding absorption for retinoic acid is shown above [Wit07].

Besides the very sensitive spectroscopic applications, mid infrared quantum cascade lasers can be used for free space optical communications. Their key advantages are the much lower absorptions regarding fog, dust and particles [Mar05] in combination with their high modulation frequencies due to much lower carrier lifetimes. In clear air, the attenuation can be as low as 0.05 dB/km [App07], which is lower than regular 1.55 µm fibers exhibit.

It has to be mentioned finally, that most commercial revenue is currently made with military applications, which are using the high powers in the mid infrared range for directional infrared countermeasures against incoming surface-air missiles or as portable target illuminators [Pat09]. Both of these applications require only large output powers without single mode operation at the mid infrared. Lifetime and device size play a much larger role than price.

Operation principles of quantum cascade lasers

At this point, it is worth highlighting the differences between classical lasers and quantum cascade lasers and their principle of operation. Figure 1-3 shows the main difference between an

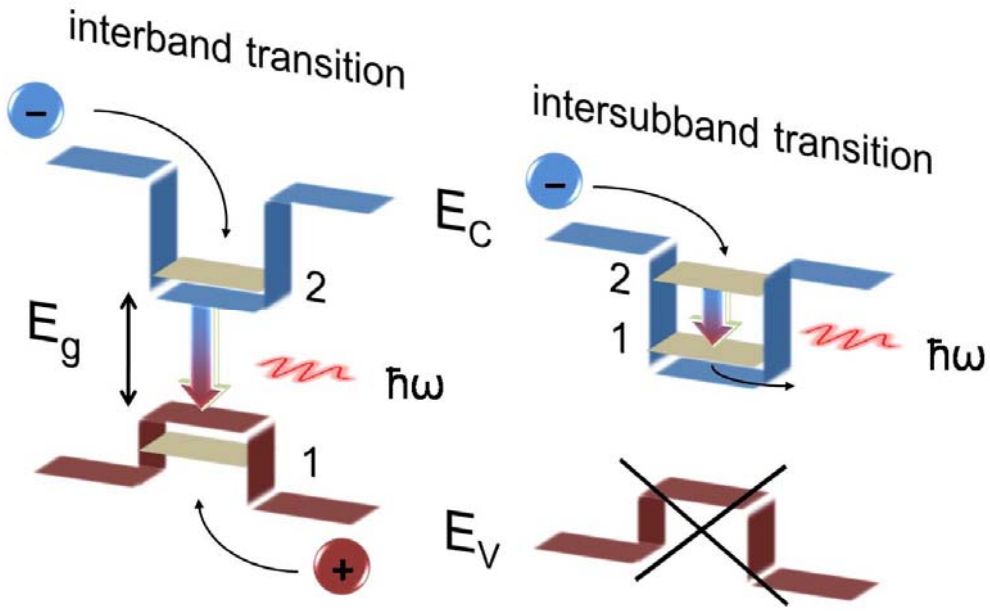

Fig 1-3: interband transition (left) and intersubband transition (right). E_V and E_C indicate the valence band and the conduction band, respectively

interband transition (left) and an intersubband transition (right). While the emission energy of the interband transition depends on the band gap and the confinement energies of the electrons and holes, it is only confinement dependent for the intersubband transition. Additionally only one type of carrier, in most cases electrons, is required for operating the device, which is therefore called unipolar. Without the band gap, nearly all transition energies are achievable, from very small ones (few meV depending on line width) up to an eV, depending on the conduction band offset between the two materials.

The main problem, which stalled the successful demonstration of quantum cascade lasers, were the complex scattering processes, which prevented most initial concepts from operation. These problems were overcome by Capasso and his co-workers only in 1994 [Fai94]. And a key advantage of using only one type of carrier comes into play now, the cascading of transitions, as the carriers are kept inside the conduction band and only have to regain sufficient energy for another transition.

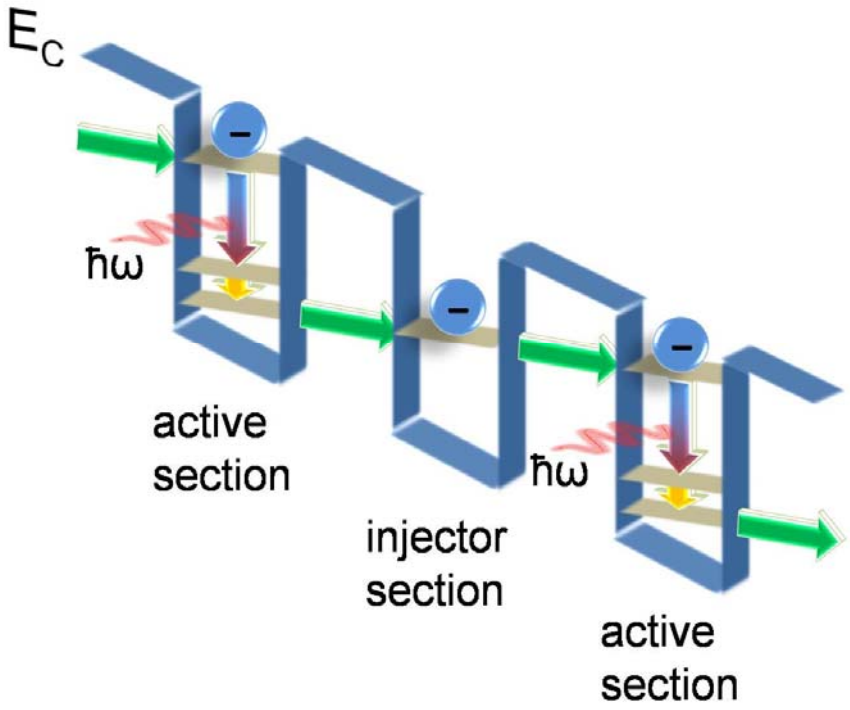

Fig 1-4: principle of a quantum cascade, with the optical transition indicated by a blue-red arrow, the fast resonant phonon scattering by an orange arrow and the tunneling transport by a green arrow. The tilt of the conduction band corresponds to the applied field.

Figure 1-4 shows the cascading principle of the intersubband laser, which allows the carrier to regain its transition energy over some intermediate states by tunneling and low energy scattering mechanisms and finally being reinjected into another upper laser state. This intermediate section, which is called injector, is designed as energetic miniband by using many coupled quantum wells. This injector was also a main factor, which helped the first lasers to operate, although it is not necessarily required as injectorless designs have showed [Wan01].

From the electronic device point, quantum cascade lasers behave similar to rapid tunneling diodes, as their injection mechanism is based on tunneling. Both devices have a maximum current density at the design field, which is indirect proportional to the overall transition time per period. When increasing the current density above this limit, the energy states jump towards a higher electric field, suitable to this larger current density, causing a negative differential resistance and stopping the device from lasing.

Besides these differences in gain design and electrical behavior, the optical resonator and the thermal management are similar to regular diode lasers with some exceptions. The long wavelengths cause higher absorption losses and require thicker guiding layers, while the thermal resistance is larger because of the micrometer thick superlattice structure of alternating ternary materials. This leads back to the question of advantages over other laser systems and possible applications, to justify the research efforts into these complicated devices.

State of the art devices at the beginning of this thesis

At the beginning of 2007, the mid infrared quantum cascade lasers have matured to devices ready for applications. Concepts from classical diode lasers have been transferred to quantum cascade lasers like distributed feedback and facet coatings, offering single mode operation with 100 mW of power for a wide wavelength range [Dar06]. The wall plug efficiency, being the ratio of output power divided by overall input power, reached 9.3 % [Eva07] for short wavelength devices around 4.6 µm. This followed the model of J. Faist [Fai07], which proposes that the maximum achievable efficiency is indirect proportional to the wavelength for quantum cascade lasers. For the common injector based devices the best threshold current densities, which are the result of good optical and electrical design, had reached a pulsed room temperature threshold current density of 0.73 kA/cm^2, using high-reflectivity coatings [Sliv07]. All of this performance improvements were achieved by optimization of the injector and active region designs as well as waveguide improvements and implementation of overgrowths for heat removal.

None of these changes touched the design principle in general for very good reasons. The injector states were the key to success in 1994, after many years of failure. They offered a good control over the injection efficiency and stability of current flow, as well as providing space for the electrons to regain their transition energy. Although they are passive and don't contribute to the gain, they were kept with the exception of some early try to remove them [Wan01], which failed as the device performance was very weak even in comparison to that time.

In 2004, research on injectorless devices was revived by the previous PhD student A. Friedrich, in collaboration with G. Scarpa, who started the quantum cascade laser research at the Walter-Schottky Institute. Injectorless devices could assumable exceed the performance of injector based devices, due to a more compact stacking of optical transitions and faster transit times. And in 2005, the first pulsed operation of an injectorless device at room temperature was demonstrated [Fri05] with still a very high threshold current density of 7.1 kA/cm^2. Additional improvements enabled finally to catch up in terms of threshold current density by the end of 2006, with a threshold current density of 0.73 kA/cm^2 for an uncoated device operating at 300 K [Fri06]. The optical power of these devices, in contradiction to the good threshold, was weak with 70 mW. And even higher doped devices only increased to 240 mW and 0.83 % overall efficiency, in comparison to devices which achieved 200 mW and 2.5 % overall efficiency in continuous wave operation at even longer wavelengths (8.4 µm) [Die06].

It has to be mentioned, that research on injector based device is much more intense and ongoing for 15 years now, while injectorless devices were left aside, although they are closer to the original suggestion of Suris and Kazarinov [Kaz71]. Only recently a few more groups have joined this field [Dey09][Hsu09] besides the Walter-Schottky Institute.

Focus of this thesis

The general field of this thesis was *"multialloy structures for injectorless quantum cascade lasers",* a very wide topic with endless possibilities. The term multialloy refers to the conduction band of quantum cascade lasers, which were mostly using only two material alloys. Some research was done by different groups on using more than two material compositions [Yan05][Sem06], while preliminary work on AlAs enhanced barriers was done at the WSI by A. Friedrich [Fri07]. None really improved the performance beyond the classical two alloy designs, with the work of Faist and coworkers achieving 1.65 kA/cm^2 and 200 mW of output power in pulsed operation at least [Vit07].

When using more material alloys, an additional degree of freedom within the designs is gained, theoretically enabling increased performance with lower threshold current densities and higher output efficiencies. Additionally the design and growth become more complex and have to be investigated and controlled.

- **Main topic:**
  Injectorless devices using multiple alloys with improved threshold and output performance

This main topic covers the research on materials and development of a suitable design optimization algorithm. Also the growth reproducibility and variance have to be taken into account. Besides the research within active region designs, room temperature continuous wave operation should be achieved and demonstrated, as up to 2007 all injectorless devices were only working in pulsed operation. The pulsed only operation started discussions at various conferences whether the short transient time and the reduced number of states could prevent these devices from stable continuous wave operation.

- **Side topic:**
  Continuous wave operation of injectorless devices at room temperature

In the next chapter, the theory regarding electrical, optical and thermal design will be explained in detail, combined with examples. The third chapter is focused on the growth, the processing, the setup and the device characterization, while the fourth chapter contains the results and corresponding discussion to the previously mentioned main and side topic. Subchapter 4.1 focuses on low threshold current devices, 4.2 is covering the work on continuous wave devices and 4.3 is presenting the results on the high-performance devices. Subchapter 4.4 summarizes the general research on injection behavior and current field dependencies, which was necessary to fully understand the devices and improve them.

Theory and Design of Injectorless Quantum Cascade Lasers

This chapter was written to describe the physics behind the devices, required for designing a suitable laser structure. In a general view, the concept of a quantum cascade laser can be separated into three different domains: the electrical, the optical and the thermal domain. These domains have to be optimized all together for a perfect performance, unfortunately they are coupled to some degree (see figure 2-1-1). A suitable band design has to be found for achieving high laser gain within the active region in the electrical domain. This band structure design includes the confined states, the scattering rates and possible laser transitions but also the intersubband absorption. Additionally the electrical domain has to be optimized for low serial resistances and good ohmic contacts. Good electrical performance always requires a high doping in this case, which directly affects waveguide losses and therefore threshold current density and output power. The optical domain involves the wave guiding and resonator design, including internal losses and mirror losses but also output power and overall efficiencies. Under pulsed operation the thermal domain is neglected, as long as the device is operated with low duty cycles. For continuous-wave (cw) operation the thermal domain, especially choice of materials but also setup technology has to be considered. The schematic in figure 2-1-1 should give an impression about the coupled problems, which are discussed in detail within the following subchapters and in each material section. The schematics are by no means complete, but for visibility kept simple.

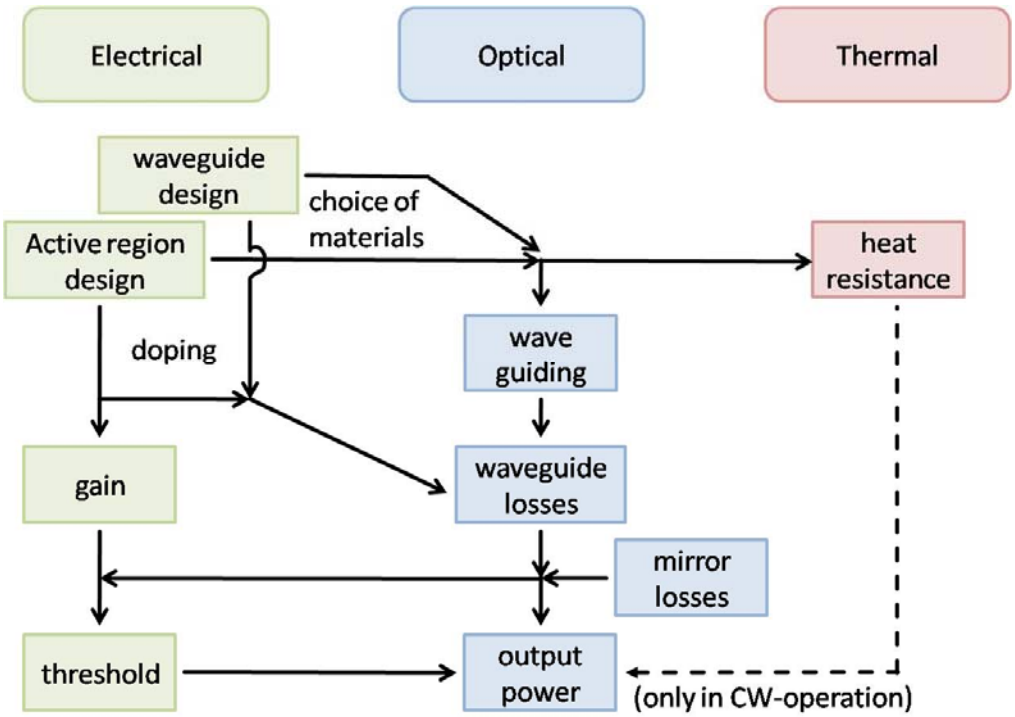

Fig 2-1-1: Schematics of electrical, optical and thermal domain within a quantum cascade laser design

All sub chapters are divided into a first part, in which the general theory necessary for understanding the problem is described, and a second part explaining possible materials and design approaches for different emission wavelengths. The focus of this work is the improvement of mid infrared devices based on AlGaInAs/InP using more than two alloys.

2.1 Electrical Model and Theory

When designing a quantum cascade laser, the general principles and design rules of a laser have to be combined with the quantum mechanics theory of energy eigenvalues, confined states and charge transport within a superlattice. The electrical model describes the pump scheme and when applying rate equations, allows deriving the gain coefficient. The gain coefficient determines the threshold condition in combination with the optical losses as following:

$$g_c \cdot \Gamma \cdot \mathrm{j_{th}} = \alpha_i + \frac{1}{L}\ln\left(\frac{1}{R}\right) \tag{2.1.1}$$

with g_c being the material dependent gain coefficient, Γ the confinement factor of the electromagnetic radiation within the uniformly excited region [CasH89] and j_{th} the threshold current density. The right side of the equation is representing the losses of the device with α_i being the internal losses and the mirror losses α_m given by (1/L)·ln(1/R). As the losses are mostly waveguide dependent, except for the intersubband absorption, they are treated within subchapter 2.4.5.

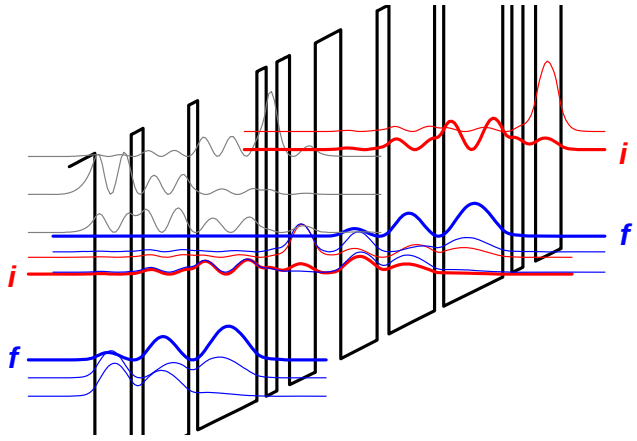

Fig 2-1-2: squared wavefunctions of two sequenced stages, f indicating the final and i the initial state of the optical transition

Every laser needs a medium which exhibits gain. In the case of quantum cascade lasers, the gain is created by stimulated emission between two different confined states in the same conduction band (see equation 2.1.6 & 7). This is indicated in figure 2-1-2 with the initial and the final state of the transition (*i* and *f*) while the other lower blue states are used for fast depletion by optical phonon scattering (see electron-phonon scattering) and the resonance for an efficient injection (see interface defect scattering). Rate equations can be applied on this simple energy level system, as done by Gorfinkel et al. [Gor96][Sca02], yielding the following equations:

$$\frac{\partial n_i}{\partial t} = \frac{j}{e} - \frac{n_i}{\tau_i} - \sigma_c\left(n_i - n_f\right)\bar{c}\Gamma \cdot \mathrm{S} \tag{2.1.2a}$$

$$\frac{\partial n_f}{\partial t} = \frac{n_i}{\tau_{if}} + \sigma_c\left(n_i - n_f\right)\bar{c}\Gamma \cdot \mathrm{S} - \frac{n_f}{\tau_f} + f\left(n_f, n_0, \Delta E, \vec{E}, T\right) \tag{2.1.2b}$$

$$\frac{\partial S}{\partial t} = \sigma_c\left(n_i - n_f\right)\bar{c}\Gamma \cdot S - \alpha_{tot}\bar{c} \cdot S \tag{2.1.2c}$$

with $n_{i,f,0}$ being the carrier densities of the initial, the final and the ground states. S is used as the photon density, while $\tau_{i,f,if}$ is representing the overall life time of the initial state, the overall lifetime of the final state and the transition time between the initial and the final state. $\bar{c}$ is determining the speed of light divided by the effective refractive index, α_{tot} are the total waveguide losses, similar to the right side of equation 2.1.1 and σ_c is representing the gain cross section coefficient. The function $f\left(n_f, n_0, \Delta E, \vec{E}, T\right)$ represents the effects of thermal backfilling from carriers of the ground states into the lower laser state, which is dependent on the temperature, the applied field and the energy separation of the actual states.

A steady state solution of the rate equations (equation 2.1.2a-c) can be found for the photons, which yields

$$S = \frac{1}{\sigma_c \cdot \alpha_{tot} \cdot \bar{c} \cdot \left[1 + \frac{\tau_f}{\tau_i} - \frac{\tau_f}{\tau_{if}}\right]} \cdot \left[\frac{\sigma_c}{e}\Gamma \cdot j\left(1 - \frac{\tau_f}{\tau_{if}}\right) - \frac{\alpha_{tot}}{\tau_i}\right] \geq 0 \tag{2.1.3}$$

neglecting the function of thermal backfilling. The number of photons has to be larger than zero above threshold, which leads to the threshold condition

$$\frac{\sigma_c}{e}\Gamma \cdot j\left(1 - \frac{\tau_f}{\tau_{if}}\right)\tau_i = \alpha_{tot} \tag{2.1.3b}.$$

When introducing the gain coefficient g_c with

$$g_c = \frac{\sigma_c}{e}\left(1 - \frac{\tau_f}{\tau_{if}}\right)\tau_i \tag{2.1.3c}$$

the threshold condition of equation 2.1.1 is derived. The following subchapters explain in details how the gain coefficient g_c can be calculated from a given conduction band structure and, maybe even more important, how a good design can be found.

For finding the proper superlattice design, one can follow different approaches, like the very complex and time consuming non-equilibrium green functions approach [Lee02] [Yas09] [Kub09]. It is suitable for taking multiple scattering processes (see scattering processes) into account like acoustical and optical phonons, impurity and interface defects, electron-electron scattering and even dephasing. Including the k-dispersion relation and thermal excitation, it is even possible to calculate populations and therefore gain and losses over the required energy range. On the other hand a single field step for a given design takes roughly two hours on a fast computer, leading to a day or more for a single structure and the necessary field sweep: Far too long for designing new structures, but good for analyzing working devices. Another approach is based on the monte-carlo method [Com02] which takes electron-electron and electron-phonon scattering into account and performs a simulation over many carriers by probability, ending up in a steady distribution of carriers yielding gain and line width. The time for

performing a monte-carlo simulation also ranges in a few hours for a given structure and therefore a simpler solution had to be chosen. The 1-band Schrödinger equation is suitable for finding the energy eigenvalues of a given conduction band structure allowing an estimation of the transition energies. Additionally the complex wave functions can be used for calculating the lifetimes inside the structure, which will be used for gain approximation. This method is much simpler and faster, allowing a fast search for new designs, but falls short on its own simplicity in some cases, as population densities cannot be calculated.

2.1.1 Self-consistent Schrödinger equation in one dimension

When an electric field is applied to a conduction band structure, using different materials (see materials) and layer thicknesses, the solutions for the energy eigenvalues can be found by using the one dimensional Schrödinger equation for the envelope function $\varphi_n(x)$:

$$\left[-\frac{\hbar^2}{2}\frac{\partial}{\partial x}\left(\frac{1}{m_{eff}(x)}\frac{\partial}{\partial x}\right)+V_c(x)+V_{el}(x)\right]\cdot\varphi_n(x)=E_n\cdot\varphi_n(x) \tag{2.1.4}$$

With $m_{eff}(x)$ being the effective mass in the growth direction x, $V_c(x)$ is the conduction band profile, $V_{el}(x)$ is the contribution of the applied field and E_n is attributed to the energy of quantized electronic state. More details about the envelope function approach can be found in Appendix A auf G. Scarpa's PhD Thesis [Sca02].

As normal quantum cascade lasers are only confined within one dimension, in contrary to quantum dot lasers for example, the other two dimensions are described by the normal parabolic k-dispersion relation. Taking this dispersion into account is less important for mid infrared emission but vital for any emission energy below the longitudinal optical phonon energies.

In the confined direction, where electron states can reach higher energies levels, the so called non-parabolicity has to be taken into account. In other words, the deviation of the real conduction band from the parabolic approximation becomes significant. This is done by using an energy dependent mass $m(E)$ following

$$m(E)=m^*_{eff}(x)\cdot\left(1+\frac{E-E_c(x)}{E_{g,eff}(x)}\right) \tag{2.1.5}$$

with $E_c(x)$ being the conduction band energy and $E_{g,eff}(x)$ being the effective bandgap at a position x. With the equations 2.1.4 and 2.1.5 and the transfer matrix method it is possible to calculate the energy eigenvalues and the complex wave functions. These wave functions are required for analyzing the dipole matrix element and the lifetimes of the different energy states.

2.1.2 Intersubband material gain

The peak material gain g_p, the device comprises can be calculated by knowing the dipole matrix element z_{if} between the initial and the final state of the transition (see figure 2-1-2), the population inversion Δn as the difference of the carrier densities between the two states and the line width of the transition γ_{if}. This is can be written as

$$g_p = \frac{4\pi e^2}{\varepsilon_0 n \lambda} \cdot \frac{{z_{if}}^2}{2\gamma_{if} L_p} \cdot \Delta n \tag{2.1.6}$$

with λ being the transition wavelength, L_p the length of a single stage and n the refractive index [LuiC00]. The population inversion Δn can be extracted from the lifetimes and the injection efficiency η_i,. This leads to a gain coefficient g_c given by the formula:

$$g_c = \frac{4\pi e}{\varepsilon_0 n \lambda} \cdot \frac{{z_{if}}^2}{2\gamma_{if} L_p} \cdot \left(\eta_i \tau_i - \left(1 - \eta_i \left(1 - \frac{\tau_i}{\tau_{if}} \right) \right) \tau_f \right) \tag{2.1.7}$$

Most injection efficiencies for mid infrared devices are found to be between 70 % and 80 %, but can be much lower and strongly design and field dependent. As one tries to obtain maximum peak gain for best performance, the dipole matrix element and the upper laser state lifetime (τ_i) have to be maximized. The dipole matrix element, for the non orthogonal states, can be obtained by the formulae given in [Sir94] and transformed by Faist in [LuiC00] which reads as:

$$z_{if} = \frac{\hbar}{2(E_i - E_f)} \langle \varphi_i \left| p_x \frac{1}{m_{eff}(E_f, x)} + \frac{1}{m_{eff}(E_i, x)} p_x \right| \varphi_f \rangle \tag{2.1.8}$$

with p_x being the momentum operator $-j\hbar(\partial/\partial x)$ and normalized wave functions, according to

$$1 = \langle \varphi_i \left| 1 + \frac{E - V(x)}{E - V(x) + E_g(x)} \right| \varphi_i \rangle. \tag{2.1.8b}$$

Besides the dipole matrix element, the life times have to be well designed for achieving a sufficient population inversion. This requires a long life time of the upper laser state and a very fast depletion of the lower states. One of the fastest processes in intersubband transitions of higher energy (30 meV and more) is the electron-phonon scattering with *LO*-phonons. This is also the dominating process for the upper laser lifetime for mid infrared and one of the major limitations for far infrared designs. For smaller energies the electron-acoustical phonon and the interface defect scattering play an important role, both temperature dependent. These small energy transitions play an important part in the injection efficiency and the negative differential resistance.

2.1.3 Scattering by optical phonons

When considering scattering by optical phonons *(LO)* it is important to separate between transitions, exhibiting larger or low energy than the phonon energy. In general, larger energy separations are used for the optical transition in mid infrared devices, while lower energy separations for far infrared devices. In figure 2-1-3 it is illustrated with displaying the dispersion relation for two different transition energies. The transition for energies below the optical phonon energy also occurs in mid infrared devices within the depletion and injection states and can therefore influence the behavior of the device [Lya09][Viz09].

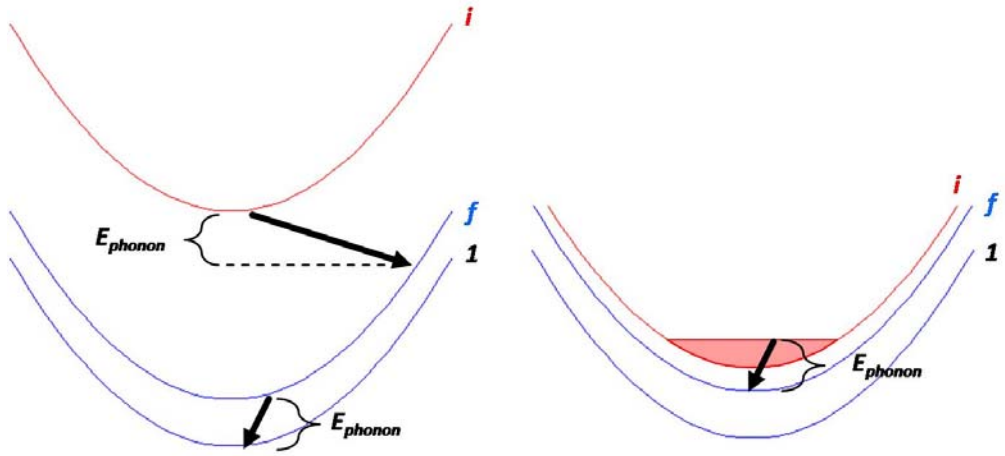

Fig 2-1-3: A three level systems for mid infrared transitions (left) and one for far infrared transitions (right). In both the initial (i), final (f) and ground state (1) are indicated. The right scheme can be also found in mid infrared devices which use asymmetric depletion schemes [Lya09][Viz09].

In the mid infrared design, the electron-optical phonon scattering takes place from all different levels. While the lower one is in resonance, yielding extremely short lifetimes, the upper one is much higher and therefore achieving higher lifetimes and a population inversion proportional to the injection current. In the far infrared design, the charges fill, assuming no scattering directly into the ground state takes place, the upper level until they reach resonance and define a maximum inversion possible. With higher temperatures this maximum inversion decreases, limiting the maximum temperature of operation to the phonon energy for far infrared devices. But in case of a non resonant depletion mechanism for mid infrared devices [Lya09][Viz09], it requires some thermal activation.

When estimating the electron-phonon scattering, we can follow the theory of G. Bastard and R. Ferreira [Fer89] and U. Bockelmann [Boc90]. By Fermi's golden rule we can calculate the lifetime for $k_{\parallel} = 0$ using

$$\frac{1}{\tau_{if,LO}} = \frac{m_{eff} \cdot e^2 \cdot \omega_{LO}}{2\hbar^2 \varepsilon_p q_{if}} \int dx \int dx' \varphi_i(x) \varphi_f(x) e^{-q_{if}(x-x')} \varphi_i(x') \varphi_f(x') \qquad (2.1.9)$$

with q_{if} being defined as

$$q_{if} = \sqrt{\frac{2m_{eff}(E_{if} - \hbar\omega_{LO})}{\hbar^2}} \qquad (2.1.9b)$$

with ω_{LO} being the phonon frequency of the material, normally the dominating branch in case of GaInAs. In figure 2-1-3 all different cases of electron-phonon scattering are displayed. The fastest scattering, which is used in both designs for depletion, is achieved when the lower laser state *(f)* and the ground state *(1)* are in resonance with the phonon energy. This process yields lifetimes as low as 0.2 ps. In case the transition energy E_{if} is larger than the phonon energy, the lifetime is monotonically increasing up to a few picoseconds with increasing separation, as a scattering phonon needs to carry a larger momentum. As the phonons follow the Bose-Einstein distribution, they are reducing the lifetime at higher temperatures given by

$$\tau_i(T) = \tau_i(0) \cdot \frac{1}{1+\frac{1}{\exp\left(\frac{\hbar\omega_{LO}}{k_B T}\right)-1}} \quad . \tag{2.1.10}$$

If the transition energy between the initial state *(i)* and the final state *(f)* is lower than the optical phonon energy, the carriers are filling the upper band, assuming no other scattering mechanism occurs, until they reach the phonon energy. At this point any additional carriers are scattered very fast as they are in resonance and the maximum inversion is reached. With increasing temperature and a thermal distribution, this maximum inversion is even reduced further more limiting the maximum temperature of operation. This problem is found in all far infrared devices and can only be overcome by using materials with either higher optical phonon energies or other means of suppressing the fast scattering process.

2.1.4 Scattering by acoustical phonons

For lower energies and higher temperatures the acoustical phonon *(LA)* scattering has to be taken into account, where it plays an important role for an efficient injection at room temperature. Similar to optical phonons, Fermi's golden rule and a first-order perturbation theory [Boc09] leads to

$$\frac{1}{\tau_{if,LA}} = \frac{2\pi}{\hbar}\sum_{f,q}\alpha(q)\left|\left\langle\varphi_i(x)\middle|e^{-jqx}\middle|\varphi_f(x)\right\rangle\right|^2 \times \delta\left(E_f - E_i + E_q\right)\cdot(1+n) \tag{2.1.11}$$

with q being the phonon wave vector and $\alpha(q)$ being the coupling factor of electrons to *LA*-phonons by means of deformation potential. The Bose-Einstein distribution is taken into account by n, which is in this case much more temperature sensitive as the acoustical phonon energy is typically in the range up to a few meV. While acoustical phonon scattering, with confinement in one direction, lies in the range of a few hundred picoseconds at liquid helium, it strongly increases towards room temperature to lifetimes in the sub picoseconds range for small energy transitions. Looking at the electron-phonon coupling strength, the factor $\alpha(q)$ can be calculated as

$$\alpha(q) = \frac{D^2}{2\rho c_s \Omega}\,\hbar q \tag{2.1.11b}$$

using D the deformation potential (7.2 eV in the case of $In_{0.53}Ga_{0.47}As$), ρ the density of the material (5500 kg/m^3), c_s the velocity of sound (3400 m/s) and Ω the volume of the device. As acoustical phonons play no role at low temperatures, they were neglected for the optimization of the devices and

the more relevant interface defect scattering was used. At higher temperatures the acoustical phonon scattering replaces the interface defect scattering as dominant injection mechanism, both most efficient for low energy separations as found between the upper laser state and the lowest injection state.

2.1.5 Scattering by interface defects

At low temperatures, a major scattering effect is attributed to the interface defect scattering mechanism [Fer89], which is caused by coulomb impurities sitting at the mth-interface. For calculating the scattering rate at the mth-plane with the local coordinate x_m the following formula can be used:

$$\frac{1}{\tau_{if,ID}} = \frac{2\pi^2}{\hbar}\left(\frac{e^2}{4\pi\varepsilon}\right)^2 N_{imp} \sum_f \frac{1}{(E_i - E_f)} \left| \left\langle \varphi_f(x) \right| \exp\left(-|x - x_m| \sqrt{\frac{2m_{eff}}{\hbar^2}(E_i - E_f)}\right) \left| \varphi_i(x) \right\rangle \right|^2 \tag{2.1.12}$$

with N_{imp} being the area density of defects at an interface ($1.2 \cdot 10^{14}$ m^{-2} was assumed). The overall scattering rate can be taken from the sum over all interfaces, yielding the overall lifetime. For taking the temperature behavior into account, the Conwell-Weisskopf approximation is used, which adds the term for multiplying the overall scattering rate [Sch07].

$$\tau_i(T) = \tau_i(0) \cdot \frac{\sqrt{T^3}}{\ln(1+T^2)} \tag{2.1.12b}$$

It has to be admitted, that none the less, the interface scattering is only a rough estimation. It suits the optimization of the devices, but clear insights are still missing. While other groups have proposed that interface roughness scattering could be more dominant, this work was based on the theoretical models of R. Ferreira and G. Bastard [Fer89], which yields higher scattering rates for interface defects than roughness, assuming equal defect densities.

2.1.6 Summary of scattering mechanisms

There are more than just the three mentioned scattering mechanisms. Besides the interface defect scattering, also impurity scattering and interface roughness scattering can be investigated. As the describing is quite vague and leaves space for assumptions (i.e. impurity densities in a real device), it was considered less help full for an optimization algorithm. Theoretical scattering rates are a little bit larger than the interface defect ones. On the other side, electron-electron scattering was neglected following the argumentation of B. Williams [Wil03, pp. 74-79]. Also the detailed investigations for mid infrared devices by Iotti and Rossi [Iot01] showed that electron-electron scattering consideration would only modify the results by a few percent. It can be summarized, that optical phonons play the dominant part in the quantum cascade laser, used for effective depletion of the lower laser state and limiting the upper laser state lifetime. Only at small energy scales, as used in the injection into the upper laser state or in the injector miniband other scattering processes have to be taken into account. Besides scattering processes which are incoherent, resonant tunneling as coherent process, was considered as possible transport mechanism. It was at first ruled out for mid infrared [Iot01], but with deeper understanding

found to be sometimes important for the terahertz range [Kub09] and the mid infrared range [Khu09]. The important factor for the injection time is the dephasing, caused by in-plane scattering. Due to this scattering, carriers lose their phase, increasing resonant tunneling times. Although the fast scattering between two energetically close states in separated wells should lead to very short injection times, latest research indicates that the dephasing significantly increases the transit time [Liu09] and therefore the maximum current density [Fai07]. Therefore the separation of the injection states has to be well considered, balancing between fast scattering and fast tunneling. As this problem requires a complex 3-dimensional approach, like the non-equilibrium's green function method, it is unsuitable for design optimization and only allows a post-measurement analyze of the device in depth.

2.1.7 Electrical losses

This subchapter is similar to the subchapter within the optical properties section, focusing on losses inside the device. At this point only the electrical losses will be highlighted, but also impacts on the optical behavior are mentioned.

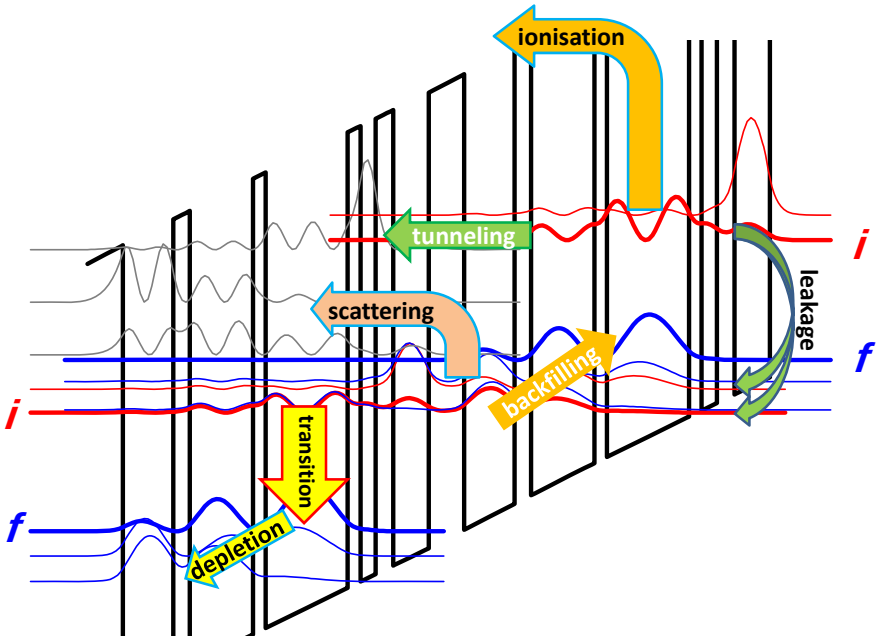

Fig 2-1-4: schematics of electrical losses inside the active region. The yellow filled arrows indicate the transition (red border) and the required losses by depletion (blue border). The unnecessary losses are shown in the second period. They are all design dependent, but also influenced by lattice temperature, material and applied electric field to some degree.

There are different loss mechanisms, which can be in general divided into required losses and unnecessary ones. The unnecessary losses in the active region, can be found in leakage paths, like thermal ionization of carriers. But also direct scattering from the ground state to the lower laser level or the depletion states of the following stage causes electric losses. As last point, thermal backfilling has to

be mentioned, a process in which carriers get re-exited into the lower laser level, reducing the effective population inversion. All these paths and mechanisms are shown in figure 2-1-4.

Another source of unnecessary losses comes from the contact resistances on one side, but also from low doped waveguides which induce ohmic losses. Those losses have to be minimized, especially for continuous wave operation, as they only generate heat. Unfortunately increasing the doping levels for reduced contact resistances and low ohmic serial resistances will also increase the waveguide losses by plasma absorption. Therefore a suitable compromise has to be chosen.

The required losses, in contrast to the unnecessary ones, are found in the depletion concept of the lower laser state, which normally uses one or two optical phonons. For every transition, the required energy is the sum of the emission energy and the energy required for depletion and injection. The second part is also called the voltage defect, which is tried to keep as low as possible, with suitable depletion and injection performance (see subchapter 4.4 about voltage defect and injection behavior).

2.2 Materials for the electrical design

All previous calculations are based on theoretical models, in which the materials are neglected. In reality however, different materials offer different effective masses and conduction band energies. When looking at the III-V map of semiconductors (see figure 2-1-5) the three possible groups of material systems come into view:

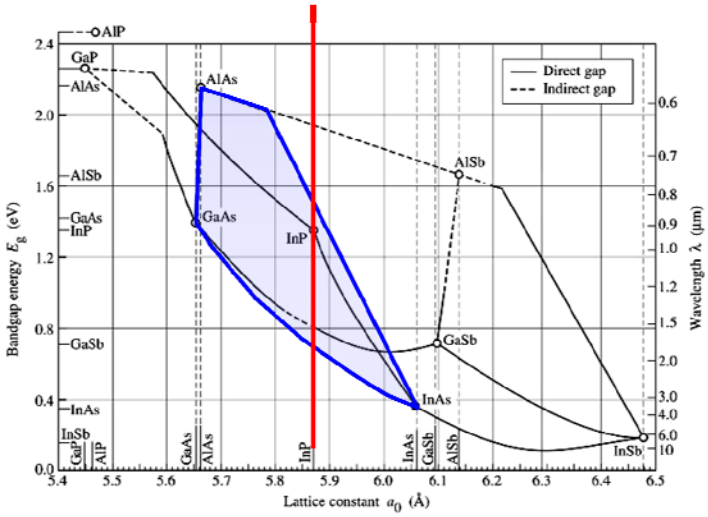

Fig 2-1-5: III-V semiconductors, the red line indicates the InP lattice, the blue area the AlGaInAs system

- $Al_xGa_{1-x}As$ on GaAs
- $Al_xGa_yIn_{1-x-y}As$ on InP
- AlGaInAsSb on GaSb

With decreasing effective mass, materials yield increasing peak gain. While the effective mass contributes to the peak gain by

$$g_p \propto \frac{1}{(m_{eff})^{3/2}} \qquad (2.1.13),$$

it also reciprocal increases the waveguide losses. From this point of view the GaSb based materials would be the best, but unfortunately they require the use of two different group five elements (InAs,GaSb or AlSb), making the growth even more complicated. For designing far infrared devices another point must be considered: a lower bandgap comes along with lower optical phonon energy, yielding a lower maximum population inversion. And important for both wavelength ranges are the conduction band offsets: limiting the maximum transition energies and increasing the losses into the continuum for mid infrared devices if too low, disabling good control of injection and tunneling rates for far infrared devices if too high. In the mid infrared, the material system using tensile strained AlInAs as barrier and compressive strained GaInAs as well, has shown so far the best performance. Additionally the previous work was done using this material system and MBE was well calibrated. Therefore the mid infrared multialloy structures are based on AlGaInAs. But for completeness and comparison the GaSb material system shall also be described (preliminary experiments are shown in appendix F).

2.2.1 Conduction band, effective mass and band gap

The material dependent effective mass, conduction band offset and band gap were calculated using nextnano, which included strain and temperature dependences. For the antimonid based systems the side valleys and the valence band levels were also taken into consideration. Figure 2-1-6 shows the band profile of various compounds based on the AlGaInAs system (left) and some compositions suitable for the growth on GaSb (right).

In general, the material parameters can be found in the summarizing work of I. Vurgaftman and J. Meyer [Vur01]. Nextnano uses these material parameters and applies the deformation potential theory by van de Walle [vdW89]. Additional details about thermal behavior can be found in the work of Sharma et al. [Sha83] and Varshni [Var69].

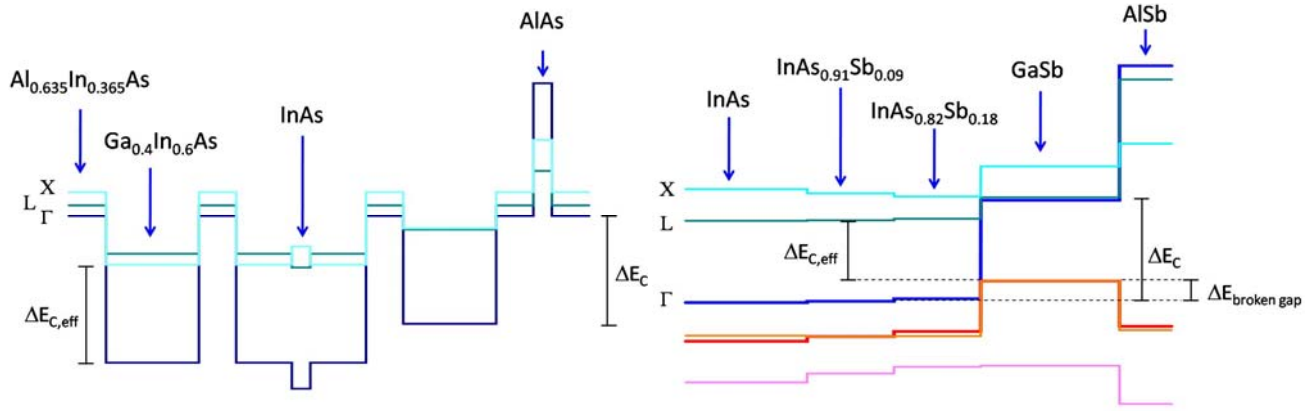

Fig 2-1-6: the AlGaInAs system (left), with a conduction band offset ΔE_c of 760 meV between the AlInAs barrier and the GaInAs well. In device design, the effective band offset also has to consider the ***L*** and ***X*** valley for scattering losses at higher fields and shorter emission wavelengths, leaving 520 meV for design ($\Delta E_{c,eff}$). The AlGaInAsSb system (right) offers a higher conduction band offset ΔE_c of 910 meV, which is reduced not only by side-valley scattering but also by a broken gap alignment (~ 180 meV). This leaves for the lattice matched case of InAsSb vs. GaSb about 540 meV for design. In both material systems, the binary Al-compound can be used for injection control and reduced thermal emission losses.

The material system using AlInAs and GaInAs on InP is most flexible, as the sidebands (***L*** & ***X***) are high enough, relative to the ***Γ***-band and no broken gap alignment occurs. In terms of growth, the single group-V element As provides better interface control, without the risk of segregation. This simplicity in regard to GaSb matched systems, is the reason why mid infrared devices are more successful on InP up to date.

Composition	Lattice	Bandgap	Conduction Band Offset	Effective Mass $m_{eff,\perp}$ ($m_{eff,\parallel}$)
	in Å	in eV	in eV	in $1/m_0$
InAs	6.0583	0.3978	0.0 (by definition)	- (0.0315)
$Ga_{0.4}In_{0.6}As$	5.9084	0.6483	0.1262	0.0407 (-)
$Ga_{0.47}In_{0.53}As$	5.8680	0.7317	0.1672	0.0410 (-)
$Al_{0.16}Ga_{0.31}In_{0.53}As$	5.8690	0.9230	0.3237	0.0480 (-)
$Al_{0.48}In_{0.52}As$	5.8680	1.2020	0.6315	0.0710 (-)
$Al_{0.635}In_{0.365}As$	5.8062	1.5930	0.8881	0.0790 (-)
AlAs	5.6613	1.9070	1.1092	0.1730 (-)

Tab 2.1.1: Table of material parameters for 300 K grown on InP

The most common used material compositions and its material parameters are shown in table 2.1.1, with the band offset and the band gap determined by the lowest energy band.

GaSb based materials (see figure 2-1-6) offer on one side a much higher peak material gain, more than a factor of 2 higher just by their lower effective mass. On the other side they accumulate a lot of growth related problems, like requiring at least two different group-V elements, since InAs is the only well material with a suitable energy difference between the ***Γ***-band and the next side valley. Finally many compositions result in broken gap alignment and only InAs against AlSb-containing layers avoids this. Unfortunately AlSb has a very large effective mass, conflictive to the higher peak material gain. Table 2.1.2 shows some material parameters, used in simulations, for GaSb-based compositions.

Composition	Lattice	Bandgap	Conduction Band Offset	Effective Mass m_{eff}
	in Å	in eV	in eV	in $1/m_0$
InAs	6.0583	0.417	0.0	0.022
$InAs_{0.91}Sb_{0.09}$	6.0959	0.316	0.012	0.019
GaSb	6.0959	0.726	0.921	0.041
AlSb	6.1355	1.642	1.429	0.115
InSb	6.4794	0.268	0.683	0.046 ($m_{eff,\perp}$)

Tab 2.1.2: Table of material parameters for 300 K grown on GaSb

2.2.2 Lattice matched and strain balanced

The first quantum cascade lasers were grown with lattice matched materials, to avoid strain accumulation and layer degradation. On the other side strained materials offered higher band offsets and lower effective masses. This is a result of higher In-content within the GaInAs layer and for compensation a higher Al-content in the barrier. Unfortunately, strain complicates the band profiles and effective masses, as latter split up into an in-plane and a perpendicular effective mass. The in-plane mass determines the lifetimes for electron-phonon scattering processes, while the perpendicular mass which equals the growth direction, defines the confined states. In figure 2-1-7 (left) the effective mass for

$Ga_xIn_{1-x}As$ is shown [Sha02], with the node indicating the InP lattice. The conduction band offset gets reduced under strain, defining a real limit for the maximum transition energy. The term strain, with its normal units being N per mm^2, is used in epitaxy as lattice mismatch in %, differentiating between pseudo-morphic and, by a factor of two smaller, relaxed lattice mismatch. When designing a structure three strain related rules have to be followed to avoid crosshatch or even complete degradation. First of all, the overall mismatch within one period has to be compensated, at best to 0, more practically below 0.1 % overall for thicknesses less than 2 µm and even lower for thicker stacks. As second rule, the lattice mismatch between two layers at their interface should not be larger than 2.0 % to avoid non

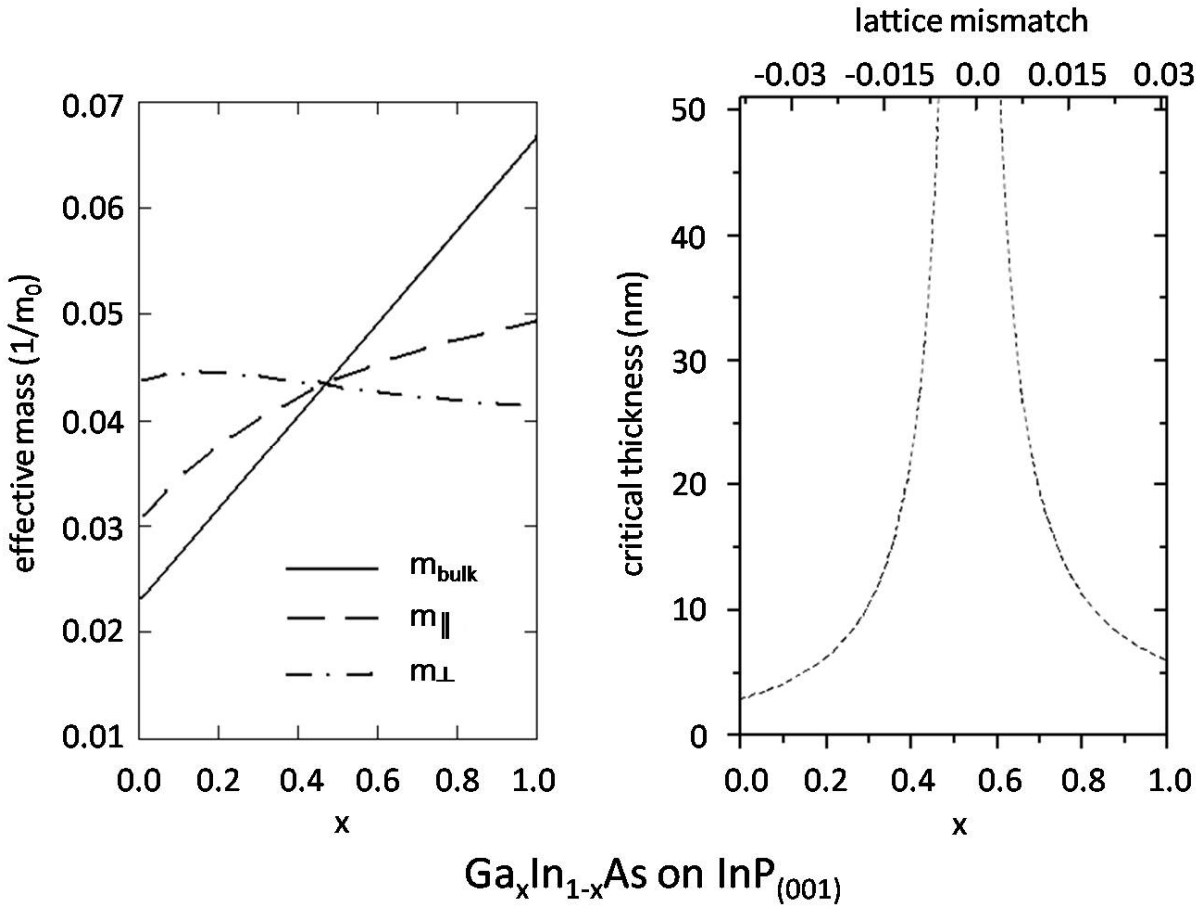

Fig 2-1-7: strain effects in GaInAs on InP, showing the effective mass [Sha02] for the unstrained (solid) case and the splitting into the in plane mass (dashed, y&z) and the perpendicular mass (dash-dotted, x) over the indium content (left). The critical thickness (right) is calculated by Matthews and Blakeslee over the indium content and the corresponding lattice mismatch

saturated bonds and higher defect densities. The third rule is governing the critical thickness within each layer of material and strongly thickness and lattice mismatch dependent, as shown by Matthews/Blakeslee [Mat74] and People/Bean [Peo85]. Figure 2-1-7 shows the critical thickness for $Ga_xIn_{1-x}As$ grown on InP [Koe09].

2.3 Design and optimization

When designing a new structure for a quantum cascade laser, many different approaches can be used. The wide range of decisions starts with vertical or diagonal transition, the first giving higher dipole matrix elements and the latter giving better lifetimes resulting in higher slope efficiencies. For a sufficient depletion of the lower laser state, the most common design is a double phonon resonance, while other approaches like a continuum of states are also possible. Following the two depletion states, most designs use an injector, a superlattice with a dense manifold of states. These injectors offer a series of key functions [Fra09] to the device and were used for the first successful designs [Fai94]:

- Efficient injection of electrons into the upper laser state
- Isolation of the upper laser state from the continuum
- Preventing electrons from tunneling into unwanted states
- Spatial and energetic separation of the lower laser state from the electron pool
- Providing space over which electrons can gain energy

Besides the conventional injector-based design, the injectorless design was first proposed by Wanke et al. in 2001. They used a continuum to continuum design, which resulted in very little thermal stability (T_0 ~ 48 K), low pulsed power ($P_{max,7K}$ ~ 300 mW) and limited operation temperature ($T_{max,pulsed}$ ~ 200 K). In general, the injector is an optical passive section and should be limited, while its key functions have to be maintained. This desire leads to the latest research in injectorless and short injector devices [Fra09] and a more advanced injectorless design principle proposed by G. Scarpa [Sca02], was used in combination with multiple materials in different material systems for mid infrared devices. For far infrared devices, the most common used design, proposed by Williams [Wil03b], using a single phonon for depletion and bringing upper and lower laser state into resonance with the states of adjacent quantum wells, achieved the highest operation temperatures for direct THz generation. In the following subchapters, the details of the injectorless mid-infrared design is explained.

2.3.1 Design optimization by evolution algorithm

When a new design has to be created, many degrees of freedom are found. Each individual barrier and well has a thickness and a material composition, making the problem multidimensional and discontinuous. An experienced designer can find a new solution within a few days of adjusting barriers and wells, finally achieving a good but unlikely the best solution. All approaches in solving the problem analytically by predefining wave functions and calculating the required structure also fail due to the complexity of the design. Let alone that the perfect wave functions are even unknown for each design. Therefore at the beginning of this work, the 1-band Schrödinger solver was extended to also calculate the injection efficiency by low energy scattering mechanisms and an evolution algorithm was implemented. This algorithm is best explained by figure 2-1-8.

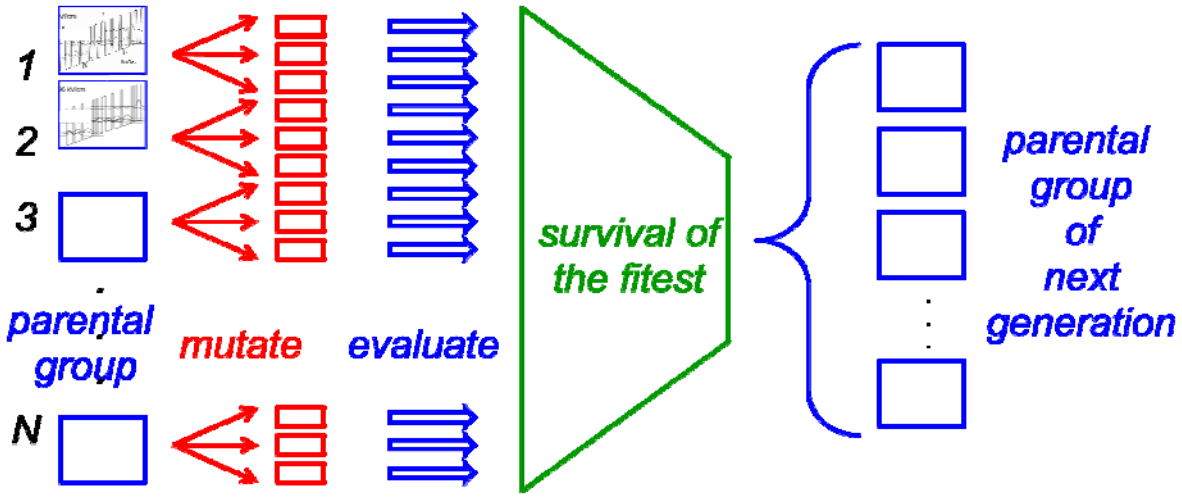

Fig 2-1-8: Principle of evolution algorithm showing the development through one generation

The range of possible evolution algorithms is large and it would fill a book of its own, to describe possible solutions to quantum cascade laser designs. Therefore only the used approach shall be described and some remarks on convergence and stability are made. In this work, a so called (μ+λ) evolution strategy was chosen, with μ being the number of parents per generation and λ the number of mutants per generation. The plus indicates that for the survival of the fittest all parents and mutants are evaluated and directly compared. In this case parents and mutants are defined by a different but complete set of thickness and material composition parameters for a single stage. At generation one, the starting parent generation, μ-parents are randomly chosen. This means for each parameter, thickness and composition, a random value within the boundaries is taken. Then a mutation step is done λ times for creating λ mutants. At each step one of the μ parents is randomly chosen and each of its parameter is randomly changed, following a gauss distribution and using the current standard deviation σ_n for mutation, with n being the step number. At this moment, the generation exists of λ+μ parameter sets, which all get evaluated. At first, the evaluation checks if all states are confined, then if any adjacent states are within the energy specifications for a transition. Afterwards the strain, if a parameter set is strain balanced or not, is considered.

If all of the three above mentioned criteria fit, the dipole matrix elements are calculated and checked if sufficient for the transition. If true, the *LO*-phonon scattering times are calculated and validated for the upper state to be larger and for the lower states to be smaller than a predefined value. At this point the stage is in principle working and a quality factor (see equation 2.1.14 below) can be determined. As last criteria the charge injection is checked, which is determined by the interface defect scattering time.

After all parameter sets have been evaluated, they get sorted by their general performance and their quality. The best μ parameter sets get defined as the next generation's parental group. As one can see, there is a so called selection pressure, defined by $(\lambda+\mu)/\mu$. As suggested by I. Rechenberg [Rec73], the standard deviation is not fixed but follows the one-fifth rule: If the number of successful mutations in comparison to overall mutations is larger than 20 %, the parameters seem to be further away from the optimum and the standard deviation for the next step gets increased by a factor of 1.22. If less than 20 % of all mutations are successful, the solutions already chosen seem to be close to an optimum and the standard deviation gets reduced by a factor of 0.82.

To summarize the effect of the evolution algorithm, it has to be stated that finding the correct evolution window in number of parents, mutants and standard deviation is the key for a successful optimization. And also the boundaries of the parameter set should be predefined, as in barrier and wells alternating with reasonable thickness ranges for each. Most successful simulations used the following ranges of numbers:

μ	~	20000 – 40000	
λ	~	3 to 4 · μ	
σ_0	~	0.1 – 0.2	(in nm, or alloy composition)
generations	~	6 – 10	

Nearly all of the standard mid infrared structures have been optimized by using this evolution algorithm, especially the first successful design (figure 2-1-9 right) was taken exactly from the device optimization, showing its great potential. For reducing the computational effort, all parameter sets failing to achieve a key requirement, i.e. strain balanced, got rated down and the next parameter set was taken into inspection without doing the following calculations, i.e. dipole matrix elements. This allowed calculation times for a single structure to be below 0.6 s on a 1.8 GHz Dual Core machine (using only one core at 100 %), achieving a run through 1'000'000 structures within one week. Till the end of this thesis more than 40'000'000 structures have been evaluated.

2.3.2 Designs for mid infrared devices based on InP

This chapter just presents the reference two-alloy design, which was developed by the previous PhD student A. Friedrich and the first by evolution approach optimized four alloy designs. All following designs are described in the *"Results and Discussion"* section to emphasis the direct link to the corresponding results.

The first device [Kat08], which uses four material alloys and was optimized by the evolution algorithm, was designed with similar field, period length and emission wavelength to the current best injectorless device [Fri06]. Figure 2-1-9 shows both designs, while the new approach (right) uses highly strained InAs and AlAs for achieving better lifetimes and reduced carrier losses due to high fields and thermal ionisation.

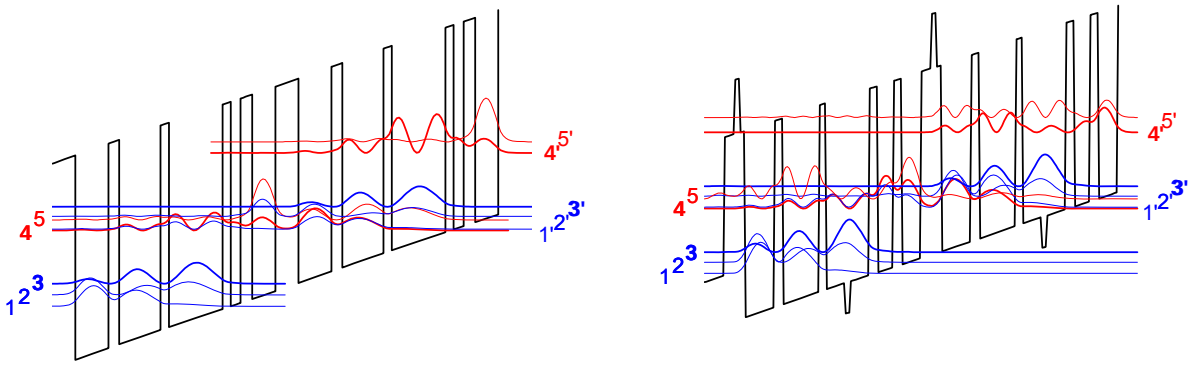

Fig 2-1-9: active region of regular injectorless device (left) and advanced design (right) using locally increased barriers (AlAs) and decreased effective mass (InAs). The layer sequences are **2.8**/4.0/**1.3**/5.0/**1.0**/6.5/**1.0**/1.2/**1.4**/2.8 for the left design and **1.45**/***0.5***/**0.56**/4.03/**1.1**/5.0/**0.9**/2.6/*0.51*/2.6/**1.0**/2.1/**1.0**/2.66 for the right design in nm, with the four material compositions: ***AlAs in bold and italic***, $\mathbf{Al_{0.635}In_{0.365}As}$ **in bold**, $Ga_{0.4}In_{0.6}As$ in regular and *InAs in italic style*. The silicon doped layers are indicated by an underline.

Both designs use five confined states, three lower ones (1-3) and two upper ones (4-5) separated by an optical phonon energy. Between state 3, the lower laser level (thick blue), and state 4, the upper laser level (thick red), the stimulated transition takes place. For comparing the performance of both designs formula 2.1.7 can be simplified to

$$g_c \propto \frac{\tau_i}{\lambda} \cdot \frac{{z_{if}}^2}{L_p} \tag{2.1.14}$$

offering a first impression of the design quality. The other parameters of the gain coefficient are expected to be nearly constant as long as a proper depletion is maintained. In the case of the shown designs the left one yielded a quality factor of 36 ($\tau_i \sim 1.4$ ps, $z_{if} \sim 2.2$ nm) and the right design a 28 % higher quality factor of 46 ($\tau_i \sim 4.2$ ps, $z_{if} \sim 1.4$ nm). Since the left design showed under a specific sheet doping density a threshold current density of 0.73 kA/cm^2, the new design, using the same waveguide

design, was expected to yield a 28 % lower current density of approximately 0.57 kA/cm^2. This was shown successfully [Kat08] and more details about the results can be found in the *"Discussion and Results"* section of this thesis. This direct comparability was only possible since all other design dimensions like field, period length, waveguide losses were kept the same. In other designs, some or all of these were changed, making a direct comparison more complex. In case of increasing fields, higher losses due to thermal emission into the continuum or side valleys are expected, which are not treated within our simulation. Changing wavelengths also changes confinement factors and waveguide losses. Different states can completely alter the intersubband absorption or other leakage paths and therefore all quality factors have to be seen as crude expectation to a new design but nothing more. More designs and the results are introduced in the already mentioned *"Results and Discussion"* section.

2.4 Optical Model and Theory

In the previous chapter the electrical properties have been described in detail, leading to the material gain and the gain coefficient. Besides the discussed gain, the optical properties play an important role in every laser design. The chosen materials and resonator design determines which modes exist and the mirror and waveguide losses for these modes. Overall the optical design greatly influences the threshold current densities, the output efficiency and the overall power. Therefore this chapter covers more than the optical properties of modal gain and confinement factor. It will also describe the pulsed characteristics in combination with the electrical properties from the previous chapter. At the end some waveguide designs for mid and far infrared devices are presented in combination with material parameters and calculated examples.

2.4.1 Optical Resonator

Without feedback from an optical resonator, the emission of light would remain spontaneous, incoherent and very inefficient, due to the short upper state lifetimes. It would remain an intersubband light emitting diode instead of a laser. The most simple model of this optical resonator, a gain medium between two plane mirrors, also called Fabry-Pérot resonator (see figure 2-2-1), is suitable for describing the general principles.

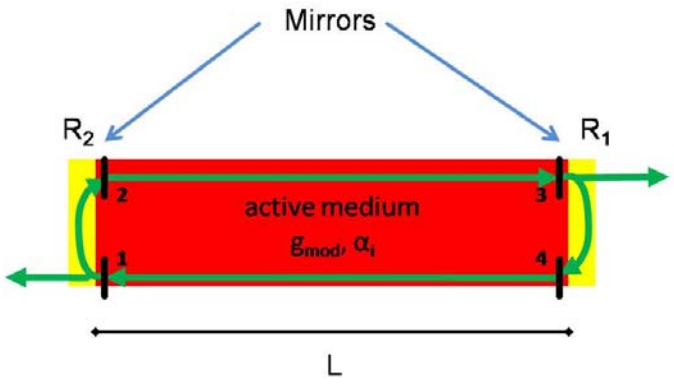

Fig 2-2-1: Fabry-Pérot resonator

A medium with the modal gain g_{mod} and the internal loss α_i is clamped between two plane mirrors with the power reflectivity's R_1 and R_2. The overall length of the resonator L shall be completely filled by the active medium. When observing one round trip of an electro-magnetic wave, its amplitude F' can be written as [CasH78]:

$$F'_{(1)} = F_{(1)} \cdot \sqrt{R_2} \cdot \sqrt{e^{(g_{mod}-\alpha_i)L}} \cdot \sqrt{R_1} \cdot \sqrt{e^{(g_{mod}-\alpha_i)L}} \qquad (2.2.1a)$$

with $F_{(1)}$ being the initial amplitude and ignoring the phase condition for now. For a stable operation, the amplitude has to reproduce itself exactly after one round trip, yielding the threshold condition

$$g_{mod} = \alpha_i + \frac{1}{L} \cdot ln\left(\frac{1}{\sqrt{R_1 R_2}}\right) = \alpha_i + \alpha_m \qquad (2.2.1b).$$

The modal gain g_{mod}, the internal losses α_i and the mirror losses α_m will be explained in detail below in subchapter 2.4.4 and 2.4.5, respectively. When taking the phase into account, it becomes clear

that after each round trip, the amplitude can interfere constructively or destructively, depending on the phase. Therefore the phase condition, written as

$$\lambda_i = \frac{2n'_{eff}L}{i} \tag{2.2.1c}$$

with n'_{eff} being the real part of the effective index and i the index of the i^{th}-mode, has to be matched additionally. For long resonators, like edge emitters, the index i becomes large and the phase condition is easily fulfilled multiple times within the gain spectra. Only for measuring the gain directly, these conditions are used again, as explained in subchapter 4.1.3.

Besides the already mentioned internal and mirror losses, optical resonators also exhibit diffraction losses. If the stability condition is fulfilled these diffraction losses play a minor role. For any resonator this stability condition can be written as [Eic91]

$$0 < \left(1 - \frac{L}{radius\ of\ mirror\ 1}\right)\left(1 - \frac{L}{radius\ of\ mirror\ 2}\right) < 1 \tag{2.2.1d}$$

yielding a value of 1 for a Fabry-Pérot resonator, because of its plane mirrors with infinite radius. In the case of semiconductor lasers, the plane mirrors are normally created by cleaved facets and show better quality than any dry etched round facet. Therefore the diffraction problem is overcome by waveguiding within the active medium between the two mirrors. The principle of waveguiding will be explained in the next subchapters, while the details of modal gain and optical losses follow afterwards.

2.4.2 TM-Wave propagation in a slab waveguide

For TE and TM modes, the wave propagation within a dielectric slab waveguide can be written as three independent scalar wave equations [CasH78], given as

$$\Delta E_x = \mu_0 \varepsilon \frac{\partial^2 E_x}{\partial t^2} \tag{2.2.2a}$$

$$\Delta E_y = \mu_0 \varepsilon \frac{\partial^2 E_y}{\partial t^2} \tag{2.2.2b}$$

$$\Delta E_z = \mu_0 \varepsilon \frac{\partial^2 E_z}{\partial t^2} \tag{2.2.2c}$$

for the electric field, and

$$\Delta H_x = \mu_0 \varepsilon \frac{\partial^2 H_x}{\partial t^2} \tag{2.2.2d}$$

$$\Delta H_y = \mu_0 \varepsilon \frac{\partial^2 H_y}{\partial t^2} \tag{2.2.2e}$$

$$\Delta H_z = \mu_0 \varepsilon \frac{\partial^2 H_z}{\partial t^2} \tag{2.2.2f}$$

for the magnetic field, with x being the growth direction, z the direction of propagation and y the in-plane direction. Due to the quantum mechanical selection rules, well described in the work of G. Scarpa [Sca02], the polarization of the transition is within the growth direction x. Therefore the quantum cascade laser requires a waveguide suitable for TM polarized electromagnetic waves. The TM mode, with $H_z = 0$ by definition, and no variation over the y direction ($\partial/\partial y = 0$), results in $E_y = H_x = 0$. Therefore the TM mode can be written as

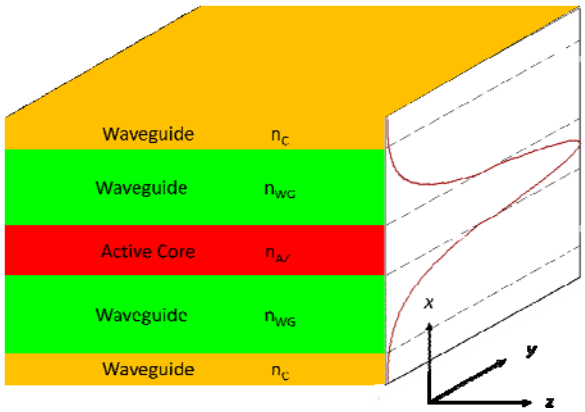

Fig 2-2-2: dielectric slab waveguide for a mid infrared wave. The TM_0 Mode is displayed with its H_y component, propagating into the z direction.

$$\frac{\partial^2 H_y}{\partial x^2} + (n^2 k_0^2 - \beta^2) H_y = 0 \tag{2.2.3}$$

with n being the refractive index, k_0 the free space propagation constant and β the phase constant. Figure 2-2-2 shows a dielectric slab waveguide schematic, fulfilling the condition

$$n_{AZ} > n_{WG} > n_C \tag{2.2.3b}$$

for guided modes within the active core. The solution of equation 2.2.3 gives an in x-direction varying H_y component, with sinusoidal behavior inside the core layer and exponential decay in the wave guiding layers, propagating in the z-direction. With d_{AZ} being the thickness of the active core, H_y can be written as [CasH78]:

$$H_y = H_0 \cdot cos(\kappa x) e^{j(\omega t - \beta z)} \tag{2.2.4a}$$

using $\kappa = n_{AZ}^2 k_0^2 - \beta^2$, for x between $\pm d_{AZ}/2$. Outside the active core,

$$H_y = H_0 \cdot cos\left(\kappa \frac{d_{AZ}}{2}\right) \cdot e^{-\gamma(|x| - d_{AZ}/2)} \cdot e^{j(\omega t - \beta z)} \tag{2.2.4b}$$

represents the magnetic field component, with γ^2 being defined as $\beta^2 - n_{WG}^2 k_0^2$. The electric field components can be derived from the Maxwell equations, giving components in the z and x direction.

2.4.3 Plasmon waveguides for TM polarized waves

TM polarized waves, in contrast to TE polarized ones, offer the possibility of plasmon waveguiding. This is always required for far infrared devices, as the long wavelengths prevent the growth of dielectric slab waveguides. For mid infrared devices it is a possible option [Bou09][Xu09], but only recommended for surface emitting devices. Plasmon waveguide in general enabled, when the plasma resonance of the material is larger than the wavelength and, as already mentioned, a TM

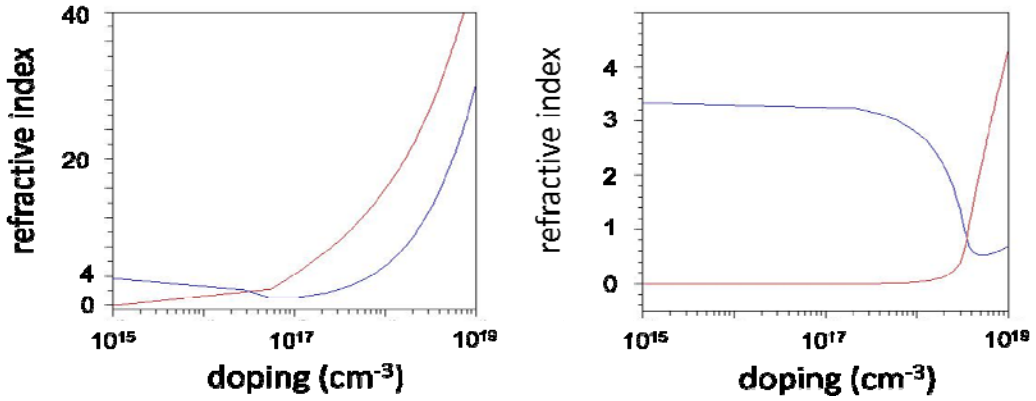

Fig 2-2-3: doping dependent real (blue) and imaginary (red) part of the refractive index at 75 µm (left) and a 7 µm (right) for lattice matched GaInAs. Calculated by equation 2.2.15 and experimental data parameters.

polarized wave is present. For a general treatment of plasmon waveguides, the same Maxwell equations can be used as introduced before, but the complex part of the permittivity plays the major role. In conductors, fulfilling the condition of $\sigma \gg \omega\varepsilon_r\varepsilon_0$, the complex permittivity can be written as [Det05].

$$\varepsilon_r = -j\frac{\sigma}{\omega\varepsilon_0} \qquad (2.2.5a) \qquad \text{yielding} \qquad n' = n'' = \sqrt{\frac{\sigma}{2\omega\varepsilon_0}} \qquad (2.2.5b)$$

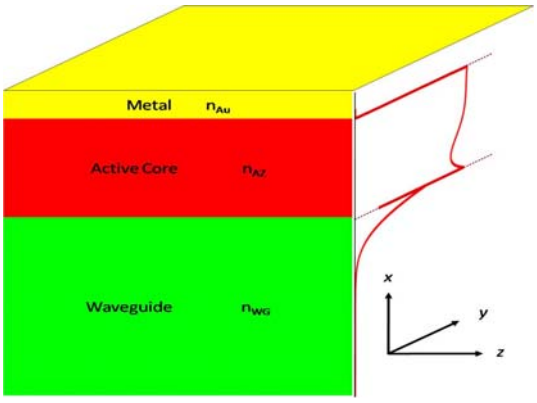

Fig 2-2-4: plasmonic waveguide for a far infrared (THz) wave. The TM_0 Mode is displayed with its H_y component, propagating into the z direction. Between the waveguide and the active core, a highly doped, thin, GaInAs layer is implemented

with the penetration depth of the field being given by the skin effect [Det05]

$$\delta = \sqrt{\frac{2}{\omega\sigma\mu_0}} \qquad (2.2.6).$$

It can be seen that highly doped layers (see figure 2-2-3) offer a suitable guidance by strong attenuation and low doped areas are required into which the wave can be confined. Figure 2-2-4 shows a simple plasmon waveguide, displaying the x-dependent H_y component, quenched between a metal layer and a highly doped GaInAs layer beneath the active core.

2.4.4 Confinement factor and modal gain

In chapter 2.1.2, using formula 2.1.6, we calculated the peak material gain, which we can now transfer into the more important modal gain, which is used in equation 2.2.1b. Following the work of T. Visser et al. [Vis96], the modal gain of a TM polarized wave is calculated by

$$g_{mod} \approx \Gamma_{AZ}^{TM} \cdot g_p - \frac{Im\left\{\tilde{H}_y{}^2 \cdot \frac{j\Delta Im\{n_{AZ}\}\overline{\partial H_y}}{Re\{n_{AZ}\} \quad \partial x}\right\}}{k_0^3 \cdot \int_{-\infty}^{\infty} \left|\tilde{H}_y(x)\right|^2 dx} \tag{2.2.7}$$

using the confinement factor

$$\Gamma_i^{TM} = \frac{\int_i \left|\tilde{H}_y(x)\right|^2 dx}{\int_{-\infty}^{\infty} \left|\tilde{H}_y(x)\right|^2 dx} \tag{2.2.8}$$

This shows that the modal gain for a TM mode is normally smaller compared to an equal TE mode, since polarization effects take place.

For real devices, the modal gain is estimated using the product of the threshold current density j_{th}, the confinement factor Γ and the gain coefficient g_c, which equals the total losses α_{tot} at threshold. This threshold current density formula can be written as [Fai94]

$$g_{mod} = g_c \cdot \Gamma \cdot j_{th} = \alpha_i + \frac{1}{L} \ln\left(\frac{1}{R}\right) = \alpha_{tot} \tag{2.2.9}$$

The right term of equation 2.2.9 contains the losses, which can be separated into the mirror losses and the internal losses α_i. The next subchapter will explain the loss mechanisms in detail.

2.4.5 Optical losses

Similar to electrical losses, there are optical losses, which influence the behavior of the laser device. In general, they are much more important than the electrical losses, as they not only prevent the laser from reaching threshold but are also more challenging to controll.

The right part of the loss term in equation 2.2.9 is the contribution of the mirror losses. A normal wave under 90° incident is reflected at a given refractive index change to some part. Most often the semiconductor – air interfaces at the cleaved facets are used, with

$$R \approx \left(\frac{n_{eff}-1}{n_{eff}+1}\right)^2 \tag{2.2.10}$$

being the power reflectivity R of a single interface. In the symmetric case, the mirror losses α_m can be normalized over the length, yielding (similar to equation 2.2.1b)

$$\alpha_m = \frac{1}{L} \ln\left(\frac{1}{R}\right) \tag{2.2.11}.$$

In case of high reflectivity coatings, the different reflection coefficients have to be taken into account. For metal coatings the imaginary part n'' dominates the reflection R (2.2.12a) while in case of distributed Bragg reflectors [Yeh88][Wan74] the increased reflectivity can be calculated by 2.2.12b

$$R_{metal} \approx \frac{(n'-1)^2+(n'')^2}{(n'+1)^2+(n'')^2} \qquad (2.2.12a) \qquad R_{DBR} \approx \left(\frac{1-\frac{n_A}{n_E}\left(\frac{n_1}{n_2}\right)^{2M}}{1+\frac{n_A}{n_E}\left(\frac{n_1}{n_2}\right)^{2M}}\right)^2 \qquad (2.2.12b)$$

The change in reflectivity, changes the mirror losses according to

$$\alpha_m = \frac{1}{2L}\ln\left(\frac{1}{R_1 R_2}\right) \qquad (2.2.13)$$

with $R_{1(2)}$ being the reflectivity of the interface *1(2)*. This change in reflectivity also alters the laser performance in general. A perfect reflection would prevent any light from being emitted, therefore high reflectivity coatings are only used on the back facet.

Besides the mirror losses, the internal losses α_i determine the laser behavior. They consist of free carrier absorption predominantly but also intersubband absorption can play a role. In case of far infrared devices, the absorption on optical phonons also contributes to the losses, especially closer to the absorption peaks in the 30 to 50 µm range. In general the internal losses, can be calculated by the imaginary part of the refractive index by

$$\alpha_i = 2\frac{2\pi}{\lambda}\cdot n'' \qquad (2.2.14).$$

All absorption mechanisms change the real and the imaginary part of the refractive index, therefore we use a combination of the classical Drude model [Sca02] and the absorption by optical phonons [Abs79] as suggested by Palik [Pal85]. This can be done as follows

$$(n' - jn'')^2 = \varepsilon = \varepsilon_\infty \cdot \left[\frac{\omega_{LO}^2-\omega^2}{\omega_{TO}^2-\omega^2} - \frac{\tilde{\omega}_p^2}{\omega^2\eta} - j\frac{\tilde{\omega}_p^2}{\omega^2\eta}\cdot\frac{1}{\omega\tau}\right] \qquad (2.2.15)$$

with

$$\eta = 1 + \frac{1}{(\omega\tau)^2} \qquad (2.2.15b) \qquad \text{and the scattering time } \tau = \frac{\mu_e m_{eff}}{e} \qquad (2.2.15c)$$

using the modified plasma frequency

$$\tilde{\omega}_p^2 = \frac{1}{\sqrt{\varepsilon_\infty}}\cdot\frac{n_e e^2}{\varepsilon_0 m_{eff}} \qquad (2.2.15d).$$

with n_e being the concentration of free carriers. From this complex permittivity the real and imaginary part can be extracted as follows:

$$n' = \sqrt{\frac{\sqrt{\varepsilon'^2+\varepsilon''^2}+\varepsilon'}{2}} \qquad (2.2.16a) \qquad n'' = \sqrt{\frac{\sqrt{\varepsilon'^2+\varepsilon''^2}-\varepsilon'}{2}} \qquad (2.2.16b)$$

A more complex model of the absorption, taking the linewidths of the optical phonon branches into account is shown in Appendix E. With normal emission energies being far away from the phonon energies of the used semiconductors, they can be neglected. Dielectrics in contradiction have strong absorption peaks in the mid infrared, which has to be considered for narrow ridge waveguides, like used in continuous wave processes.

The last absorption mechanism which has to be mentioned is the intersubband absorption between different confined states. It is exactly the opposite of the stimulated emission, depending on the carrier concentration, the energy separation and the dipole matrix element. Since the intersubband absorption is strongly design dependent, we neglect it in the estimation of waveguide losses and assume a suitable design. As shown in subchapter 3.1, the inter-subband absorption is much lower in injectorless designs than in injectorbased ones as less confined states are existent.

2.5 Materials for the optical design

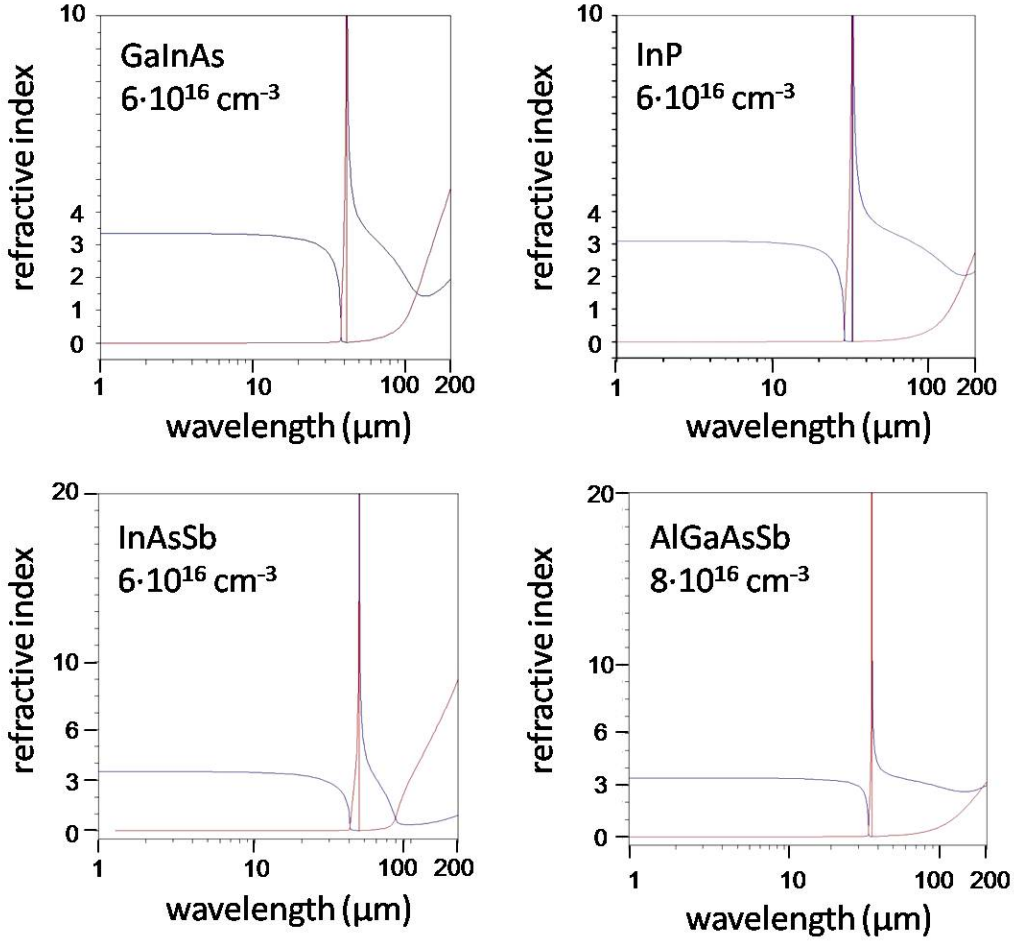

Fig 2-2-5: wavelength dependent refractive indexes (real part in blue, imaginary part in red) for different materials at low doping simulated using equatition 2.2.15

As mentioned in chapter 2.1 & 2.2, the design of the electrical active zone and the choice of materials, determines the complex refractive index of the waveguide core. Therefore suitable materials, with lower refractive index and low absorption losses are preferred for slab waveguides while plasmonic waveguides are realized at best with metal surrounding a low doped active region. Figure 2-2-5 shows some refractive indexes for different materials in wavelength dependence.

In the next subchapters, some exemplary waveguides are described, which were used for the specific material and wavelengths. The specific waveguide designs were varied multiple times during this work, using different materials, doping levels and thicknesses and therefore the most optimized design shall only be introduced here. The material data for the index calculation and the waveguide simulations was taken from various sources. Optical properties of metals can be found in the recapitulatory work of Ordal et al. [Ord82][Ord85], while most of the optical constants for

semiconductors were taken from the summarizing archive at the Ioeffe Institut [Iof], which only deviate a few percent from the evaluated values by C. Grasse [Gra10].

2.5.1 InP based waveguide materials for mid infrared devices

The advantage of InP based devices in the mid infrared can be found by simple use of the binary InP as waveguide. While the active region consists mostly of ternary AlInAs/GaInAs which yields a refractive index around 3.3 the InP substrate offers a natural waveguide ($n \approx 3.07$) with good heat conductivity and growth conditions. Figure 2-2-6 shows a mid infrared waveguide, with its parameters displayed in table 2.2.1.

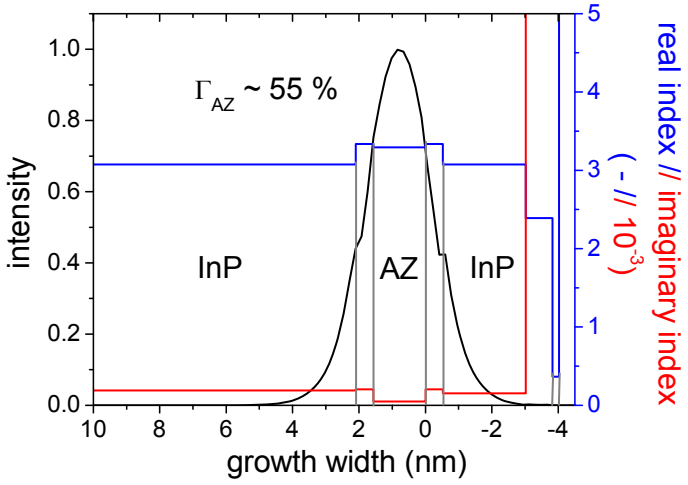

Fig 2-2-6: mid infrared waveguide showing the intensity of a 7.1 µm wave (black) and the corresponding refractive index with real part (blue) and imaginary part (red)

Material	d (µm)	n (cm^{-3})	n'	n''
InP	-	$6 \cdot 10^{16}$	3.07	$2 \cdot 10^{-4}$
GaInAs	0.53	$6 \cdot 10^{16}$	3.33	$2.1 \cdot 10^{-4}$
Active	1.57	var	3.30	$0.5 \cdot 10^{-4}$
GaInAs	0.53	$6 \cdot 10^{16}$	3.33	$2.1 \cdot 10^{-4}$
InP	2.5	$6 \cdot 10^{16}$	3.07	$1.5 \cdot 10^{-4}$
GaInAs	0.8	$5 \cdot 10^{18}$	2.388	0.0646
GaInAs	0.2	$2 \cdot 10^{19}$	0.366	3.098
Ti/Pt/Au	0.92	-	6.05	13+

Tab 2.2.1: Waveguide parameters for Fig 2-2-6

A confinement factor of 55 % can be calculated at an emission wavelength of 7.1 µm for this waveguide, while the confinement in the highly doped layers is below 0.08 %. The effective index gives 3.21 for *n'* and 0.00024 for *n''*, yielding waveguide losses α_i of 4.2 cm^{-1} theoretically. The estimated mirror losses α_m can be found around 3.2 cm^{-1} with the evaluated effective index for a 4 mm long sample. For electrical characterization and allowing the direct measurement of the applied field, a structure was grown, which consisted of a full waveguide without any active region. This structure was processed as regular metal cladded ridge waveguide for the determination of serial resistances.

2.5.2 GaSb based waveguide materials for the mid infrared devices

For covering the full theory of possible materials for mid infrared devices, also possible waveguides for GaSb based devices shall be described. In opposite to InP based devices, the GaSb based system is more complex in finding a proper waveguide. In the work of J. Devenson et al. [Dev07a&b] the active region consisted of an InAs/AlSb superlattice. The used material composition [Dev07b] yields a refractive index of 3.32 for the active zone. With GaSb and InAs having larger refractive indexes only AlSb can be used as waveguide, which unfortunately completely oxidizes if purely used. If used as

$Al_{0.8}Ga_{0.2}As_{0.078}Sb_{0.922}$ the refractive index difference equals 0.15, sufficient for waveguiding but problematic regarding thermal resistance [Bor02] and doping behavior [Die07]. Therefore they used highly doped InAsSb as plasmonic waveguide [Dev06], which results in higher waveguide losses (estimated to be around 7 cm^{-1}, even at these low wavelengths.

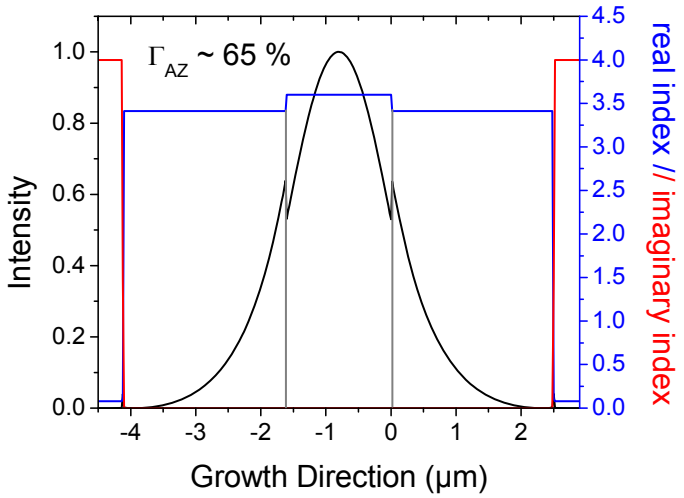

Fig 2-2-7: mid infrared waveguide showing the intensity of a 5.5 µm wave (black) and the corresponding refractive index with real part (blue) and imaginary part (red)

With the implementation of GaSb instead of AlSb within the active region, the refractive index of the active zone increases to 3.6. This makes it more suitable to regular waveguiding with $Al_{0.5}Ga_{0.5}As_{0.049}Sb_{0.951}$, yielding a refractive index difference of 0.2 and slightly decreased thermal resistance. And if using $Al_{0.8}Ga_{0.2}As_{0.078}Sb_{0.922}$ as waveguide material, the refractive index difference increases to 0.4 allowing thinner waveguide layers which also decrease the thermal resistance.

Figure 2-2-7 shows the waveguide for a 5.5 µm emission wavelength, with table 2.2.2 giving the waveguide details. The effective refractive index was simulated to be 3.485 + j $2 \cdot 10^{-4}$. The estimated waveguide losses α_i are 4.6 cm^{-1}, the confinement factor of the TM mode within the active zone yielded 65 % and the mirror losses for 4 mm long cavity are 2.95 cm^{-1}. In combination with the improved gain, the overall performance of the device should be theoretically better, than any given InP device. Unfortunately the material quality of GaSb growth is much more complex (see Apendix F).

Material	d (µm)	n (cm^{-3})	n'	n''
InAsSb	0.5	$2 \cdot 10^{19}$	0.08	4.00
AlGaAsSb	2.5	$8 \cdot 10^{16}$	3.41	$1.4 \cdot 10^{-4}$
Active	1.62	Var	3.61	$1.5 \cdot 10^{-4}$
AlGaAsSb	2.5	$8 \cdot 10^{16}$	3.41	$1.4 \cdot 10^{-4}$
InAsSb	0.5	$2 \cdot 10^{19}$	0.08	4.00

Tab 2.2.2: Waveguide parameters for Fig 2-2-7

2.6 Laser characteristics

So far the electrical and optical properties have been introduced, which allows to estimate laser characteristics as threshold current density, slope efficiency and output power in pulsed operation. In general, the macroscopic laser characteristics shall be linked to the previously mentioned properties.

Writing equation 2.2.9 differently, we obtain

$$j_{th} = \frac{\alpha_i + \frac{1}{L}\ln\left(\frac{1}{R}\right)}{g_c \cdot \Gamma} \tag{2.2.17}$$

a formula which directly tells us something about the relation between losses, modal gain and threshold. This formula can then be expanded to the temperature dependent factors

$$j_{th}(T) = \frac{\alpha_i(T) + \alpha_m}{g_c(T) \cdot \Gamma} \approx j_0 \cdot e^{\frac{T}{T_0}} \tag{2.2.18}$$

with the right side of the equation being used as a temperature fit. T_0, the characteristic temperature, includes all temperature dependent effects like mobility, transition linewidth and lifetimes, which normally decrease the performance over temperature. The characteristic temperature (T_0) determines the continuous wave operation, in combination with the heat resistance and the threshold power, but also influences pulsed operation performance.

When a device reaches threshold condition, other macroscopic descriptions come into consideration. The slope efficiency *dP/dI*, for example, includes the quantum efficiency of the active region, the number of cascaded periods and the loss management. It can be written as [Fai07][Sca02]

$$\frac{dP}{dI} = \frac{1}{2}\frac{hf}{e} \cdot \frac{\alpha_m}{\alpha_m + \alpha_i} \cdot N_p \cdot \left\{1 - \left[\frac{\tau_f}{\tau_i}\left(\frac{1}{\eta_{in}} - 1\right) + \frac{\tau_f}{\tau_{if}}\right]\right\} \tag{2.2.19}$$

with N_p being the number of stages, $\tau_{f,i,if}$ being used with the same denomination than in figure 2-1-2. The factor *0.5* is representing the single facet emission, while the injection efficiency η_{in} is given by the ratio of charges being injected into the upper laser level and over all injected charges into all possible levels. In good designs for mid infrared, the injection efficiency ranges around 70 % to 80 %, while the far infrared devices have smaller injection efficiencies, due to less energy separation between lower and upper laser state. Correlated to the slope efficiency, the overall efficiency, also called wall-plug efficiency (*WPE*) can be estimated by [Fai07]

$$WPE = \frac{(j_{max} - j_{th})}{j_{max}} \cdot \frac{dP/dI}{V} \tag{2.2.20}$$

with j_{max} being the maximum current density before the negative differential resistance (NDR) appears. The NDR is one major limitation under pulsed operation and is determined by the doping sheet density n_s and the overall transition time τ_{trans} with

$$j_{max} = \frac{e \cdot n_s}{\tau_{trans}} \qquad (2.2.20b).$$

The transit time, depending on the scattering rates within the device, is significantly smaller for injectorless devices than compared to injector based devices. This offers either higher maximum current densities at equal doping levels or in opposite, reduced doping levels under equal performance.

The maximum temperature T_{max} of operation can be estimated by the maximum current density, using equation 2.2.20b and the corresponding temperature dependent threshold current density from equation 2.2.18. In continuous wave operation, the maximum temperature of operation is limited by more factors, which will be explained in the next chapter.

2.7 Thermal Model and Theory

After having considered the pulsed characteristics, which can be derived from the electrical and optical properties of a device, the continuous wave behavior shall be discussed. In general, assuming perfect heat removal and no influence by the transient response, a device would behave similar in pulsed and continuous wave operation. The pulsed device is the best possible performance, regarding the characteristics like threshold current density and wall-plug efficiency, a real continuous wave operating device can achieve. On the other side, pulsed devices show in reality strong transient behavior because of heating up during the pulse, shifting in wavelength and power performance. In this chapter, the general theory of thermal conductance and the influence on heat on the device performance shall be described.

2.7.1 Thermal conductivity

A quantum cascade laser is dissipating power mostly into heat, except for the photons being coupled out. This heat will lead to an increase in temperature inside the device's active zone, while the heat sink should remain at a constant temperature. This gradient will cause a heat flux, which can be described by [Kit84]

$$j_{heat} = -\lambda \cdot \nabla T_{(\vec{x},t)} \tag{2.3.1}$$

assuming a homogeneous medium with heat conductance λ. Using the continuity equation of energy, one can obtain the heat conductance equation [Kit84]

$$\frac{dT_{(\vec{x},t)}}{dt} = -\frac{\lambda}{C} \cdot \Delta T_{(\vec{x},t)} \tag{2.3.2}$$

with C being the heat capacity per unit of volume. Under continuous wave operation, the device will heat up according to equation 2.3.2. In this case used materials and the geometry of the device play a significant role in achieving a good heat removal, which can be written as a location and temperature dependent heat conductance $\lambda_{(\vec{x},T)}$. With this general description, this complex problem can be solved by the finite element method quite well.

2.7.2 Heating effects on device performance

As already mentioned in chapter 2.6, equation 2.2.18 describes the temperature dependent threshold current density. In reality, a device being driven by any duty cycle (*dc*), being defined as the repetition frequency multiplied with the pulse length, will have a higher temperature than the heat sink is set to. With the electrical power being

$$P_{el} = A \cdot j \cdot V \cdot dc \tag{2.3.3}$$

using A as the device area, j as the operating current density and V the operating bias, the actual temperature inside the active region can be written as [Sca02]

$$T_{act} = T_{sink} + R_{th} \cdot A \cdot j \cdot V \cdot dc \tag{2.3.4}$$

with R_{th} being the thermal resistance. Under small temperature changes the heat resistance is assumed to be constant. The maximum operation temperature can then be written as [Fai95]:

$$T_{sink,max} = T_0 \cdot \left[ln\left(\frac{T_0}{R_{th} \cdot A \cdot j_{th} \cdot V_{th} \cdot dc} \right) - 1 \right] \tag{2.3.5}.$$

It can be seen now, that for high temperature, continuous wave operation (*dc* equals one in this case) a high characteristic temperature T_0 is required, but also low threshold power and low thermal resistance. This internal heating also influences the pulsed behavior, as previously described in the subchapter about pulsed laser characteristics. The duty cycle has to be taken into account: the length of each pulse, as the device experiences a transient heating, corresponds to an average heating and an instantaneous heating. Therefore the equation 2.3.4 also allows evaluating the real temperature of a pulsed device. For power measurements for example, duty cycles of 0.3 to 1.0 % are used with electrical input powers up to 70 W. Taking a regular heat resistance for the standard pulsed process and setup of 40 K/W or more, the average temperature increases between 8 and 28 K above the heat sink temperature.

2.7.3 Material dependent thermal conductivity

In general, the thermal resistance is reciprocal proportional to the thermal conductivity, similar to the electric description of resistance and conductivity. In case of a quantum cascade laser, which uses ternary alloys and a superlattice of different alloys, the thermal conductance in the active region is expectedly low compared to bulk alloys, binaries and especially metals.

Quantum cascade lasers are thin film devices and therefore the thermal conductivity in growth direction is the decisive factor [Lop06][Le08]. The decrease in thermal conductivity between the ternary alloys themselves and the superlattice is found in the interfaces between each layer. In table 2.3.1 different materials and their heat conductivity are shown, which were used for thermal steady state analysis.

Material	λ (W/m·K)	Ref
Au	300	
Au electroplated	150	assumed
InP	68	[Sca02]
GaSb	33	[Bor02]
InAs	27	from Ioeffe
GaInAs	5	[Lop06]
GaInAs/AlInAs	2	[Lop06]
GaInAsSb	6	estimated from [Bot89]
InAsSb/GaSb	2	assumed
$Al_{0.5}Ga_{0.5}AsSb$	7.7	[Bor02]
SiO_2	1.4	amorph, [Lop06]
Si_3N_4	30	single crystal

Tab 2.3.1: Thermal conductivity of different materials at room temperature

It can be seen, that the whole optical and electrical design of a quantum cascade laser has an influence on the thermal design. Especially the high thermal resistance of the active region, due to the required quantum well and barrier superlattice, is nearly unavoidable. In combination with high threshold powers, compared to regular quantum well lasers, sufficient heat removal can only be

achieved by keeping the active volume small and bringing good heat conductive materials close to the active region. For achieving this, two different approaches can be chosen. Either one performs an insulating InP overgrowth or one sticks to classically narrow mesas, with sufficient passivation and thick electroplated gold heat sinks. Both possibilities are discussed in the continuous wave chapter of this thesis.

2.7.4 Finite element analysis of thermal designs

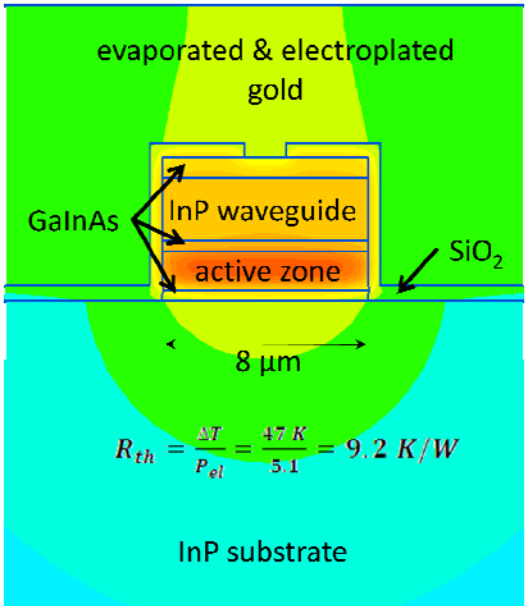

Fig 2-3-1: Thermal analysis of a electro plated, epi-side up mounted device

This subchapter will discuss the thermal analysis by the finite element method. It will not describe the method at all, but show different designs in terms of materials and geometry, which have been analyzed with Quickfield.

The InP based mid infrared devices are the most interesting ones for room temperature, continuous wave operation. They operate in pulsed operation up to 200°C, with watt-level output power at room temperature and characteristic temperatures in the range of 100 K to 200 K. Additionally the InP waveguide offers a good thermal conductivity on both sides of the active region. Figure 2-3-1 shows an epi-side up device's cross section, for a mesa width of 8 µm. The thickness of each active zone is 1.6 µm.

The 600 nm passivation was assumed to be silicon dioxide beneath 4 µm of electroplated gold. The design of the waveguide is described in subchapter 2.5.1, while the active zone design was introduced in subchapter 2.3.2. The boundary conditions of the simulation were set to:

- constantly dissipated power within the active region corresponding to 100 % of the threshold power at room temperature
- a constant heat sink temperature of 300 K either at the bottom of the substrate or the top of the electroplated gold

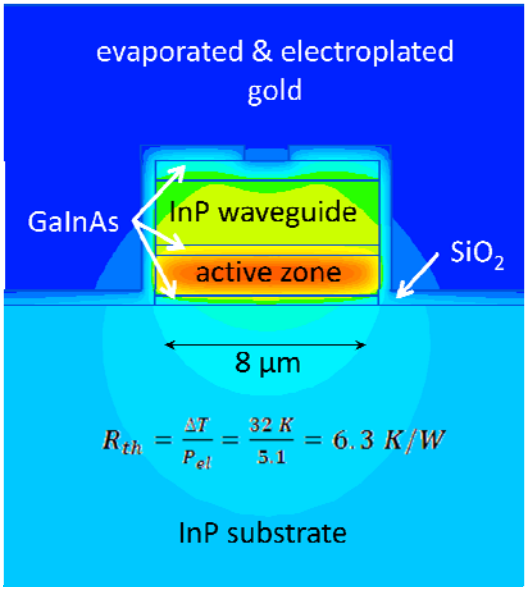

Fig 2-3-2: Thermal analysis of a electro plated, epi-side down mounted device

For figure 2-3-1 the result yielded an overall thermal resistance of 9.2 K/W. For improved heat removal, the epitaxial layer can also be mounted down facing (epi-side down). This is shown in figure 2-3-2, with the defined heat sink being on top of the structure. The device geometry is the same as in figure 2-3-1. Overall it yields a thermal resistance of 6.3 K/W, significantly lower than the regular set up.

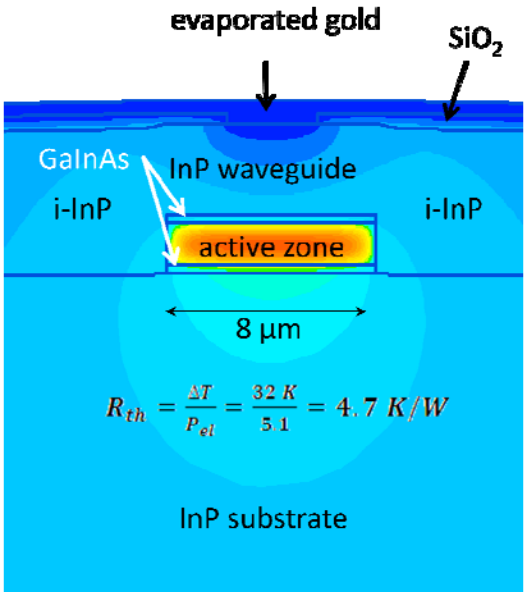

Fig 2-3-3: Thermal analysis of a InP overgrown, epi-side down mounted device.

As mentioned before, instead of using electroplated gold, the heat removal can be done by overgrowth of insulating InP (see figure 2-3-3). The thermal resistance decreases to 4.7 K/W for the overgrown sample assuming the same active region design.

When further reducing the mesa width, the dielectric thickness has to be increased to avoid increasing losses caused by the gold. This is problematic, as thicker dielectric will reduce the lateral heat removal on one side, but also could break due to deposition induced strain. In case of InP this is not required, as the wave gets attenuated in the InP overgrowth. The challenges at overgrowth can be found in avoiding valence band absorption, caused by p-doped blocking layers, and in the reduction of parallel leakage paths. Most successful overgrowth is performed with semi-insulating iron-doped InP.

It also has to be mentioned, that no additional thermal resistances of the setup are included, which unfortunately doesn't hold true as soon as real device setups are investigated. With simple setup technology which is used for pulsed setup, easily 12-15 K/W are added. Similar to high power quantum well lasers, achieving good performance and lifetime becomes more an industrial packaging and soldering problem, as the monolithic heat resistances are quiet low.

Process Technology

This chapter, in contrary to the previous one, which was mainly focused on theoretical aspects and material properties, will describe the details about epitaxial growth, edge emitter processes and sample setup technology but also the measurement systems which are used for characterization. Besides describing the general principles, also specific issues are mentioned, which could be interesting for following workers in this field but also show potential improvements which could be done in the future. The subchapters are arranged following the general process sequence, giving the reader an idea of the device fabrication and characterization flow.

3.1 Molecular Beam Epitaxy of Devices

After having designed a quantum cascade laser for the mid or the far infrared, the device has to be grown inside an epitaxy machine. Due to its versatile application of different material compositions with very good interface control, the molecular beam epitaxy (*MBE*) (see figure 3-1-1, [ETH09]) is the best choice, although quite successful devices have been grown with metal-organic vapor phase epitaxy lately [Gre04][Wan07][Bla07].

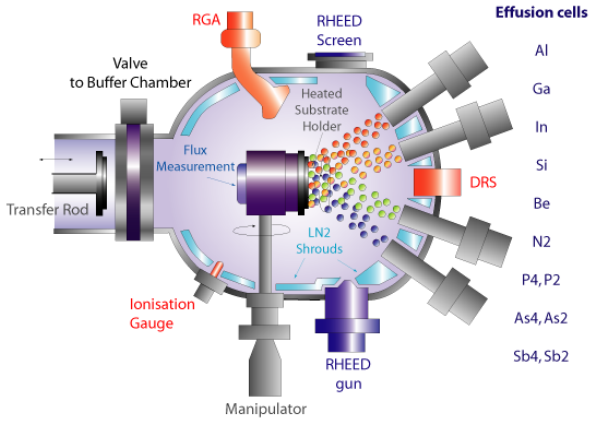

Fig 3-1-1: molecular beam epitaxy, schematics with sources and in-situ control

In principle, the molecular beam epitaxy works by controlling the elementary flux ratios of different materials like aluminum, gallium, indium or arsenic, which then combine into a specific alloy on a substrate. By controlling the temperatures of the individual material cells, the composition is controlled while movable shutters are used for growing alternating layers of different materials. For establishing homogenous deposition on the substrate, it rotates, while an ultrahigh vacuum (~ 10^{-11} torr) guarantees low defects and long mean-free path for the beam coils. The limitations, which arise from the epitaxial side, are due to requirement of operating the material cells (*Knudson cells*) under constant flux. This constant flux is required, since the superlattice structure of any quantum cascade laser can only be controlled by shutters, which can open and close within 0.1 s, while flux changes are much slower. Due to this constrain, the amount of different material compositions which can be grown as alternating stack is limited. Table 3.1.1 shows constant flux rates, in monolayers per second, for the phosphide-MBE system and the corresponding material compositions which can be achieved.

For achieving good interface quality, the group-V component should be only consisting of a single element like As or P, which are used in oversaturation to avoid metallic formations of group-III elements. In case of two required group-V elements, they should have a constant ratio throughout the active region. In case of InP based devices this can be easily done by using only the materials from the AlGaInAs system (see table 3.1.1) inside the active zone. For the GaSb related compounds (see subchapter 2.2.1) the side bands force to use mixed group-V compounds or at least different ratios of them.

	Cell	Ga (ML/s)	Al1 (ML/s)	Al2 (ML/s)	In (ML/s)	As (-)
Composition						100 %
AlAs				0.5811		100 %
$Al_{0.635}In_{0.365}As$			0.5255	0.5811	0.6360	100 %
$Al_{0.48}In_{0.52}As$				0.5811	0.6360	100 %
$Ga_{0.4}In_{0.6}As$		0.4240			0.6360	100 %
InAs					0.6360	100 %

Tab 3.1.1: Composition limited by MBE cells. Top line shows the different material cells of which only Al exists twice, while the fields indicate the rate in monolayers per second. During a quantum cascade laser growth the growth rate cannot be changed, and therefore only a few material compositions can be used.

Besides limited amount of different alloys, which can be grown, also the precision can be an issue. Since most quantum cascade lasers require above 1 µm thick lattice matched or even strain-compensated alternating stacks, strain can accumulate for different reasons. Strain can be created by imperfect interfaces or the slightly mismatch of the compositions, especially when they are ternary or quaternary. Overall the strain must be below 0.1 % for stacks around 1 µm and even below for the 10 µm thick active zones of far infrared devices. Assuming an accuracy of 1 % for the compositions, an random induced lattice mismatch in the order of 10^{-4} can be expected, just one order below the critical limit. On the other side, the quality of the growth has to be controlled and approved.

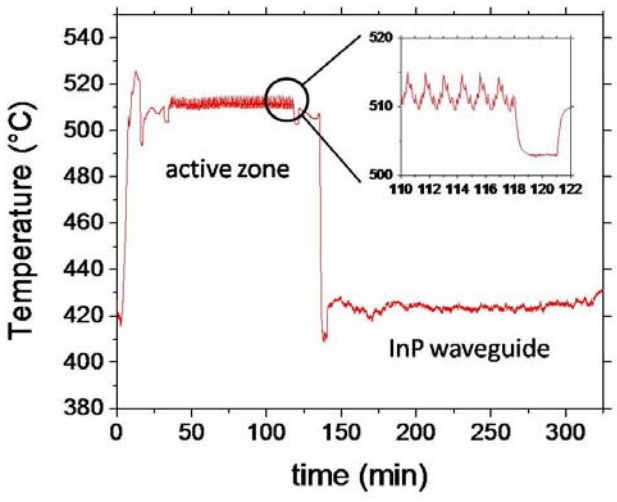

Fig 3-1-2: pyrometer signal for a mid infrared InP based quantum cascade laser, inset shows focus in active zone

Growth control during and after the process

There are some control possibilities during and after growth, which can be used to analyze the quality of the sample before processing or in case of contradictionary results afterwards. The in-situ control is done by monitoring shutter movements, temperature of the sources and most important, the pyrometer signal of the substrate. Figure 3-1-2 shows a pyrometer signal curve in general and a focus into the active region. In general, different material compositions require different growth temperatures, which can be seen between the AlGaInAs active zone and the InP waveguide. A good hint on the morphology is given by the stability of this curve, especially during the active zone, which should oscillate around a certain temperature. In the focused region, which shows six repetitions of the active zone design, each shutter movement can be seen by a small spike, which is caused by the heat radiation of each cell. The temperature oscillates during one sequence over roughly five degree, depending on the different cell temperatures.

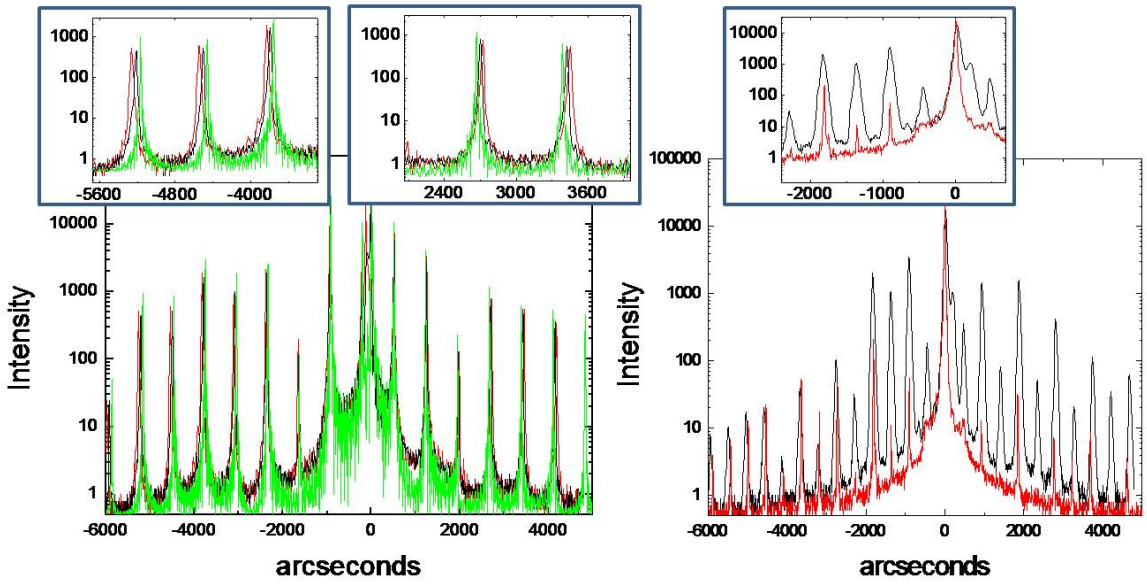

Fig 3-1-3: X-ray diffraction measurements for mid infrared devices (left) and far infrared devices (right). The smaller graphs show focused regions of the larger overall measurements.

Besides the in situ analysis, the exact compositions for ternary compositions and a hint on the interface quality can be determined by the X-ray diffraction (*XRD*) analysis. Especially with strained structures, it can give a clue on possible problems, but unfortunately it is not always easily interpreted. Figure 3-1-3 shows four different X-ray diffraction measurements being done. The mid infrared devices (left) are having the same design, which is simulated (green curve) for comparison to the results being obtained (red and black curve). The overall *XRD* measurement is shown, while two insets show the compressive strained side (left) and the tensile strained side (right). A newly grown sample (black curve) is compared with an older sample (red curve). In general, the linewidth of the peaks corresponds to the number of periods, but also to the morphology like the interface quality, while the distance between individual peaks is proportional to the used strain. All measurements are aligned to the substrate peak, in

this case InP, to be comparable. It can be seen, that in both cases the red curve is shifted further away in arcseconds from the corresponding green peak than the black line, showing that the compressive and the tensile strain are larger. This corresponds to higher indium fraction in the GaInAs well and higher aluminum fraction in the AlInAs barriers. From the device performance, this can be seen by the shift in emission wavelengths from roughly 7.1 µm (red sample) to 7.6 µm (black sample) and a change in threshold voltage and current density. Paradoxically, the red sample shows the lower threshold current density although being further away from the expected simulation, while the black sample shows higher output power. Both of these samples are within a normal deviation, which can be only further reduced by intensive calibration before every single growth.

Simpler in interpretation are severe problems, which can be seen in the right *XRD* measurement for two far infrared designs, with a small inset focused on fewer peaks. The lattice matched grown sample (red line) using ternary compounds shows sharp peaks while a strain balanced quaternary-ternary sample (black line) only has broad peaks (black line). In this case, the *XRD* clearly shows the quality of the growth, but unfortunately the ternary AlInAs barrier in contrast to the quaternary AlGaInAs barrier has a much larger conduction band offset and is therefore less suitable for far infrared designs. Especially for the large stacks (~ 10 µm) being required for far infrared devices, the growth performance is critical on achieving any lasing performance.

3.2 Process Technology of Devices for the mid and far infrared

This subchapter describes the required process steps for transforming an epitaxial sample into a ridge waveguide for optical characterization. It is separated into different topics, describing the standard process for pulsed applications and the development of different continuous wave processes. Additionally different facet treatments are mentioned, which were used for high-reflectivity coatings. The far infrared process and major parts of the continuous wave process had to be developed within this thesis and still rely on problematic steps, which are far away from industry standards regarding yield and reliability. Some important issues will be pointed out, during the next subchapters to help future workers at the walter-schottky institute to avoid errors which have been done.

3.2.1 Standard process for mid infrared devices

This fast and reliable process has been developed by G. Scarpa already in 2001 and is still used for general characterization of pulsed devices in the mid infrared. In the following figure 3-2-1, the process is described by graphics and short comments.

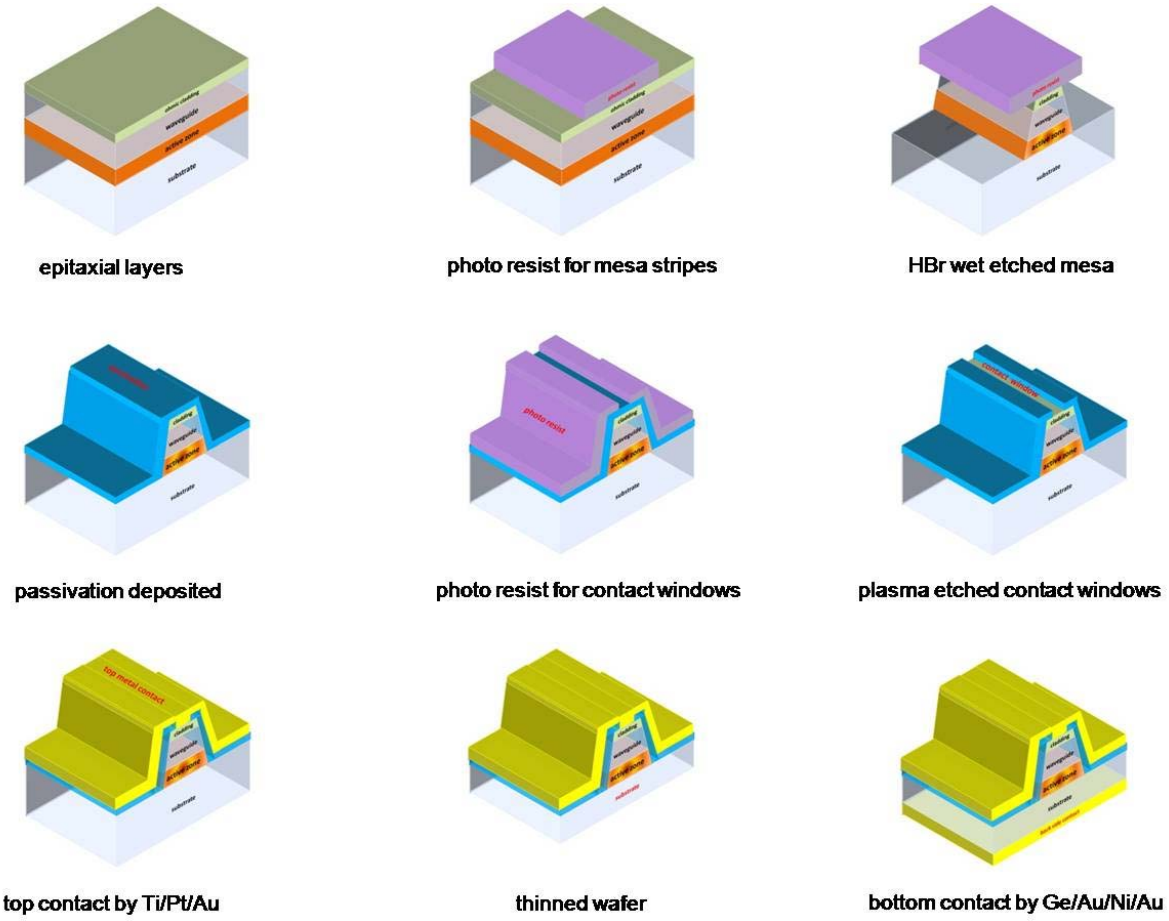

Fig 3-2-1: standard process for mid infrared devices based on InP

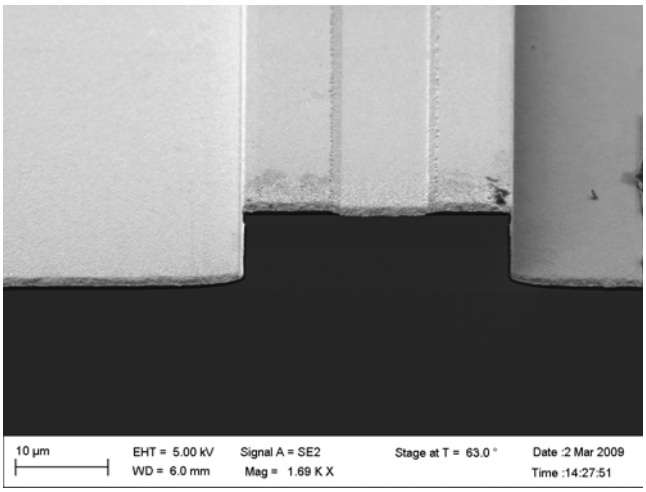

Fig 3-2-2: SEM picture of standard process done by reactive ion etching

In the standard process, the wet etching was done by hydrobromic acid and the passivation by sputtered silicon dioxide. Variations were done by using the chlorine based reactive ion etching system (*RIE*) for forming mesa stripes and silicon nitride passivation by plasma deposition (*PECVD*) (see figure 3-2-2). The device performance was not much different for these variations as long as broad mesa's (22, 26 and 30 µm) were used, but they allowed flexibility in processing. Important steps in this process are the alignment of the contact windows with the given lithographic system and the oxygen removal with hydrochloric acid before the evaporation of the top contact metallization. In case of far infrared devices, this process can also be applied with broader mesas, ranging from 50 to 200 µm, and plasmonic wave guidance on the top metallization. This process is the most reliable one, due to its broad mesas and therefore relatively wide contact windows and large tolerances in the range of 2 µm and more. It can be performed within 14 work-hours by an experienced process operator for a single sample, when all systems are running and free of other users.

3.2.2 Continuous wave process for mid infrared

In contrast to all other processes before, the continuous wave operation requires besides good waveguiding and excellent electrical performance also a good thermal management. To some part the thermal resistance is already predetermined by the chosen materials for the active region and the waveguide. On the other side, the active volume, which is defined by the thickness of the active region, the width of the mesa stripes and the length of the resonator are defined by the growth and process design. The heat sink itself can be created by either InP overgrowth (see chapter 2.7 *Thermal Properties and Design*) or electro-plated gold. Unfortunately also the setup technology can increase the thermal resistance, but will be explained in the next chapter.

Even a quantum cascade laser with good electrical performance, will have a threshold power (assuming 25 µm wide mesa) of around 10 to 12 Watt. Taking this value and assuming a very good characteristic temperature T_0 of 200 K, a heat resistance below 1.5 K/W would be required for reaching room temperature continuous wave operation (equation 2.3.5). This small example shows, that the power quantum cascade lasers dissipate is massive, compared to standard quantum well lasers and that a very good thermal management is always required. For reducing the required power, the reduction of the mesa width is the most important factor, already mentioned before. There are some constrains though, which limit the mesa width. In general, wet etched mesas have a better quality and therefore lower threshold powers. Unfortunately wet etching is to some degree isotropic, which means that at best for

every micrometer being etched down, an underetch of 600 nm has to be taken into account. With a suitable waveguide thickness of 3.5 µm and additional 1.5 µm for the active zone, which also has to be etched since current spreading cannot be allowed for low threshold powers, an estimated underetch of

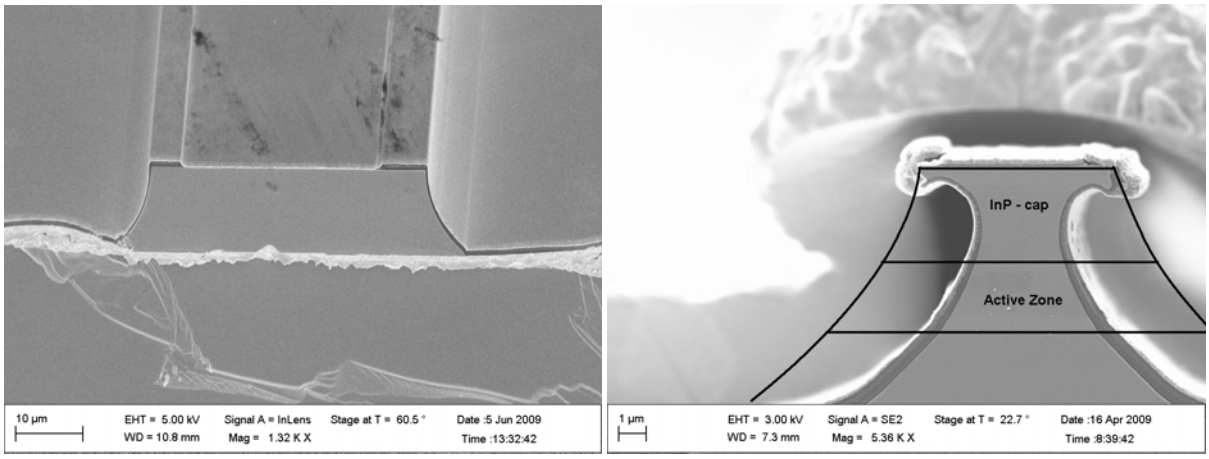

Fig 3-2-4: SEM pictures of the metal-metal waveguide (left) shows a well cleaved facette, while the substrate itself is not perfectly cleaved at all. The bright line beneath the mesa (~ 40 µm) is the roughly 1 µm thick $Au_{0.8}Sn_{0.2}$ eutektikum, which was sandwiched between a Ti/Pt and a Ti/Pt/Au/Pt layer. The right pictures shows an extremly underetched continuous wave process using the combination of dry and wet etching. The top contact window and the active zone are both about 4 µm wide, while the InP waveguide, due to a little higher wet etching rate, is stronger underetched. The black solid lines indicate the mesa structure for an only wet etched process, with an limit of roughly 8 µm for the active region.

3 µm per mesa side is expected. Since the available lithographic system has a tolerance of about 0.7 µm and a minimum feature size of 0.8 µm, the remaining contact width yields about 2 µm. For a less critical process this should be extended to 3 to 4 µm, resulting in an minimum effective active zone width of 8 to 10 µm for a wet etched process, corresponding to an maximum thermal resistance of 4.2 K/W. To avoid this limitation, a new process, combining dry etching for small mesa widths and wet etching for good interface quality, had to be developed. Using a silicon nitride hard mask, mesas between 5 and 12 µm are etched using a chlorine reactive ion etching system through the whole active region. After this step, the lasers are wet etched mostly for further width reduction in combination with a smoothening effect down to 4 µm. At this point two other limitations come into play. The smaller the mesa, the further the wave will penetrate into the lateral dielectrics which are used as passivation. This reduces the lateral confinement, which was taken as 100 % for wide mesas, but also increases the passivation thickness, which is required for keeping the wave away from the metallization. Additionally thick passivation layers will increase the thermal resistances and bear the risk of strain induced cracking; therefore they should be avoided if possible.

In figure 3-2-4, scanning electron microscope pictures of the two newly developed processes are shown. These pictures also indicate possible issues, which are still requiring future development. It has to be mentioned that the sample from the right picture showed a record low threshold power of about

2.4 W, but unfortunately had an drastically increased thermal resistance of 16 K/W limiting its continuous wave operation to 310 K [Kat09b]. Future processes reduced the thermal resistance further and improved the performance at room temperature under continuous wave operation of injectorless devices.

3.2.3 Facet treatment for high reflective coatings

There are different methods for increasing the performance of a laser. Most common are high reflectivity (*HR*) coatings on the unused facet. During this work, these *HR*-coatings were done either by distributed bragg reflectors (*DBR*) (see equation 2.2.12b) using alternating layers of amorphous silicon ($n \approx 3.4$) and zinc-sulfide ($n \approx 2.3$) or by metallic mirrors. In the case of *DBR*s, the strain inside the dielectric layers in combination with the required thickness ($d_{ZnS} \sim 0.76$ µm) made them unreliable and at best 2 pairs could be deposited on a cleaved facet, yielding a reflectivity of 88 %.

Using metallic mirrors reduces the required thickness drastically. The applied layers were amorphous silicion for insulation and then a thin titan layer for sticking covered by roughly 100 nm of gold. Unfortunately evaporating metal on cleaved facets shortens all lasers, which requires afterwards additional cleaving and cutting steps to separate them again resulting in lower yield.

3.3 Setup Technology of Devices

After having finished processing the devices, they need to be setup, which seems simple, but can also contain issues, one would not have thought about before. First of all, professional sample cleavers and laser mounts were not available at this work, making the laser setup a manual work and especially frustrating for setups, which require a good thermal management. Therefore this chapter will describe the setup technology which was at hand from the beginning on, and the search for better solutions.

3.3.1 Standard setup for pulsed devices in the mid infrared

For pulsed measurements in the liquid nitrogen cryostat, samples were cleaved into bars of 1 to 4 mm in length, and 9 to 18 stripes (depending on mask layout). A thin tin foil (~ 30 µm, most likely thinner foils would do better for lower thermal resistance) was cut by a scalpel to an equal size of the sample. A highly doped silicon wafer, evaporated with Ti/Au (40/200 nm) and cleaved into small submounts of roughly 18 mm times 5 mm in size, is then used with the foil in between to anneal the sample onto it. The whole submount is afterwards clamped on a larger copper heatsink, which features a bond pad. Figure 3-3-1 shows this setup for two times 18 laser bars of 4 mm length. This setup has roughly a thermal resistance of 15 K/W, excluding the laser itself, and is therefore unsuitable for continous wave operation at room temperature.

Fig 3-3-1: standard setup for mid infrared devices in pulsed operation

Two of these copper heatsinks can be mounted back to back onto a cold finger of the liquid nitrogen cryostat, enabling up to 16 lasers being measured during one cooling cycle.

3.3.2 Continuous wave setups

The first continuous wave operation [Kat08b], which was limited to temperatures below 200 K, was achieved on the standard pulsed setup. This had to be optimized for futher improving the maximum temperature of operation. By using professionally manufactured heat sinks, which possess a 5 µm thick $Au_{0.8}Sn_{0.2}$ layer for annealing, the lasers could be mounted epi-side down directly on a gold covered copper heat sink. With this change, the thermal resistances could be reduced and the first injectorless room temperature continuous wave operation was shown [Kat09b]. Figure 3-3-2 shows the copper heat sink against which the small copper mounts were clamped by a small screw. The inlets show a top view of a setup sample and a small graphic of the mount itself.

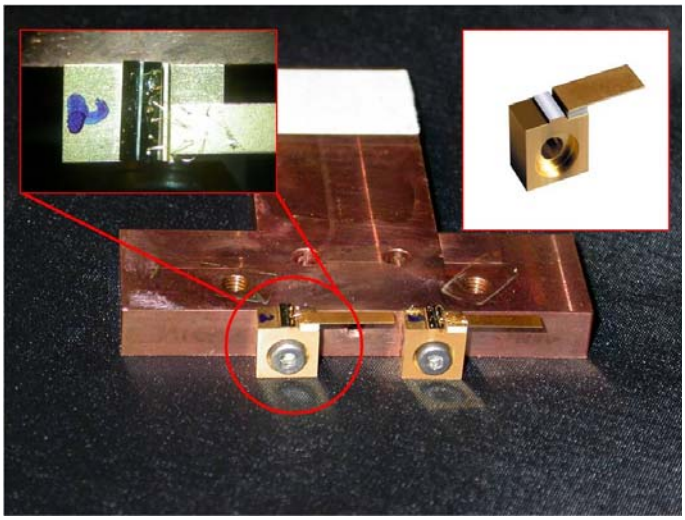

Fig 3-3-2: continuous wave mounting. Two mounts are screwed towards the larger copper heat sink. The left inlet shows a top view on two lasers mounted epi-side down and the right inlet shows the mount.

This setup is estimated to have a thermal resistance below 3 K/W. To further decrease the thermal resistance of the setup, the thickness of the gold-tin alloy has to be reduced and instead of copper, diamond or AlN mounts should be considered.

3.4 Characterization of Devices

This chapter describes all different methods of characterization, which have been done, while the results are presented in the next chapter. Before this work started, the measurement setup was limited to simple measurement of pulsed devices in the mid infrared, while spectra were recorded with an Oriel grating spectrometer.

3.4.1 Measurement setup for mid infrared devices

The whole setup moved to the back of our new fourier transformation infrared (*FTIR*) spectrometer built by bruker and was installed on a single rail. Figure 3-4-1 summarizes the measurement setup, while the next subchapter explains the different methods for measuring. For pulsed

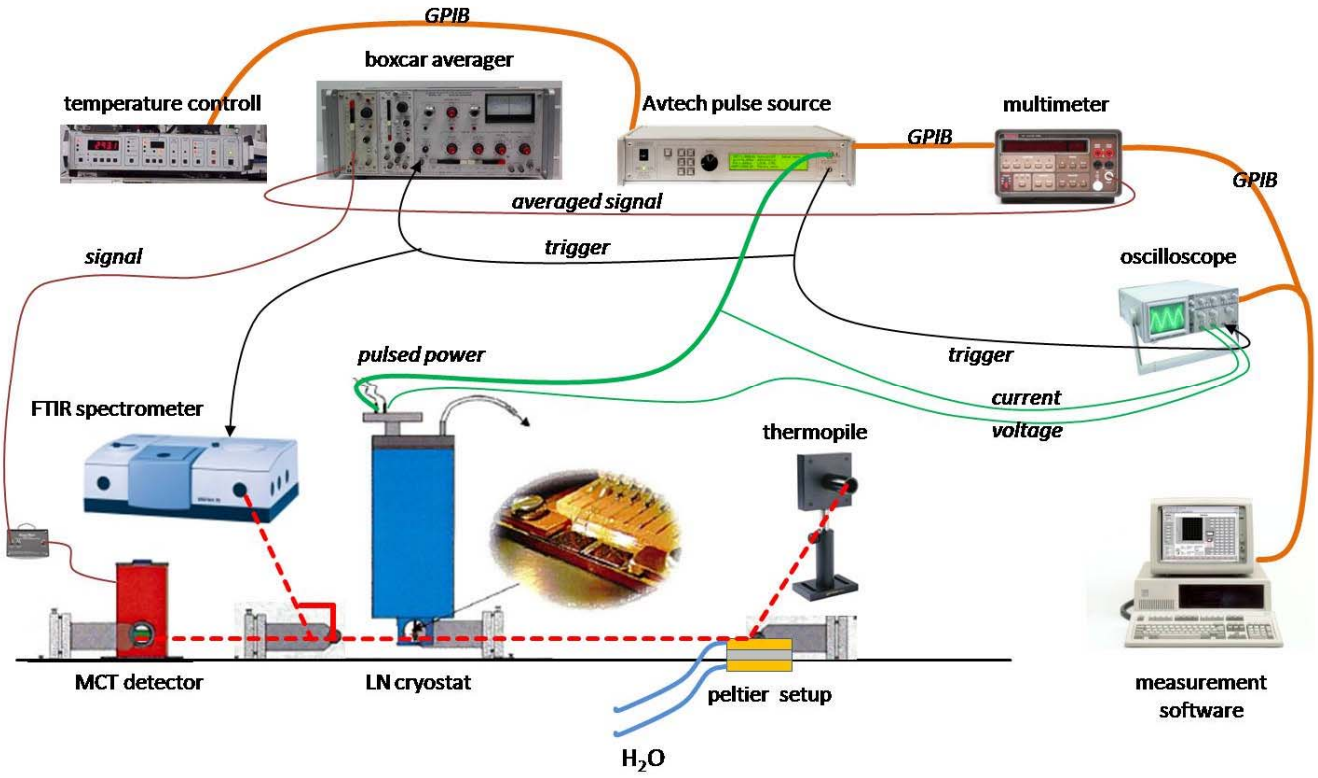

Fig 3-4-1: standard setup for mid infrared devices in pulsed and continuous wave operation

measurements, the cryostat (two window options with calcium fluoride and zinc sulfide) is used for controlling the sample temperature between 80 and 500 K, while a closely mounted mercury cadmium telluride (*MCT*) detector (from Judson Technologies) is used for measuring the light-current curves. The measurement itself uses a differentating preamplifier and an integration by a boxcar averager for higher sensitivtiy and lower noise levels. The lasers are controlled by an pulse source (Avtech 5B-B) capable of pulses between 100 ns and 100 µs, with duty cycles up to 1 %. Since most samples easily saturated the *MCT* detector, attenuators with 10, 1 and in combination 0.1 % transmission are used. The real power is

then calibrated using a thermopile detector (12 x 12 mm^2 detector area, from Gentec) directly in front of a laser facet, assuming 100 % collection efficiency. Spetra can be recorded with the *FTIR* (vertex70, Bruker Optics) via the fiber entrace with unmounted or mounted fibre coupler. The advantages of this system are the higher resolution, the possibility of step scan measurements, the auto callibration of the wavelengths and the wide choice of beam splitters and detectors.

For continous wave measurements, a water cooled temperature controllable peltier setup is used. This setup can use the same beam path than the cryostat, but with a regular preamplifier going into the multimeter. For power supply a direct current source (Detla elektronika) with up to 22 A and 70 V is used.

For recording the light-current-voltage characteristics of different devices, a selfmade labview programm is used. This programm can record single pulsed curves in the mid infrared (*MCT*) and far infrared (*pyroelectric detector*). Additionally single continuous wave curves and devices in pulsed operation over a predefined temperature range can be recorded, the latter automatically as the ITC 500 thermal controller is also accessible via the GPIB bus.

3.4.2 Measurement techniques for mid infrared devices

This subchapter is mostly written for students to help them getting into the topic of measuring mid infrared devices, especially with our current setup and therefore will be crowded with measurement details, most other readers will find boring and therefore are encouraged to skip. On the other side, it is describing how the devices were characterized, revealing weaknesses and strengths of the different methods.

Pulsed measurement of LIV-characteristics

All grown devices were processed into standard ridge waveguides for pulsed measurements. Pulsed operation enables to quickly check on the device performance, regarding wavelength, thresholds and efficiencies only depending on the optical and electrical design.

A pulsed measurement can start, when the mounted and bonded samples are evacuated and cooled down to liquid nitrogen temperature. (The filling of the cryostat is done by pressured nitrogen being blown into the liquid nitrogen Dewar, pushing the liquid nitrogen finally into the designated chamber.) If not yet done, the boxcar has to be calibrated (after at least thirty minutes of warm up phase) by unplugging all wires and setting the bias to zero (it's a potentiometer with a control screw) at the shortest time scale. Afterwards all cables are reconnected and the zero output voltage and the maximum output voltage have to be set to 0 and -10 V.

In pulsed operation, the internal resistors at the oscilloscope are chosen to be 50 Ω for the current forge and 1 MΩ for the laser voltage. In case the values seem not to be reasonable, the averaging between the gating bars has to be turned on. The position of the bars has to be chosen carefully, as deviations can give different results. For 250 ns pulses, which were used most of the time and always in

earlier times, the bars were set to 108 and 264 ns, averaging roughly the last 150 ns of the pulse. This causes a slight error around 5 % in current compared to direct current and below 2 % for the voltage. For longer pulses, the bars can be shifted backwards, enabling a better accuracy but also higher internal heating. For measuring the threshold currents no attenuator is used, while a 10 % and 1 % attenuator are at hand for *LIV*-curves over the whole current range.

Continuous wave measurement of LIV-charactersitics

For measuring continuous wave, the sample needs to be mounted on a professional stage (see subchapter 3.3.2) and placed on the peltier setup. If the maximum temperature of operation is below 0°C, it is possible to use the cryostat standard setup with a penalty of additional 10-15 K/W. For current the 0-22A dc source from elektronika can be used with minimum steps of 5 mA. The maximum current per wire is limited to 1 A, which requires parallel connecting for higher currents. It has to be mentioned, that the devices have to be connected before turning the output of the source on to avoid critical discharges. The preamplifier output has to be changed and directly connected to the multimeter.

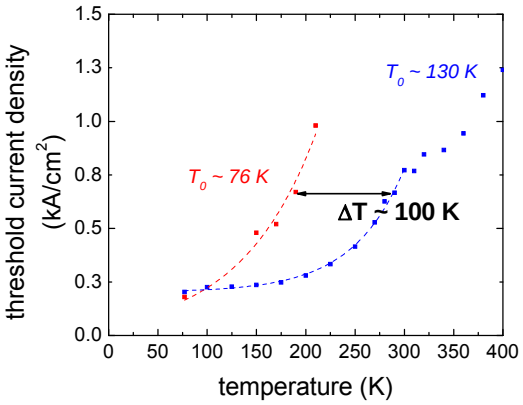

Fig 3-4-2: comparison of pulsed (blue) and continuous wave (red) thresholds over temperature

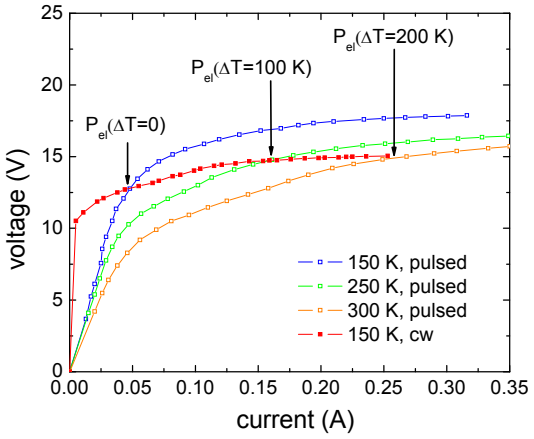

Fig 3-4-3: comparison of pulsed and continuous wave current-voltage characteristics for various temperatures

There are two ways of estimating the thermal resistance indirectly, as a direct measurement of temperature inside the active region is hardly achievable. If the devices lase under pulsed and continuous wave operation, the threshold currents can be directly compared. Figure 3-4-2 shows a comparison between pulsed and continuous wave measured thresholds versus temperature. Under continuous wave operation, the device reaches room temperature threshold already at 100 K lower heat sink temperature. The threshold power of 2.3 W corresponds to the thermal heating inside the active region and the device yields thermal resistance of 43 K/W, which is relatively high. The *CW* current density at 80 K show, that the pulsed values can be even slightly larger due to measurement setup.

In case the device does not work under continuous wave operation at all, the method of threshold comparison falls short. Therefore a second possibility was used, in which only the measured VI curves have to be compared. In case of QCLs, the heating inside the active region corresponds to line

broadening and lower required fields for equal tunnel currents. This leads to a general drop in voltage over temperature. This is valid as long as small currents and low serial and contact resistances are present and the path of current doesn't change in the active region. Figure 3-4-3 shows the comparison of pulsed curves at different temperatures and a continuous wave curve. For a rough estimation of the thermal resistance, the differences in electrical power between the intersections of the dc curve and the pulsed curves at 150 K and 300 K are taken. This yields a thermal resistance of 46 K/W, acceptable close to the previously estimated 43 K/W of the same device and standard setup.

Spectrum measurement

For measuring the emission wavelength of the device, the FTIR spectrometer (Bruker, vertex70) can be used, which allows high resolution (< 0.2 cm^{-1}) and high sensitivity in the mid infrared. Unfortunately it is not equipped with a bolometer, disabling spectral measurements in the far infrared. The alignment is done with two parabolic off-axis mirrors with f = 50 and f = 190 in mm, using the back entrance (shared with the removable fiber coupler). For pulsed measurements the repetition rate has to be chosen different from the mirror frequency to avoid measurement artifacts. While the insensitive deuterated triglycine sulfate (*DTGS*) pyroelectric detector is suitable for laser spectra, the mercury-cadmium-tellurid (*MCT*) detector has to be used for electroluminescence measurements as its sensitivity is by two orders of magnitude higher. Due to the very small dynamic range of the *MCT* detector, it is easily saturated when reaching threshold, producing strange results. Examples of different laser and electroluminescence spectra measurements are presented in the results chapter. Without the fiber coupler the effective resolution is reduced due to non parallel beam paths but the intensities are higher and the alignment is much simpler, suitable for fast low resolution scans.

Calibrated optical power measurement

The *LIV*-characteristics measured with the non calibrated thermopile, can be off by a large factor from the real values, due to not perfect alignment and noncalibrated power-voltage coefficients. The simplest approach for measuring calibrated output powers, yielding the slope and overall efficiencies, is done with a thermopile detector. The advantages of this detector are its large (12 mm · 12 mm) area and a relative sensitivity of 98% and higher over a very large wavelength range (200 nm to 11 µm). It is directly mounted in front of the laser facet (d < 6 mm) to ensure high collection efficiency. For reported and displayed powers, we assume 100 % collection efficiency, although it is most likely only 70 %. When measuring pulsed devices, the measured power value has to be divided by the duty cycle for achieving the average pulse power. It also has to be mentioned, that with 1 % duty cycle, the device heats up by 20 to 40 degree, reducing the performance. Unfortunately, the thermopile is very insensitive with a noise level of 5 µW, yielding a minimum detectable power with 0.25 % duty cycle of 4 mW, disabling very low duty cycles.

Gain spectrum measurement

For estimating the gain spectra versus current, the electroluminescence spectrum has to be recorded in the highest resolution possible. With clearly distinguishable intensity minima P^- and maxima P^+ of the Fabry-Pérot resonator, the gain can be extracted as shown by Hakki and Paoli [Hak73][Hak74] using

$$g - \alpha_i - \frac{1}{2L} ln\left(\frac{1}{R_1 R_2}\right) = \frac{1}{L} ln\left(\frac{\sqrt{P^+}-\sqrt{P^-}}{\sqrt{P^+}+\sqrt{P^-}}\right) \quad (3.4.1).$$

The difference between gain and overall losses decreases with increasing current, until finally reaching zero at threshold and clamping the gain. This measurement can be done in continuous operation, offering stable emission but also resulting in strong internal heating of the device. Alternatively pulsed operation can be used, performing an integration during a gated time slide using a pulsed sample and a transient recorder. This time slide is very important, as the device might start lasing during its first overshot at turn on and the thermal shift during the pulse might alter the measured signal. The weak electroluminescence of quantum cascade lasers, due to the lifetimes in the range of picoseconds, makes it very hard to successfully apply this method as the intensity minima are often at the noise level. A more sophisticated one is the direct measurement of the gain spectra by using multisection cavities as applied by Gresch on *QCLs* [Gre09]. One drawback of this method can be found in the not so high coupling efficiencies between the sections and the additional required process.

Results and Discussion

This chapter will describe the different devices, their performance and give an insight into possible drawbacks or improvements. As many applications require different key parameters for performance, different aspects of the devices were investigated. In general, all devices require low thresholds, high efficiencies and output powers at exactly designed wavelengths, at best. Unfortunately one contradicts the other, as for example low threshold performance is achieved by low doping for reduced waveguide losses. With a reduced doping, the negative differential resistance occurs earlier (see equation 2.2.20b) and the optical power and efficiency gets reduced. When trying to achieve a large tunability of a device, a broad gain spectrum is required which increases the threshold current density on the other side. Therefore the next subchapters focus on specific aspects of performance and show the best performing devices regarding this key parameter.

4.1 Low threshold devices

For a better comparison of the achievements, the best performance of injectorless devices at the beginning of this thesis shall shortly be introduced here. Additionally it has to be emphasized, that future developments will improve the state of the art but for comparison of what has been achieved a known basis always help. As comparison basis, the best performance, regardless of the device design and doping levels, of previously designed injectorless devices are mentioned. Figure 4-1-1 shows the best

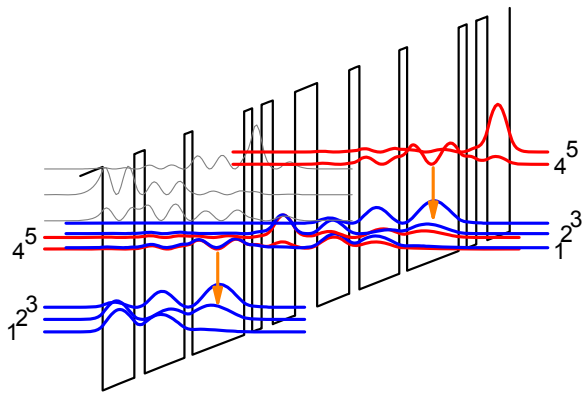

Fig 4-1-1: injectorless device based on two alloys, taken as reference for further improvements. States 1,2 and 3 indicate the lower states (blue) while state 4 and 5 indicate the upper states (red). The orange arrow indicates the transition.

$j_{th,300K}$	**0.73 kA/cm²**	**#1**
T_{max}	430 K	#2
T_0	90 K	#1
$P_{max,296K}$	**240 mW**	**#2**
WPE	**2.4 %**	**#2**
dP/dI	260 mW/A	#2

Tab 4.1.1: Summary of best performing injectorless devices (two different designs) using two alloys. WPE stands for wall plug efficiency.

performing design (quality ~ 36) which was developed by A. Friedrich. The active zone design is based on $Al_{0.635}In_{0.365}As$ and $Ga_{0.4}In_{0.6}As$ as barrier and well material, respectively. Additionally all devices were only capable of pulsed operation, although some efforts had been done to achieve continuous wave operation. Table 4.1.1 summarizes the best parameters for different designs and doping levels, none of the devices showed a combined overall performance, as indicated by different numbers.

4.1.1 Evolution optimized simple four alloy device

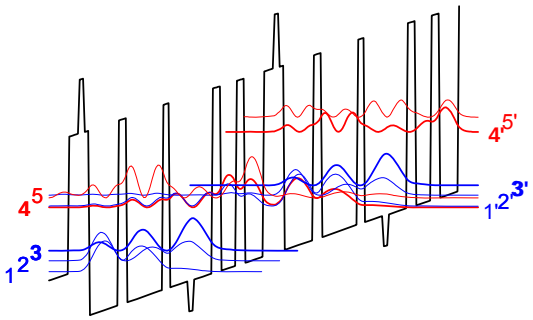

Fig 4-1-2: active region of the optimized design using four different compositions within the AlGaInAs system.

After implementing the evolution optimization algorithm, a first large scale run was started on three different computers. The boundaries of the simulation were chosen to be close to the design shown in figure 4-1-1 for comparability reasons, using an equal field, aiming for a similar emission wavelength and applying the same design scheme. The best calculated structure promised a 28 % higher gain coefficient than the reference. This design is shown in figure 4-1-2 (similar to fig 2-1-9, right). For comparability reasons the waveguide design was an exact copy of the reference one, regarding materials, thicknesses and doping levels and the active region was equally doped ($2.5 \cdot 10^{10}$ cm^{-2} as sheet doping density) and

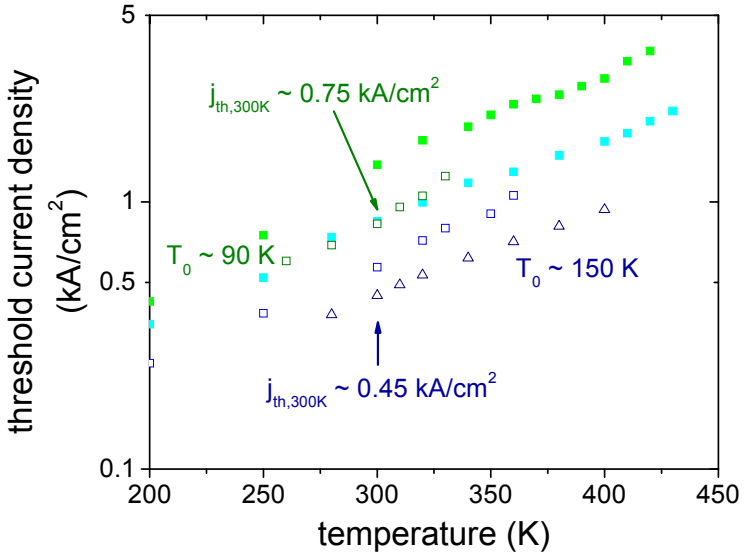

Fig 4-1-3: threshold current density versus temperature for two samples with the old design (green) and three samples of the new design (blue). Medium doped samples are filled and equally low doped samples hollow. The triangle indicates additional high reflective coating by ZnS/Si DBRs.

included the same number of repetitions (60 periods). This keeps the confinement of the active region at 55 %, yielding theoretical waveguide losses due to plasma absorption of 2.2 cm^{-1}, assuming bulk mobility's for each layer, mostly contributed by the waveguide and cladding layers. In a quantum

cascade laser, this value must be larger, due to the reduced mobility within the superlattice of the active region and the additional losses induced by intersubband absorption [Lya08].

The real difference can be actually found in the implementation of the thin AlAs barrier for increasing the temperature behavior on one side. The benefit of this barrier improvement was demonstrated before by Semtsiv [Sem02] and Friedrich [Fri07]. It is assumed that the increased barrier prevents carrier from being lost into the continuum due to the high electrical field. Another improvement was made by the InAs peak within the transition well, as InAs has a lower in-plane effective mass than GaInAs, therefore increasing the lifetime of the carriers. Both of these materials, like explained in chapter *"Materials for Design"* can only be used in very thin layers due to strain limitations. These additional materials in combination with the optimization algorithm lead to the performance shown in figure 4-1-3 in threshold current density over temperature for various samples. With equally low doping than reference sample #1, the threshold current density was decreased to 0.57 kA/cm^2, an improvement of 28 % regarding gain coefficient and threshold [Kat08]. This value is close to the prediction of the evolution algorithm. With an additional high reflective back facet coating, using two pairs of zinc sulfide and amorphous silicon, the pulsed room temperature threshold current density could be decreased to 0.45 kA/cm^2. This value is by a factor of 1.6 lower than any other quantum cascade lasers had shown so far [Boe09]. The characteristic temperature and the maximum temperature of operation were also improved from 90 K to 150 K and from 330 K to 360 K (low doped samples), respectively.

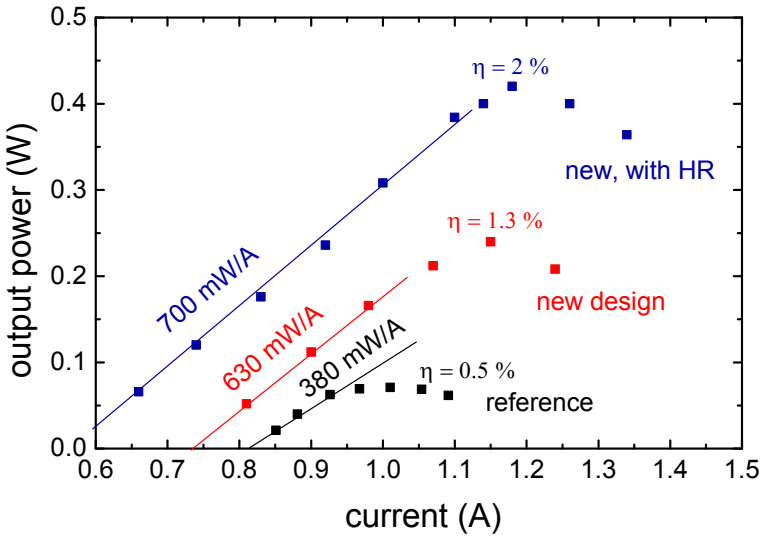

Fig 4-1-4: optical output power versus current for low doped samples of 4 mm in length and 26 µm in width. Both designs use the same waveguide and equal doping levels. η indicates the overall efficiency, also called wall-plug efficiency (*WPE*).

Another large improvement in design can be found when comparing the optical output power and overall power efficiency (figure 4-1-4). For the low doped samples the maximum power increased from roughly 70 mW to 240 mW, corresponding to an increase in wall-plug efficiency (*WPE*) from 0.5 % to 1.3 %. The slope efficiency dP/dI was also improved up to 630 mW/A. For the high-reflectivity coated sample the optical power and the wall-plug efficiency were increased furthermore to 420 mW and 2.0 %, respectively.

The measured waveguide losses were found to be around 4 cm^{-1}, for the sample with doping sheet density of $2.5 \cdot 10^{10}$ cm^{-2}, and roughly 5.5 cm^{-1} for the sample with $4.8 \cdot 10^{10}$ cm^{-2}. The corresponding absorption losses of the waveguide, which were similar in all cases, are calculated to be 2.0 cm^{-1}, indicating that 2.0 cm^{-1} of absorption result from the active core at low doping and 3.5 cm^{-1} at twice the doping. This yields 0.9 cm^{-1} for intersubband absorption, assuming no alteration by doping levels and growth fluctuations and 2.8 cm^{-1} for plasma absorption per $2.5 \cdot 10^{10}$ cm^{-2} in doping sheet density for this specific design.

4.1.2 Reproducibility of Growths and Sample Statistics

Besides growing many different samples during this thesis, most often a reference sample of the four-alloy design (see figure 4-1-2) was grown and processed as well. Overall there have been nine growths of this active region design, with variations in doping and waveguide. Figure 4-1-5 shows

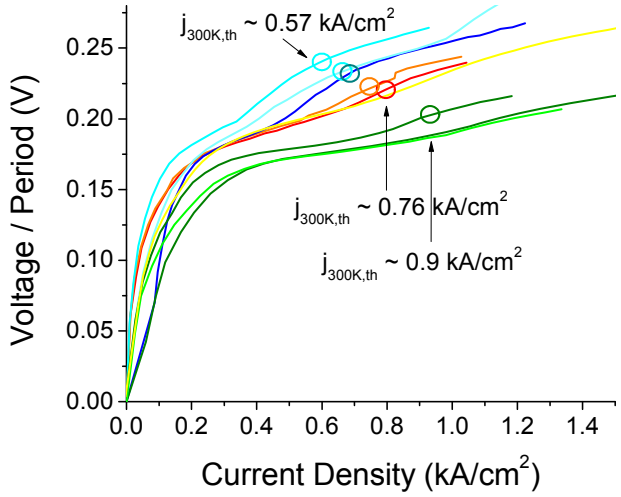

Fig 4-1-5: voltage per period for various samples of the four alloy design. The circles indicate the corresponding threshold current densities. The color of the lines indicates different doping levels for waveguide and active region but also different top contact materials like InP or GaInAs.

various voltage-per-period curves. Some of these curves, like the bright and dark blue lines, indicate low doped active regions, while green tones indicate samples with shifted wavelengths. From the voltage-per-period curves, a rough estimation of the emission wavelength can be done. With decreasing voltage, the resonance field will also decrease, emitting photons with slightly less energy at threshold. Deriving the real field inside the active region for each individual device would require processing every waveguide and cladding structure, without the corresponding active region and processing it for each design. This in depth evaluation was only done for the most often used waveguide design set (see subchapter voltage defect and injection behavior). Figure 4-1-6 shows the dependency of the voltage-per-period versus the emission wavelength close to threshold and corresponding *XRD* spectra.

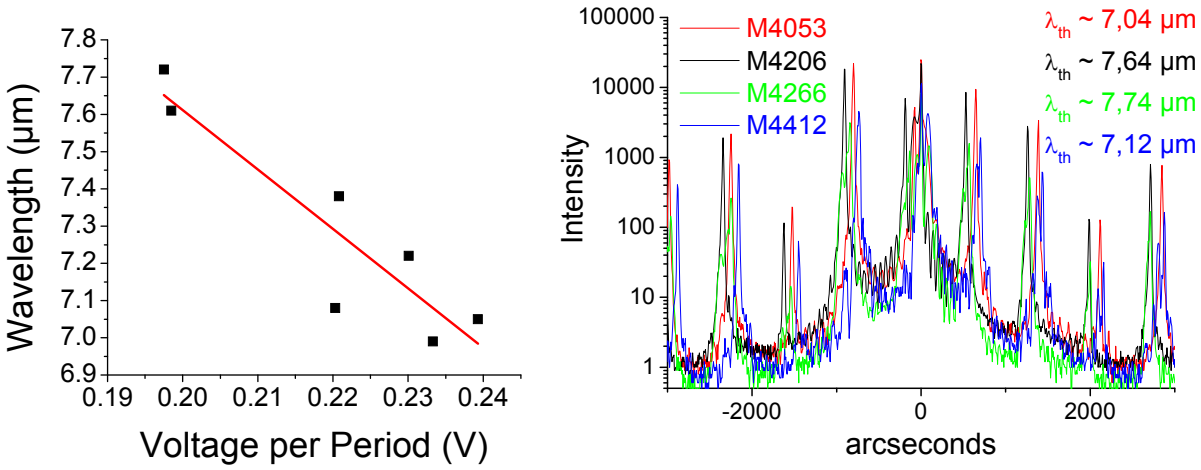

Fig 4-1-6: threshold emission wavelength (left) versus voltage per period and corresponding *XRD* spectra (right).

Sample M4053 and M4412 show similar tensile strain, while their compressive strain is different, although their emission wavelength is only 1 % in difference. The compressive strain of sample M4206 and sample M4412 are the furthest apart, although their emission wavelengths are separated less than those of M4053 and M4266. This indicates that the tensile strain is more critical on the emission wavelength than the compressive strain, but no further conclusions can be drawn from this.

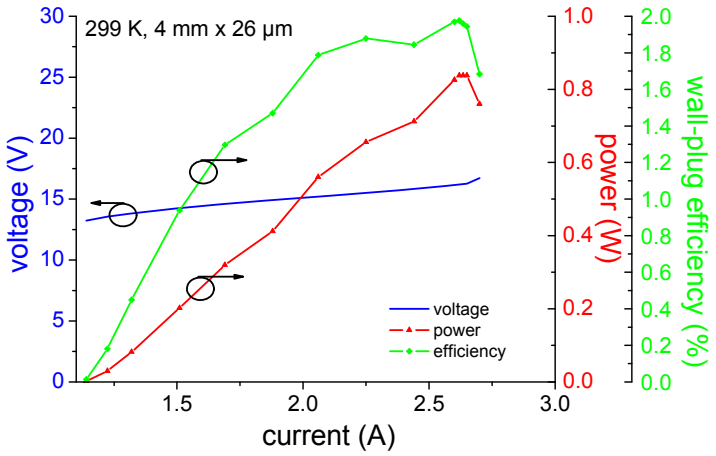

Fig 4-1-7: performance of the reference (green curves), which showed higher threshold current densities (20 %) but also much higher output power (100 %)

This shows that although the crystal quality is very good, slight changes in layer thickness and composition can alter the wavelength around its mean value of 7.29 µm with a standard deviation of less than 4 % over multiple *MBE* campaigns and about 2 % during a single campaign from growth to growth. While the threshold performance decreased for red shifted samples, their output performance strongly increased (see figure 4-1-7). This shows how sensitive quantum cascade lasers are to small growth deviations, which are unavoidable.

Since most other samples were only grown once or at best twice, no statistics could have been applied, therefore the measured values have to be taken with some uncertainty for the other growths. In case of direct comparability, like in the strong coupling experiments (see subchapter 4-4-3) the simple four alloy design was grown as reference structure directly before or after the new sample.

4.1.3 Gain Spectra of Injectorless Devices

The gain of a laser medium is a very important figure of merit, critical for good performance and low threshold current densities. As indicated by equation 2.1.6, injectorless devices with equally good design, should exhibit a twice as high gain as injectorbased device, due to the shorter length of the period. To measure the gain, two different methods can be applied. The 1/L method is done by measuring the threshold current densities of various devices with different lengths. From these values, the waveguide losses and the gain coefficient can be derived. This method is also suitable for devices only capable of pulsed operation. The 1/L method is limited to the linear fit value of the gain coefficient, which is normally identically to the gain measured by the Hakki-Paoli-method [Hak74], as shown by C. Sirtori et al. [Sir97]. Additionally the 1/L-method doesn't offer any information about the spectral behavior of the gain.

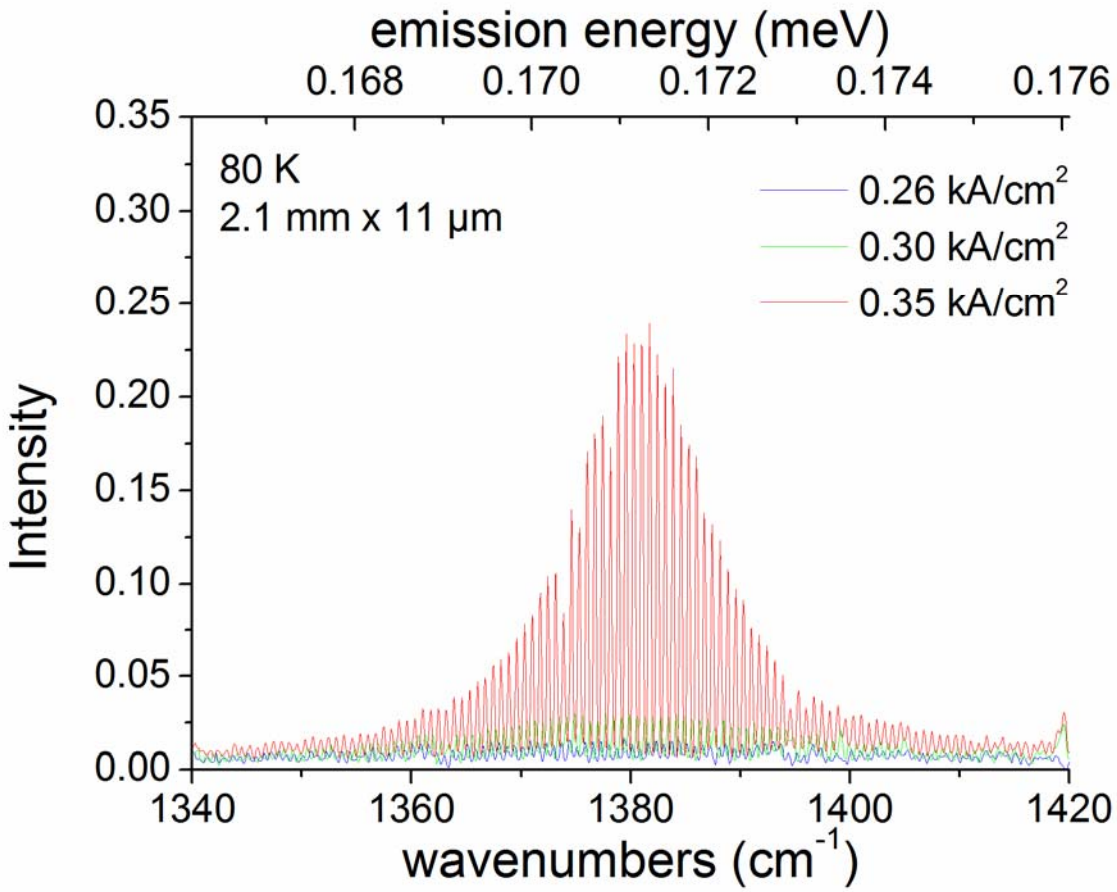

Fig 4-1-8: electroluminescence spectra at 80 K of a 2.1 mm long and 11 µm wide cw operating device.

In combination with a reliable continuous wave process (see subchapter 4-2-4) the sample presented above (design see figure 4-1-2) was spectrally measured below threshold at different heat sink temperatures under continuous wave operation. The Hakki-Paoli-method requires a high resolution to distinguish between the Fabry-Pérot maxima and minima of the gain spectrum. Due to the very short

carrier lifetimes, the electroluminescence signals of quantum cascade lasers are very weak. Therefore the high resolution can only be achieved by perfect alignment and long integration times for improved signal to noise ratios. Figure 4-1-8 shows the measured electroluminescence of a 2.1 mm long and 11 µm wide sample, operated in continuous wave below threshold (*0.357 kA/cm²*) at an heat sink temperature of 80 K.

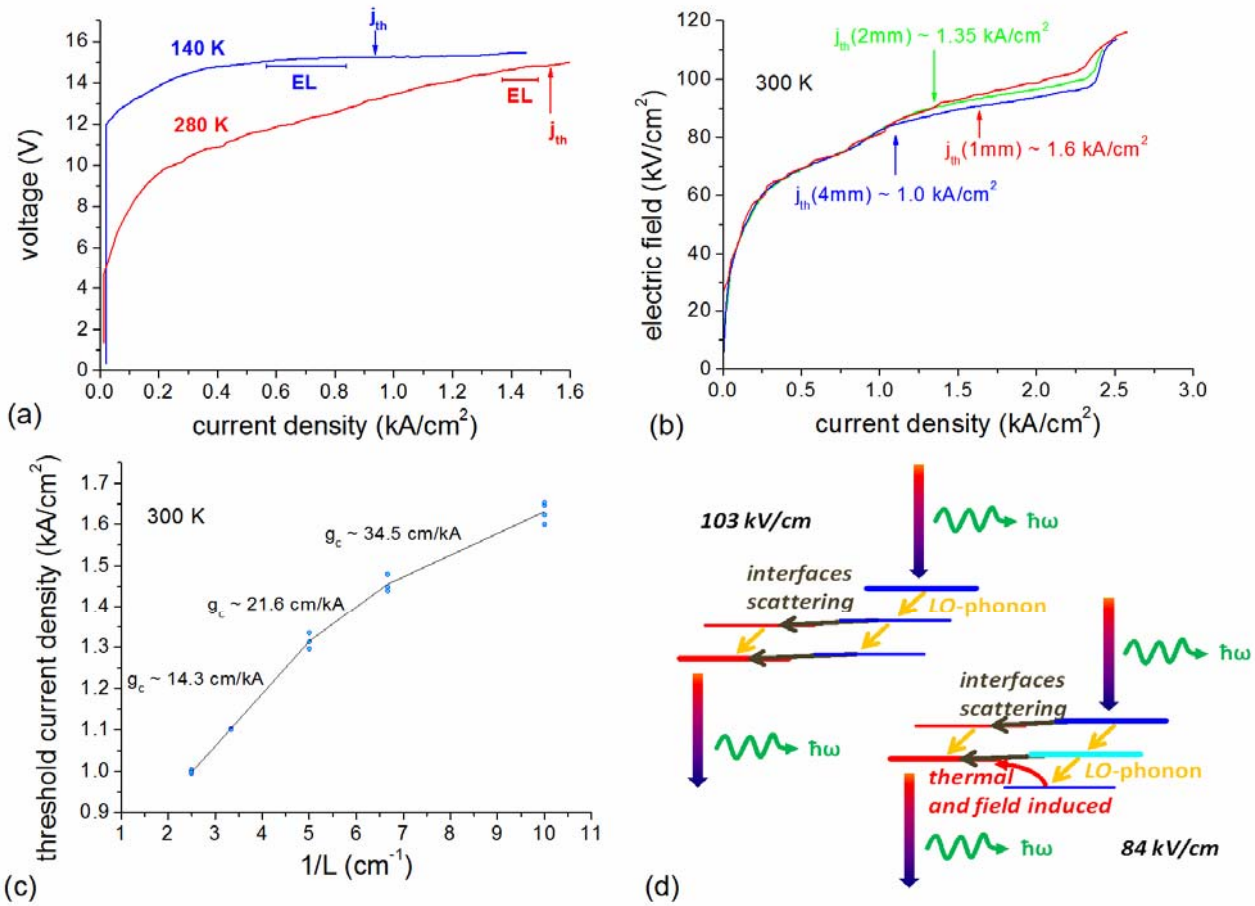

Fig 4-1-9: The cw voltage-current characteristics for 140 K and 280 K are shown. Small arrows indicate the threshold, while the bar indicates the range in which the electroluminescences measurements were performed (a). Applied electric field inside the active region presented for 4, 2 and 1 mm long devices. The clamping at different fields leads to the splitting of the characteristics (b). The non-constant gain coefficient, with two linear fits (c). The resonant scheme for the design field (103 kV/cm) and a configuration at lower field (84 kV/cm) (d).

Figure 4-1-9 a) shows the voltage current density characteristics at 140 K and 280 K heat sink temperatures. Contrary to classical quantum well lasers, the quantum cascade laser requires its operational field before it can exhibit gain. With increasing electric field, more carriers contribute to the

inversion, as the upper state lifetime increases with larger energy separation and fewer carriers get directly injected from the ground state into the lower laser level, bypassing the upper laser level. The injection behavior, schematically shown in figure 4-1-9 d) is investigated in detail in subchapter 4-4 (*Voltage Defect & Injection Behavior*). As 4 mm long resonators start lasing with field clamping at 84 kV/cm, which is below the design field of 103 kV/cm and 2 mm long devices require higher current densities, clamping at 90 kV/cm, the field characteristics split up (see figure 4-1-9 b). This results into a non linear 1/L behavior (figure 4-1-9 c), in contrast to typically quantum well and injector based devices. Therefore the 1/L values, which are normally compared, indicate an averaged value for two different resonantors, while the Hakki-Paoli-method enables a direct measurement of the differential gain coefficient. The step size of the current density corresponds to steps of 100 µm in resonator length.

Only longer devices were capable of continuous wave operation at room temperature. Therefore the gain spectra had to be recorded using a 4.1 mm long and 9 µm wide device at an heat sink temperature of 280 K. Due to the longer cavity, the resolution limit was reached for the setup, disabling a direct comparison between the Fabry-Pérot maxima and minima. The recorded spectra had to be deconvolved with the response function of the system as suggested by D. Cassidy [Cas84], and shown to be valid for quantum cascade lasers by Hofstetter [Hof99]. As boundary condition the integral of the measured spectrum and the deconvolved spectrum had to be equal. Figure 4-1-10 shows the gain spectra for various current densities at 140 K (a) and 280 K (b), corresponding to the *VI*-curves (figure 4-1-9a). At 140 K the peak frequency of the gain spectra stays constant, similar to the field of the active region, while a blue shift in peak frequency by 1.4 meV is observed with increasing current densities at 280 K. This shift is contributed to the increasing electric field below threshold which increases from 90.5 kV/cm to 92.7 kV/cm, corresponding to a theoretical change of 1.9 meV in emission energy.

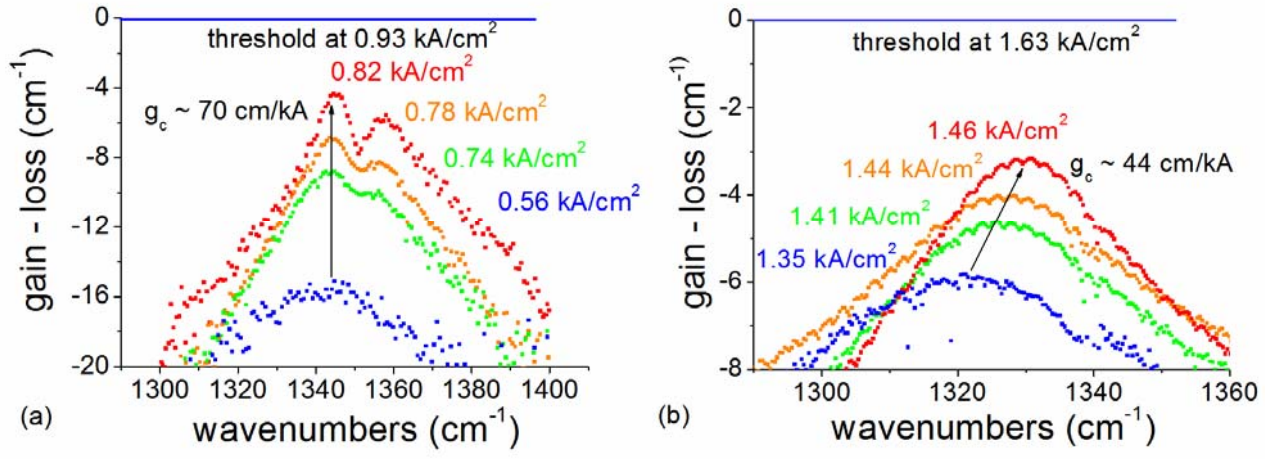

Fig 4-1-10: shows electroluminescence measurement at 140 K (a) and 280 K (b) at different current densities. The differential heating is estimated to be below 12 K (a) and 6 K (b). The black arrow indicates the gain coefficient.

The averaged gain coefficient at 140 K heat sink temperature, for devices of 4 mm and 2 mm in length, yielded 40 cm/kA, while the differential gain coefficient was measured to be 70 cm/kA. The gain coefficient derived from the spectra at 280 K, yielded 44 cm/kA close to threshold, while the 1/L-measurement resulted in 20 cm/kA as averaged value for long resonators. The simulated differential gain coefficient at room temperature, with an FWHM linewidth of 12 meV and an injection efficiency of 80 %, yields a gain coefficient of 53 cm/kA. While the 1/L measurements are performed at low current densities in pulsed operation, the differential gain coefficient was determined at higher current densities in continuous wave operation. Current dependent gain coefficients are also known for injectorbased

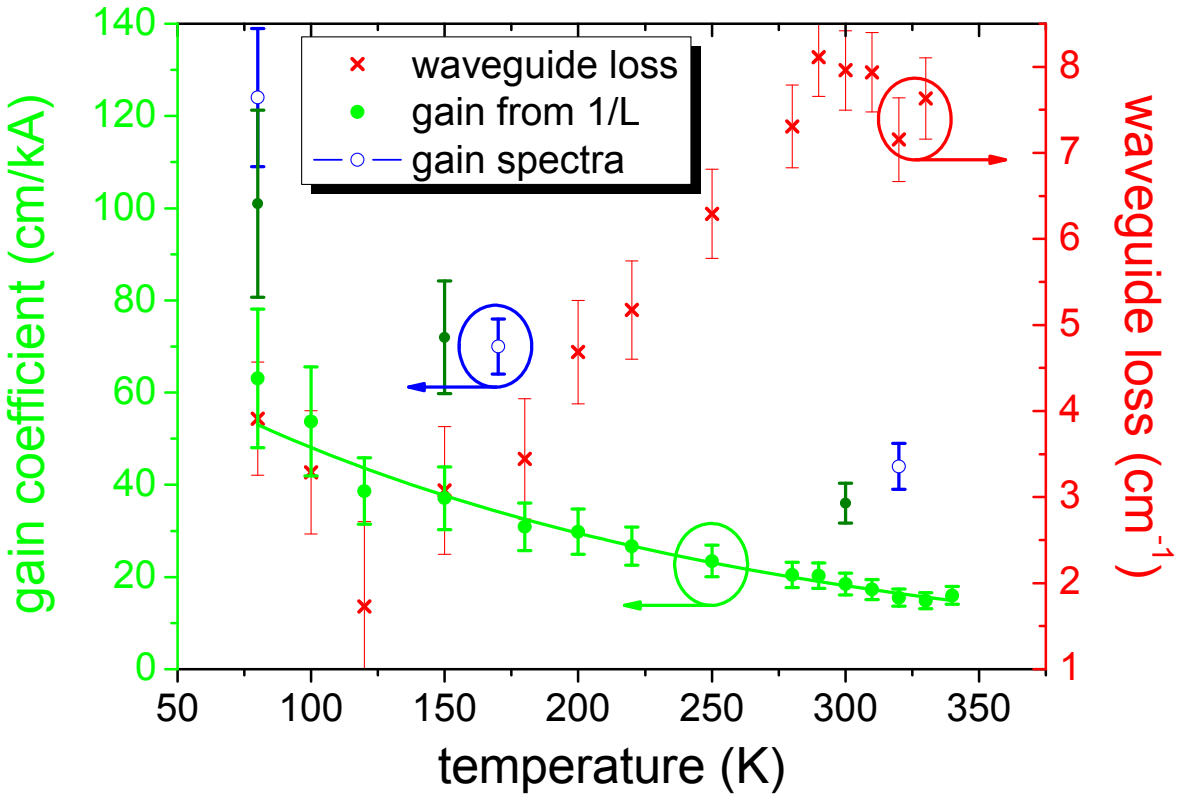

Fig 4-1-11: gain coefficient from the 1/L measurement averaging 4 and 2 mm devices (green, filled circles) and 2 and 1 mm devices (dark green, filled circles), corresponding waveguide losses (red,cross) and the differential gain coefficient extracted from the electroluminescences measurements (blue, open circles)

devices [Ben09], but are normally not that strongly emphasized as in injectorless devices. The nonlinear gain coefficient is contributed to the operation below design field for long resonators and higher required current densities for shorter resonators, which increase the applied fields accordingly. Therefore the 1/L measurement for shorter resonantors gives values closer to the ones measured with the Hakki-Paoli-method.

Figure 4-1-11 shows the summarized results from the gain coefficient measurements. A general error source is the inhomogeneous etching behavior, resulting in not perfectly known mesa widths, scattering the measured threshold current densities by roughly 10 %. The 1/L measurement has an increasing error towards the low temperatures due to measurement offsets and the very small threshold current densities, with small differences giving large differences in waveguide losses and gain coefficient. Also leakage paths are increasing with temperature, increasing the discrepancy between 1/L-method and Hakki-Paoli-method accordingly.

The waveguide losses follow the inverse mobility, as expected, over the temperature range. This shows that plasma absorption is contributing a dominant share of the waveguide losses, besides the intersubband absorption and the waveguide roughness [Too08]. In comparison to injectorbased devices, the average gain coefficient of injectorless devices is at least a factor of two larger, when taking 1/L-measurements into account. Long wavelength emitting injectorbased quantum cascade lasers show a maximum average gain coefficient of 10 cm/kA [Ben09][Wit09], while short wavelength emitting devices show an even lower gain coefficient of roughly 6 [Lya08] to 4 cm/kA [Gre09] at room temperature. The higher gain coefficient leads to the record low threshold current densities [Kat08][Boe09], although the waveguide losses are still high and give room for further improvement.

4.2 Continuous wave devices

Besides optimizing the pulsed operation characteristics of the devices as it was done previously, continuous wave (*cw)* operation was another goal of this work. For achieving a good cw performance, the device requires not only good electrical and optical characteristics but also a thermal design as best as possible. From equation 2.3.5 one can derive the maximum thermal resistance suitable for continuous wave room temperature operation for a given design and its pulsed characteristics.

4.2.1 Double-trench process of two alloy reference sample

As first design, the reference design using two material compositions, was chosen for the continuous wave process, as back then, no better design was at hand. The low doped, 60 stages containing sample (for the design see figure 4-1-1) exhibits a characteristic temperature of 103 K (see figure 4-2-1), a threshold current density of 0.10 kA/cm^2 at 0 K and a threshold voltage of 16.5 V. The processed samples had an effective width of roughly 8 µm and a resonator length of 4.1 mm. This yields a maximum thermal resistance of 3.9 K/W for reaching 300 K in cw operation, an unrealistic low value.

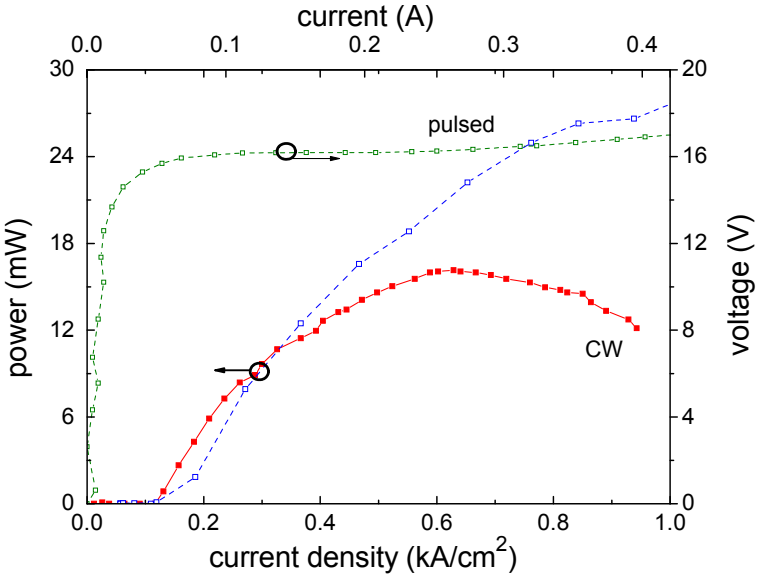

Fig 4-2-1: pulsed (blue & green) and continuous wave (red) performance for the two alloy sample. The maximum temperature of operation was 140 K due to the high thermal resistance of 18 K/W.

The maximum temperature of cw operation which had been observed was 140 K. This indicates, following equation 2.3.5, a thermal resistance of 20 K/W. This value is about a factor of two higher than comparable devices of other research groups. As the thermal simulation (see chapter 2-7) gives 9.2 K/W, the main difference was found in the simple setup technology (see chapter 3.3.1), which was used for pulsed operations and also applied here.

The continuous wave performance was mostly limited by the high thermal resistance, resulting in a low threshold current density of 0.13 kA/cm^2 at 80 K. The peak optical power was estimated with 16 mW, using an MCT as no calibrated power measurement system was available back then. It is most likely higher by a factor of 10 at least. Another method of extracting the thermal resistance, as shown in chapter 3.4.2, is the comparison of pulsed and continuous

wave threshold current densities. This method yielded a thermal resistance of 20-24 K/W, much too high for room temperature operation.

4.2.2 p-doped InP overgrowths

For further improving the thermal management some tests with p-doped InP overgrowth were performed, as no iron source was available at the inhouse metal-organic chemical vapor deposition system (*MOCVD*). Figure 4-2-2 shows the performance of a sample in overgrown and simple metal-cladded ridge waveguide process, including a small side picture of a cleaved facet. While the standard processed voltage current characteristics change with temperature, the overgrown devices don't change that drastically but show good blocking behavior and similar serial resistances, which indicates in general a good overgrowth. When comparing the pulsed optical powers, it can be shown that the

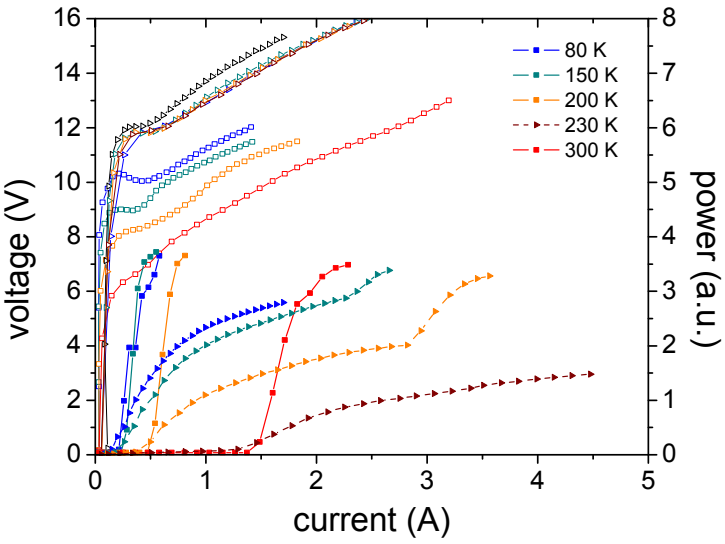

Fig 4-2-2: standard process (square) and 6 µm overgrowth (triangle) compared in voltage (open) and power (solid) for different temperatures. The small image below shows a cleaved facet at the edge of the processed wafer (with an increased etch depth due to wafer edge).

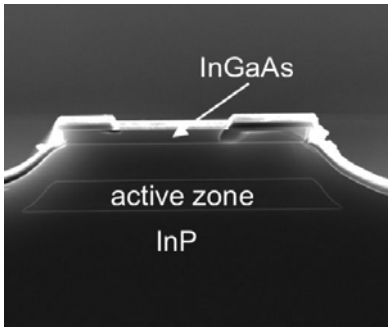

thresholds at low temperatures are closer than towards higher temperatures. In addition with the much smaller slope it is assumed to be limited by inter-valence band absorption due to the positive doped InP. With the complexity of the problem and the knowledge that most other groups use iron doped semi-insulating InP for overgrowth, other approaches on improving the continuous wave performance were considered.

4.2.3 Simple ridge process of optimized four alloy sample

With the implementation of four alloys and the corresponding improvements in pulsed operation, regarding all critical parameters, the chances of better continuous wave operation were increased. The medium doped, 60 stages containing sample (for the design see figure 4-1-2) exhibits a characteristic temperature of 153 K, a threshold current density of 0.18 kA/cm^2 at 0 K and a threshold voltage of 13.6 V. Additionally the process was modified from only wet etching to a combined etch process as described in chapter 3.2.3. Therefore the processed samples had an effective width of only 4 µm but also

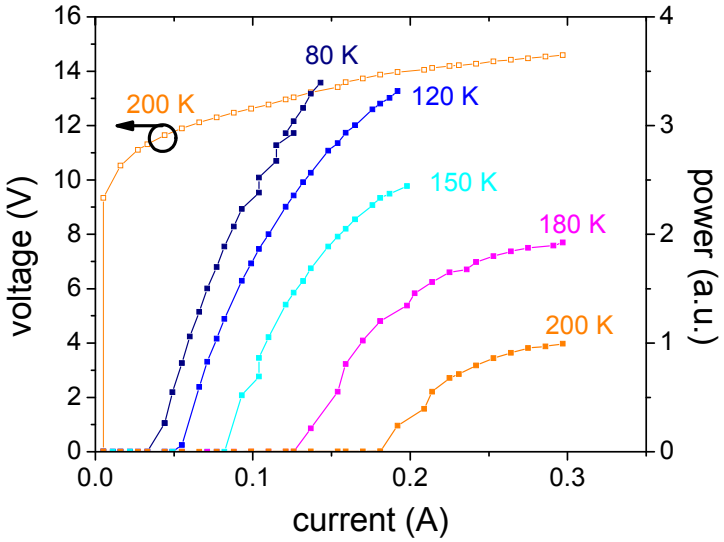

Fig 4-2-3: continuous wave performance of 4 µm wide and 4.1 mm long device using the design presented in figure 4-1-2 and the combined etch process as described in chapter 3-2-3. The maximum temperature of operation was 200 K, due to the very high thermal resistance of 40 K/W. An additional VI-curve at 200 K is shown.

a strong underetch (figure 3-2-4, right). This yields a maximum thermal resistance of 20 K/W for reaching 300 K in cw operation, a value which had been achieved before. Unfortunately the thermal resistance of the devices in epi-side up mounting had strongly increased up to 40 K/W, theoretically limiting the device performance to 190 K. Figure 4-2-3 shows the cw performance of such a device measured inside the cryostat.

The maximum optical power at 80 K was only reaching 340 mW at 450 mA, while the wall-plug efficiency reached its maximum of 5.5 % at a current of 200 mA already. The drop of conversion efficiency above 200 mA (1.2 kA/cm^2) is a result of the high thermal resistance. For further improvement the newly developed cw process had to be optimized but also the setup technology had to be improved.

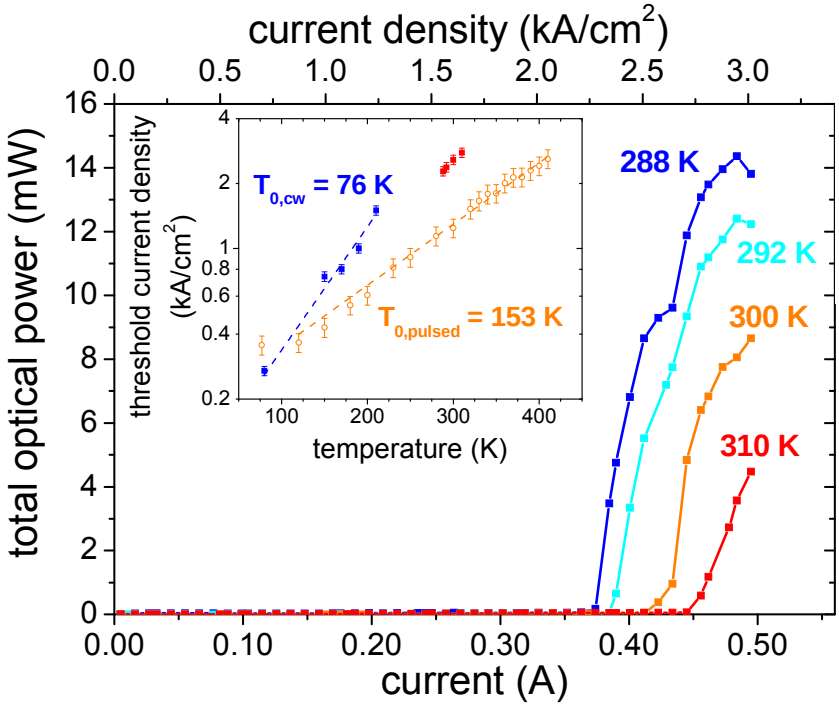

Fig 4-2-4: room temperature continuous wave operation. From the difference in thresholds (inset) the thermal resistance at 300 K of 17 K/W can be extracted. Below the emission wavelength at room temperature is shown.

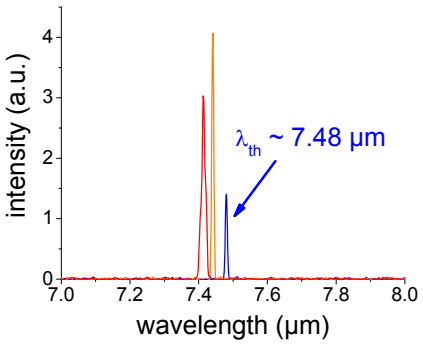

The continuous wave setup technology was changed towards professional mounting, as described in chapter 3.3.2. Additionally the devices were setup epi-side down, directly connecting the mesa to the heat pad. Although the thermal resistance of the new process was far from being optimized, room temperature cw operation was achieved [Kat09b]. Figure 4-2-4 shows the results for various temperatures, including a small inset which shows the characteristic temperature for pulsed and continuous wave measurements. While the pulsed threshold current density at 300 K is as low as 1.2 kA/cm^2, in cw operation it shifts up to 2.6 kA/cm^2 which is equal to the pulsed threshold current density at 410 K. From this shift and the threshold power of 6.4 W, we can extract a thermal resistance of 17 K/W. When using the pulsed performance and equation 2.3.5 on the maximum temperature of cw operation, it also yields 17 K/W.

4.2.4 Broad Double Channel Process of Four Alloy Sample

For further reducing the thermal resistance, a less underetched process with additional heat pads was considered. To avoid an increasing pulsed threshold density due to ultra narrow mesas and side wall roughness, the mesas were designed to be 9 to 13 µm in width. This leads to an increase in threshold power of roughly a factor 2.5, which had to be compensated by the decreasing thermal resistance. A cleaved facet from the wafer edge is shown in figure 4-2-5, indicating the additional heat pads at the edges of the picture. The cleaving areas are left free of galvanized gold and the shown mesa corresponds to a width of 9 µm. Due to the wet etching process which is unfortunately geometry dependent, this mesa is about 11 µm wide in the mid of the sample. This rather large deviation in mesa widths towards the edge leads to some uncertainties (~ 10 %) in current density measurements. As explained in the gain spectra measurement section (see subchapter 4.1.3), this error can lead to quite large errors in the gain coefficient determination, especially at low temperatures.

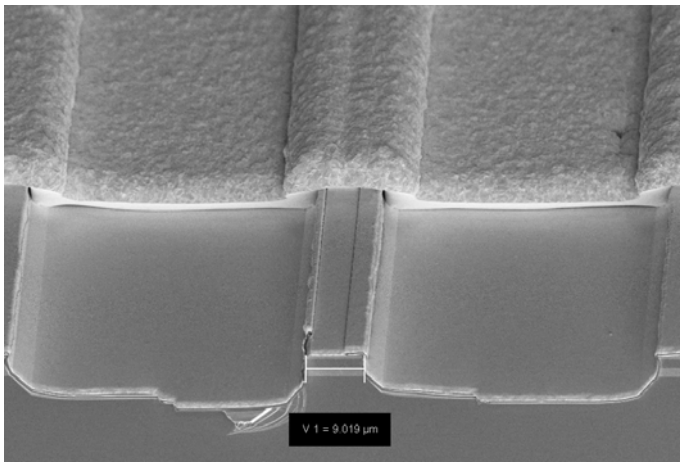

Fig 4-2-5: Fib picture of broad mesa process. The small white bar indicates the measured mesa width equaling 9 µm.

The device being processed was similar in design and growth than the previously mentioned simple ridge process, which lead to the first continuous wave, room temperature operation of an injectorless quantum cascade laser. Figure 4-2-6 shows the *LIV*-performance of a 4.1 mm long and 9 µm wide sample, placed on a Peltier cooler. The thermal resistance was measured to be 10 K/W, a 60 % improvement in comparison to the simple ridge process, using the same setup technology.

the continuous wave threshold was measured to 1.76 kA/cm^2, while the pulsed room temperature threshold of 1.1 kA/cm^2 was close to the narrow mesas value of 1.2 kA/cm^2. The much lower shift between those two values is attributed to a more robust process, although the threshold power has shifted from 6.4 W up to 11 W at 298 K. These high powers, in comparison to normal quantum well laser diodes which require *CW* threshold power arround 100 mW [Kas09], come together with higher internal thermal resistances, due to the thick superlattice structures of ternary materials. Therefore reaching room temperature continuous wave operation with quantum cascade lasers is much more challenging than with regular laser diodes. Figure 4-2-7 shows the maximum temperature

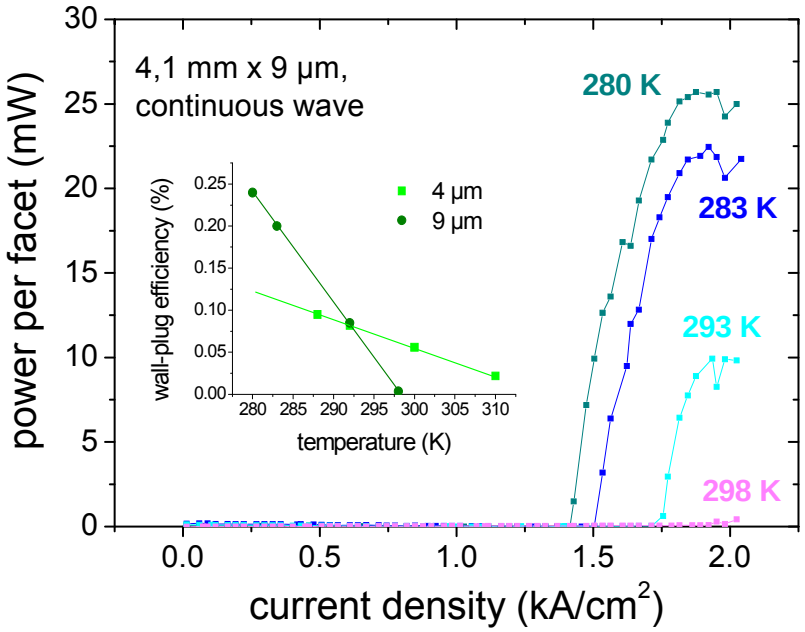

Fig 4-2-6: output power for a single facet (uncorrected) for broad double channel device (left). The inlet shows the overall efficiency in comparison to the narrow simple right process. The maximum temperature versus the thermal resistance is shown below with the first cw process (red), the narrow ridge (green) and the broad (dark green)

of operation in dependence of the thermal resistance, as described by equation 2.3.5 in the thermal properties and design chapter. A quantum well laser diode would already operate above 500 K, when taking the values from Kashani et al. [Kas09]. The difference in the characteristic temperature becomes more critical the lower the thermal resistance is. The red curve corresponds to the first, two alloy continuous wave device, which has a characteristic temperature of 103 K. The green curves show the narrow simple ridge (light green) and the broad double channel process (dark green), which both had a characteristic temperature arround 150 K.

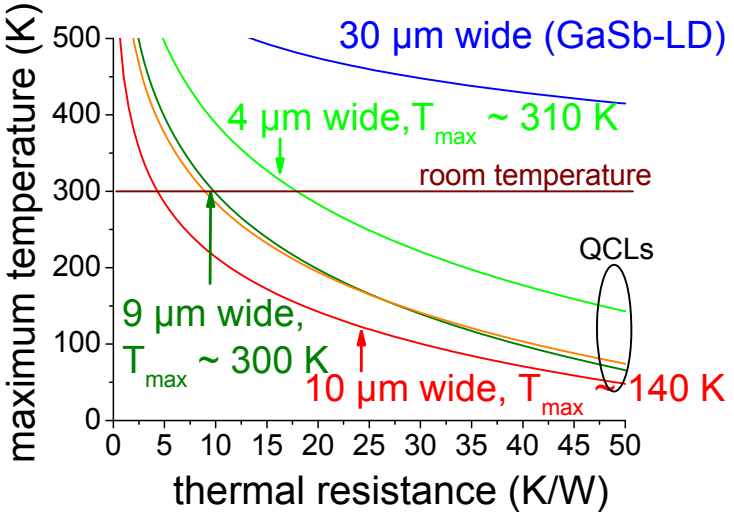

Fig 4-2-7: The maximum temperature versus the thermal resistance is shown below for the first cw process (red), the narrow ridge (green) and the broad double channel process (dark green).

4.3 High performance devices

Devices with good threshold current densities, which are directly proportional to loss management and gain, could be expected to exhibit also good performance regarding output power and efficiency. When taking a closer look into the details of the device, it can be shown why this doesn't necessarily correlate. The gain coefficient (see equation 2.1.7) can be large either due to a high dipole matrix element or a very high upper state lifetime. The slope efficiency (see equation 2.2.19), determining the efficiency above threshold, only depends on the upper state lifetime and the losses. When finally looking at the overall efficiency (see equation 2.2.20), the maximum driving current, ignoring heating, also plays a role. Besides these criteria's, the energy of the transition goes into the performance, enabling higher wall-plug efficiencies at lower wavelengths [Fai07].

4.3.1 Optimization of performance by emission wavelength and upper state lifetime

For improving the device performance in terms of slope and wall-plug efficiency, the transitions were further diagonalized to increase the upper state lifetime while reducing the dipole matrix element

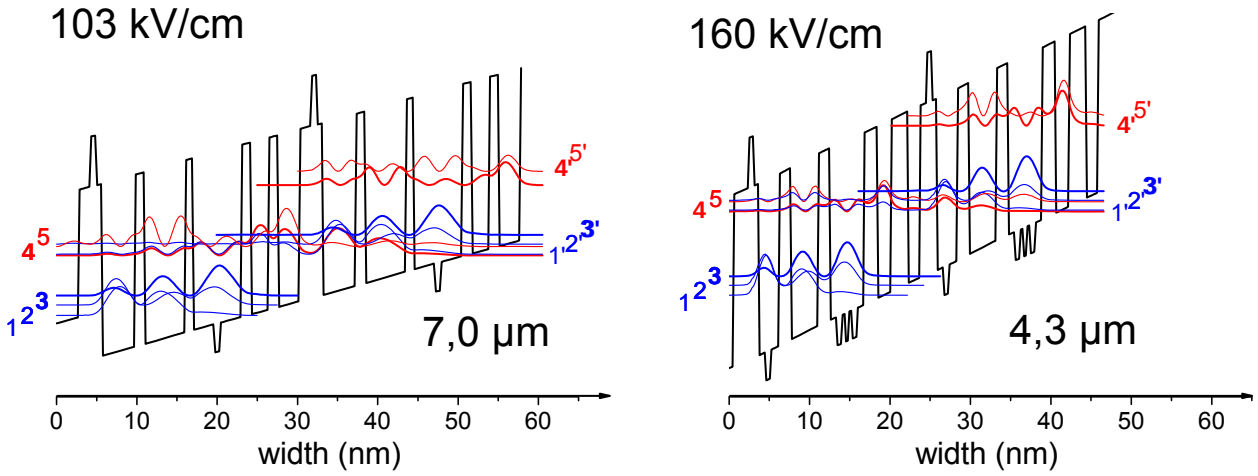

Fig 4-3-1: active region of four alloy injectorless device (left) and advanced design (right) using three InAs spikes (right). The layer sequences are **1.45**/***0.5***/**0.56**/4.03/**1.1**/5.0/**0.9**/2.6/*0.51*/2.6/**1.0**/2.1/**1.0**/2.66 for the left design and **0.8**/***0.65***/**0.7**/0.95/*0.58*/1.1/**1.8**/3.8/**1.5**/0.8/*0.51*/0.47/*0.45*/0.42/*0.6*/0.87/**1.8**/1.8/**2.3**/1.4 for the right design (both in nm). The four material compositions are indicated as: ***AlAs in bold and italic***, **$Al_{0.635}In_{0.365}As$ in bold**, $Ga_{0.4}In_{0.6}As$ in regular and *InAs in italic style*. The silicon doped layers are indicated by an underline.

of the transition. Figure 4-3-1 shows a reference design, using a single InAs spike (left) and an improved design with four InAs spikes (right) to increase the upper state lifetime by its low effective in-plane mass. Additionally the emission energy was increased by 63 % compared to the reference, which results into a roughly 60 % increase in field. Injectorless devices have to regain the transition energy within one sequence as regular quantum cascade lasers do, but they cannot use multiple wells for this and therefore show a direct transition energy dependence of the required field. This point will be also discussed in the

conclusion section (see figure 5-1). For the device growth the stages were reduced from 60 to 52 as a shorter wavelength requires fewer stages for an equal confinement factor.

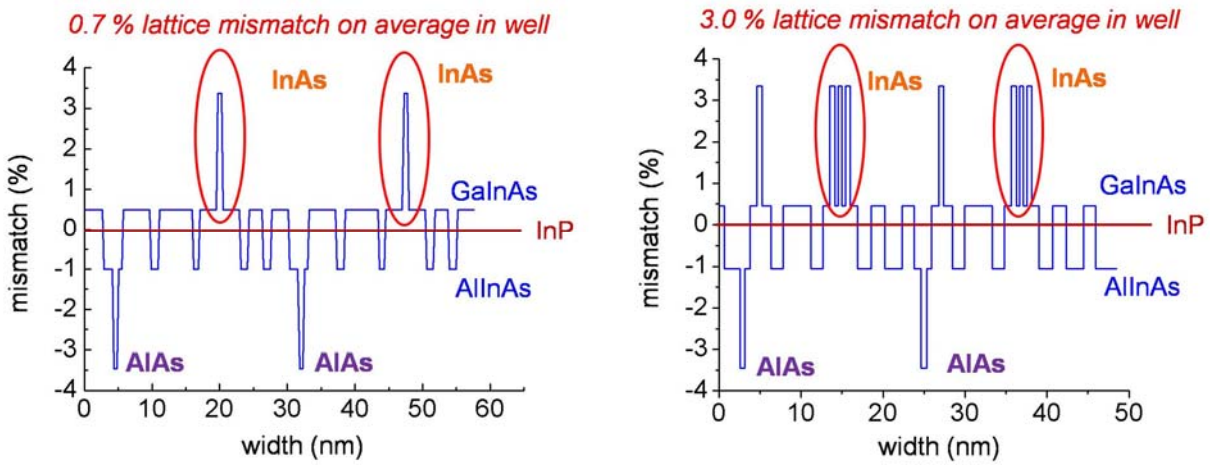

Fig 4-3-2: lattice mismatch of the single (left) and the four (right) InAs-spike design presented in figure 4-3-1.

At this point we also have to consider the lattice mismatch of the structure, as discussed in subchapter 2.2.2, because it can be a limitation. Figure 4-3-2 shows the strain over two stages for both designs presented in figure 4-3-1. Both designs are strain compensated over the whole period, but the strain accumulation inside the optically active well is completely different and by a factor of 4 higher.

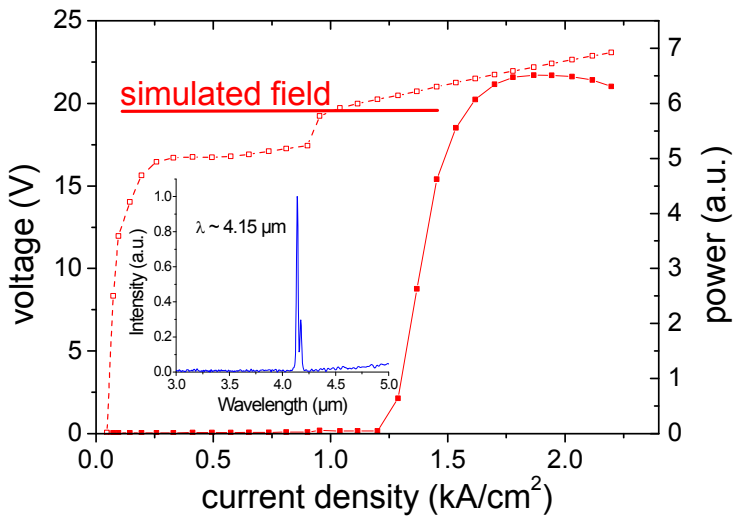

Fig 4-3-3: pulsed performance at 300 K of the four InAs-spike containing design. The inset shows the spectrum at low temperatures, which didn't shift towards higher temperatures as the emission energy was clamped.

It has to be stated that this design is a quite large step forward as nearly everything was greatly altered from field, emission wavelength and strain. Although the simulation indicated an increase of 10 % in gain coefficient, the additional losses into the continuum or side valley due to the high field were unknown.

The first growths failed due to the accumulation of strain although the first few periods could be grown without relaxation. Therefore the growth temperature was reduced further, finally ending with 50°C less. Figure 4-3-3 shows the performance of a device with 52 stages and a sheet

doping density of $5 \cdot 10^{10}$ cm^{-2}. The emission wavelength is the shortest ever reported for an injectorless device, but the power was very weak and nearly all devices tended to fail after some time. This was attributed to the lower optical quality and the higher defect ratio induced by the drastically reduced growth temperature. Another loss mechanism could be the scattering into side valleys or the loss into the continuum, clamped the field over all temperatures beneath the design field up to a current density of 1.0 kA/cm^2, also clamping the threshold to 1.0 kA/cm^2 below 280 K, yielding an artificial infinite characteristic temperature. This field clamping was already observed with a different design, using only AlAs enhanced barriers and comparably low strained wells [Kat07], but back then attributed to leakage states. The design fields were both 160 kV/cm and in both cases the field jumped around 1.0 kA/cm^2 to the designed field. In 2007 the thresholds were higher and the infinite characteristic temperature was not recognized. A possible reason could be material dependence, as the leakage into side valleys gets saturated, allowing finally the field to increase further. With this in mind, the next designs were optimized for fields below the first saturation field strength of 130 kV/cm.

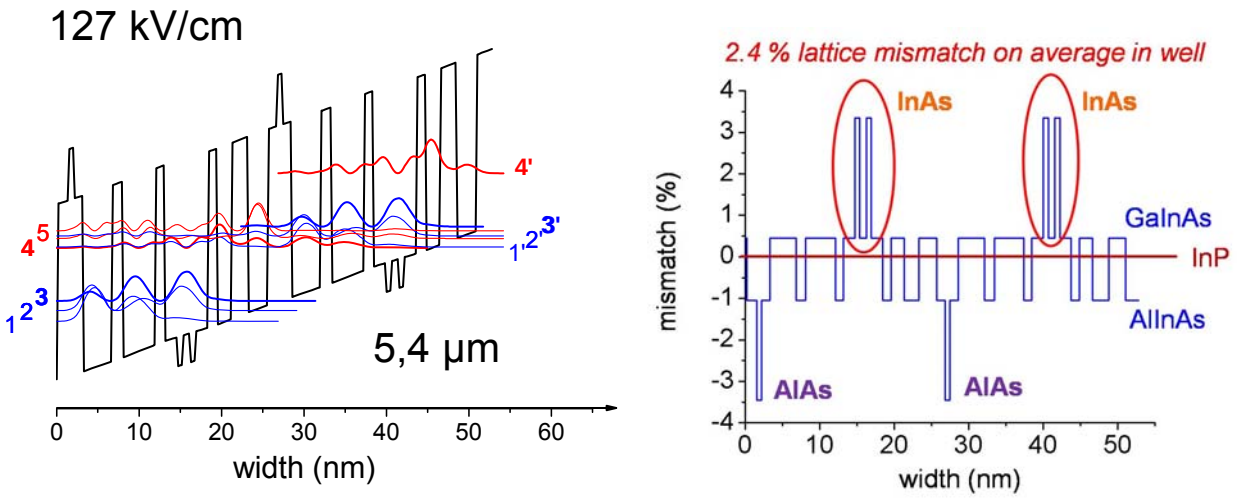

Fig 4-3-4: active region of a moderately modified device (left) with a field below the critical field strength. The layer sequence is **1.0**/***0.65***/**1.0** /3.5/**1.3**/4.4/**1.2**/1.3/*0.6*/0.8/*0.6*/1.3/**1.0**/1.95/**2.2**/2.5 with ***AlAs in bold and italic***, **$Al_{0.635}In_{0.365}As$ in bold**, $Ga_{0.4}In_{0.6}As$ in regular and *InAs in italic style*. The silicon doped layers are indicated by an underline. The right side shows the lattice mismatch over two periods with a accumulated lattice mismatch of 2.4 % in the transition well.

This moderately modified design (see figure 4-3-4) was using a design field of 127 kV/cm, an emission energy of 5.4 µm and an accumulated mismatch of 2.4 % in the transition well. From the depletion and injection scheme, the design was similar to all previous designs, using two phonons for depletion and a coupling strength of 4 meV between the ground state and the upper laser state. It was grown at a regular temperature containing 55 stages and using, for comparability, an equal doping in the active region of $5 \cdot 10^{10}$ cm^{-2} as sheet doping density (medium doping level).

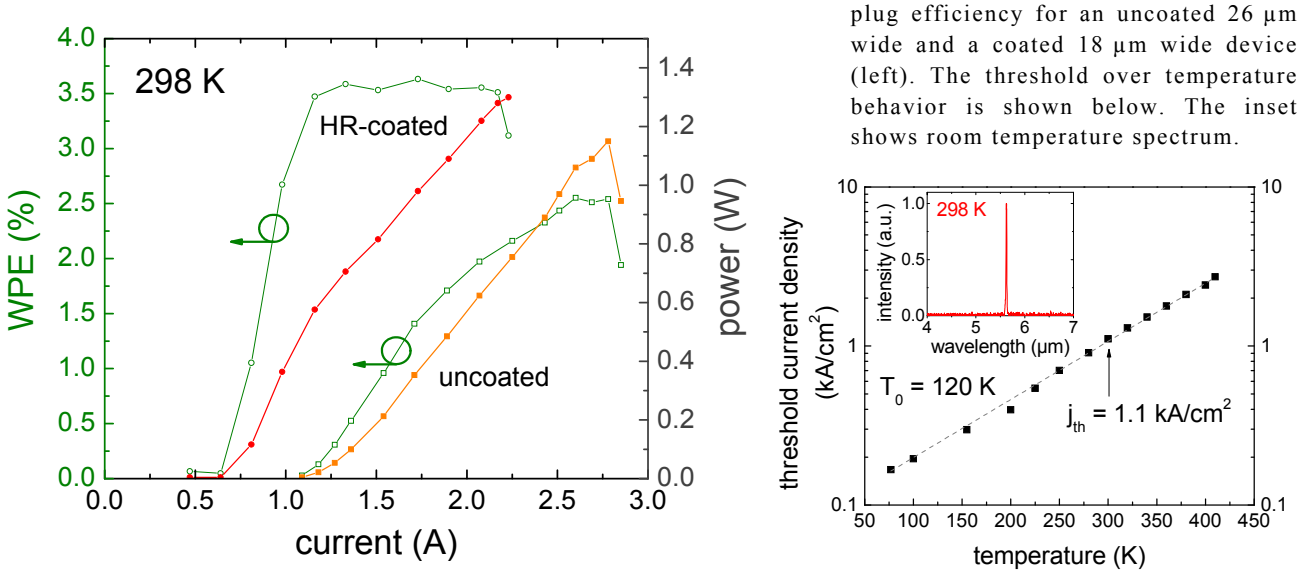

Fig 4-3-5: performance of the design shown in figure 4-3-4. Output power and wall plug efficiency for an uncoated 26 µm wide and a coated 18 µm wide device (left). The threshold over temperature behavior is shown below. The inset shows room temperature spectrum.

The performance of this design is shown in figure 4-3-5. Due to the high fields and the additional losses into side valleys and continuum, the threshold current density didn't improve, but reached an acceptable 1.1 kA/cm^2 at 300 K. These additional losses are temperature dependent, which can be seen in the reduced characteristic temperature of 120 K.

When looking at the output power and efficiency performance, the original aim of the device, it was strongly improved. While the two alloy reference sample only emitted 240 mW with 0.83 % efficiency and the simple four alloy sample already reached 420 mW with 1.3 % efficiency, the new design was capable of 1200 mW with 2.5 % efficiency. Comparing the slope efficiencies for medium doped samples, the two alloys reference (see figure 4-1-1) reached 270 mW/A, the simple four alloy sample (see figure 4-1-2) showed 400 mW/A, while the moderately modified design reached 800 mW/A with less stages. This is an improvement of a factor 2 for slope and overall efficiency, which cannot only be contributed to the emission energy increase of 30 %, as even the number of stages was reduced by 9 %, from 60 to 55. When adding a high reflective back facet coating the overall efficiency increased to 3.6 % [Kat09], without taking collection efficiency into account.

4.3.2 Beam propagation and power collection efficiency

At this point, it has to be mentioned, that all power and efficiency values which have been reported are not corrected for any collection efficiency. In reality, the processed devices have relatively wide mesas but thin core thicknesses. This causes the beam to diverge with different angles into different directions and it is general unknown how many transversal modes are lasing under which angle distribution the energy is diverging. While the beam propagation can be described with the Gaussian distribution in the ideal case for the fundamental mode TM_{00}, it can be much more complicated for multimode lasers. Retaining on the Gaussian description as much as possible, real devices are

characterized by their beam quality factor M^2, which is 1 for ideal Gaussian beams but can reach values of 10 for high-energy multimode lasers. Figure 4-3-6 shows the propagation for an ellipsoid beam waist in the fundamental mode.

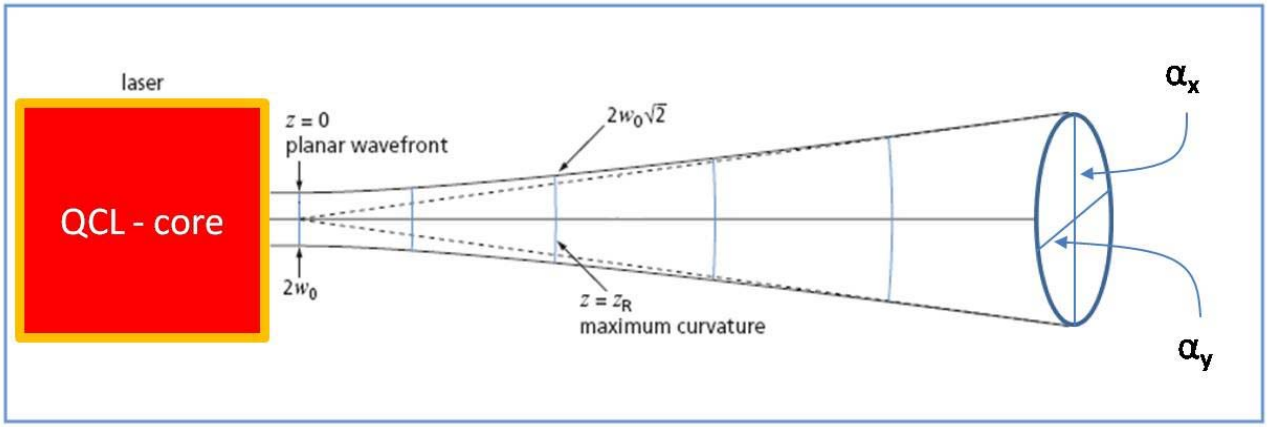

Fig 4-3-6: Schematics of Gaussian beam propagation for the fundamental mode TM_{00}.

For describing the propagation properly, it has to be determined if the near-field or the far-field description is required. At a distance ten times larger than the Rayleigh length z_r, which is written as [Mel02]:

$$z_r = \frac{\pi \cdot (w_0 M)^2}{M^2 \lambda} \tag{4.3.1}$$

with w_0 as the beam waist at the facet, the far-field description is suitable. For a quantum cascade laser, with an emission wavelength of 7 µm and mesa widths up to 30 µm, the Rayleigh length yields 0.4 mm. A simple description of the far-field behavior is the beam waist $w(z)$ in dependence of the propagation distance z, given by [Mel02]:

$$w(z) = w_0 M \cdot \sqrt{1 + \left(\frac{z \cdot \lambda}{\pi {w_0}^2}\right)^2} \tag{4.3.2}.$$

It is noteworthy that the Rayleigh length is independent of the beam quality factor M, which only changes the beam waste and the divergence angle as constant factor.

Our power measurements are carried out with a thermopile detector, which has an aperture of 12 mm and the minimum distance between the laser and the detection area is 7.5 mm.

During a demonstration of a far-field CCD camera for the near, mid and far infrared range, it was possible to measure a few far-field patterns at different distances. Figure 4-3-7 shows the three dimensional far-field pattern taken at a distance of 6 mm at high currents for a typical mid infrared device of 4 mm in length and 26 µm in width. The active core was thicker than in previously mentioned samples with 1.91 µm.

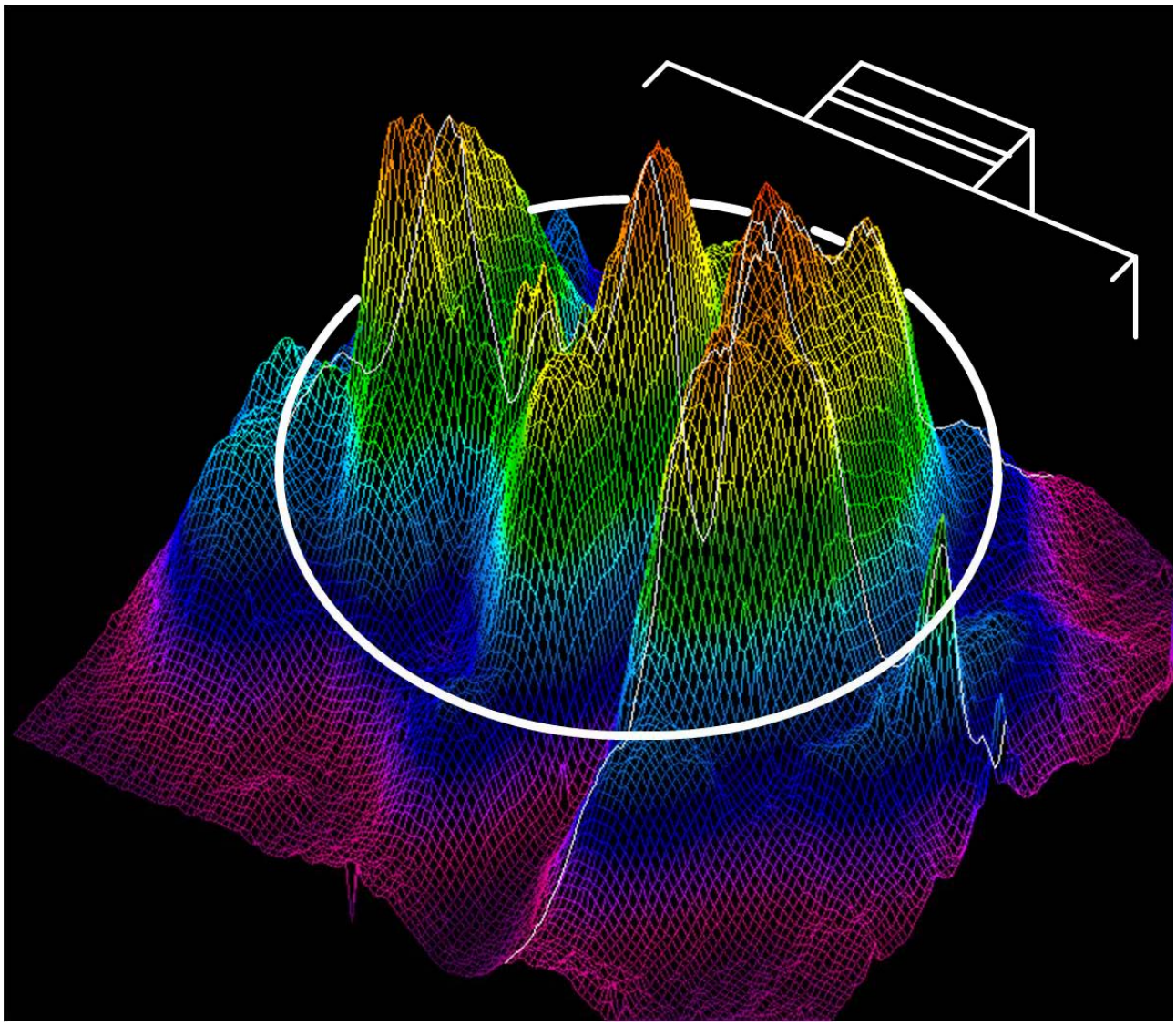

Fig 4-3-7: Far-field pattern of an injectorless mid infrared quantum cascade laser at high currents. The intensity is shown by coloring. The white ring shows the thermopile aperture as explained in the text and a small white chart indicates the layout of the mesa.

From the far-field measurement, it is clear that the divergence of the device is much more complex. The output intensity is containing higher order modes in one transversal direction, like strong a TM_{01}-mode, while the thin active region prevents higher order modes in the other transversal direction. According to *Rsoft* simulations, the TM_{00} mode should have a divergence angle (*FWHM*) of 55.6° on the growth axis and 19.7° on the in-plane axis, while the TM_{01}-mode should have a divergence of 44° between its peak positions. Using an aperture comparison between the farfield patterns at 6 mm and 7 mm distance, the divergence of the fundamental mode was estimated to 57.3° and 25.2°, respectively. Although the fundamental mode is behaving nearly Gaussian, the power is carried also in higher order modes, which have a larger divergence. The TM_{01}-mode has a measured divergence of 46° on between its peak positions, and a measured *FWHM* of 60° in the growth axis, yielding an *M*-factor of roughly 3.

For experimental determination of the collection efficiency of the power measurements, the 12 mm aperture of the thermopile detector at 7.5 mm distance was projected (white ring) into the far-field pattern at 6 mm. The collection efficiency was then derived by the quotient of the integrals over the intensity inside the projected ring and over the whole area. In good agreement with other reported efficiencies [Wan09], a value of 69 % was calculated. This method neglects the fact, that already at a distance of 6 mm, some power was missing the 12.4 mm long quadratic detection field of the camera. This effect can be seen at the sides where the intensity doesn't reach the noise level. For avoiding background noise, the system was calibrated to a zero line, with positive and negative noise, which drops out when integrating.

When taking the collection efficiency into account now, the previously measured optical powers and overall efficiencies have to be increased by a factor of 1.45, yielding a maximum power of 1.9 W from a single facet and an overall efficiency of 5.2 %. For the next chapters, the collection efficiency is further assumed to be 100 % and only at the end, when comparing with devices from other groups, it is taken into account as done by others.

4.4 Voltage defect and injection behavior

When optimizing the designs only by phonon depletion and dipole matrix element, the injection behavior is neglected although it plays a crucial role. Unfortunately this injection behavior cannot be covered by one-dimensional approaches as the in-plane momentum and thermal distribution play a major role at these low energetic processes. Lately, research in classical injector-based devices has turned towards theoretical [Khu09] and experimental [Esc09] investigations of the injection behavior. A line broadening or dephasing is caused by intra-subband and intersubband scattering processes [Wit08]. These scattering processes can prevent carriers from tunneling from the ground state of the previous stage into the subsequent upper laser state effectively, resulting in a very long lifetime in the ground state. Another uncertainty is the unclear role of phonons in combination with thermal distributions and different coupling strengths.

4.4.1 Voltage defect and electric field

At 80 K most designs show ideal *VI*-curves with a very low serial resistance and lasing at the design field. At room temperature, the wavelength has shifted as predicted by the simulation, but the voltage characteristics might have changed more drastically, indicating a different resonance scheme at higher temperatures. A sample containing only a full waveguide with all claddings but no active region was grown for evaluating the electric field at the active region.

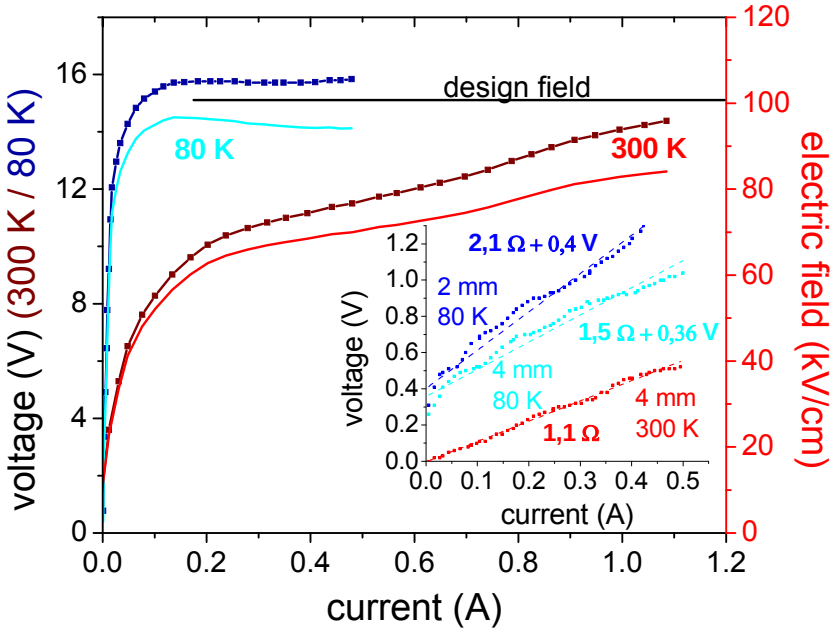

Fig 4-4-1: voltage-current (with squares) and electric field-current (without squares) characteristics for the 4-alloy reference sample (design, see figure 4-3-1, left). The small inlet shows the waveguide and setup only measurement, which was used for deriving the real electric fields.

Figure 4-4-1 shows the voltage over current curves at 80 K and 300 K and the corresponding electric fields. The design field and the measured electric field are only 5 % off at low temperatures, which is within the growth variations. At higher temperatures, lasing starts already at much lower fields, in this case 30 % below the design field. From these measurements, the voltage defect, which is defined as the energy per period, which is used for the depletion and injection of the carriers, can be estimated. By extracting the corresponding energy per period from the measured field and subtracting the emission

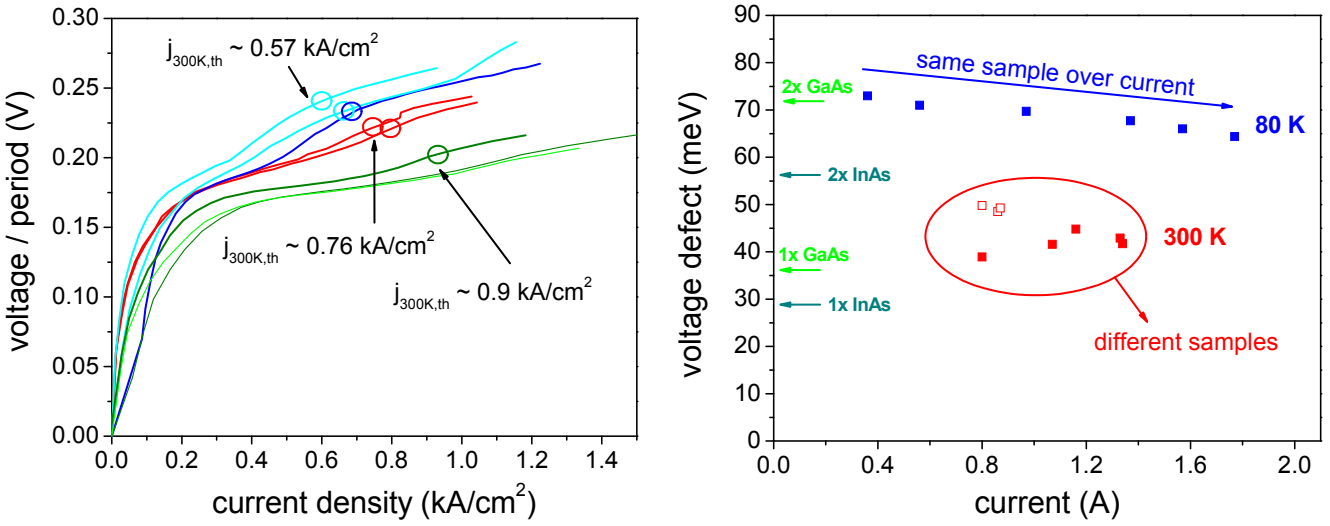

Fig 4-4-2: multiple voltages versus current characteristics (left) normalized per period for samples of different active region doping levels and number of stages but similar size (300 K). The blue lines are low doped samples, the red ones indicate medium doping and the green lines are medium doped but strongly shifted due to unknown growth issues. The right side shows the voltage defect for these curves at 300 K (red, open for low doped, full for medium doped), but also a variation over current for a low doped sample. Small marks indicate the energy of the *LO*-phonon modes.

energy from the corresponding spectra, the voltage defect energy is determined. Nearly all injector-based quantum cascade lasers have a large voltage defect, in the range of 100 to 140 meV at room temperature, except for some specially low-voltage defect designs [Hof07], which reach down to 70 meV. This voltage defect energy is unwanted, as it doesn't contribute to the emission and only heats up the device, and therefore should be reduced as much as possible. Injectorless devices on the other side exhibit a voltage defect around 40 to 50 meV, but can reach even lower values.

During this work multiple *MBE* growths of the 4-alloy reference design have been performed for testing the actual growth quality or optimizing the number of stages and doping levels. In figure 4-4-2 the voltage per period (left) of these samples is shown together with the evaluated voltage defect (right). While the difference in voltage per period can be as large as 50 meV, the voltage defect is varying in the range less than 10 meV. In other ways described, the change in voltage per period is mainly a change in the emission wavelength with similar resonance scheme for depletion and injection.

The 4-alloy reference design is meant to use two optical phonons for depletion and interface roughness-defect scattering between the energetic closer states for injection. While this scheme can be applied at low temperatures, with a voltage defect in the range of two GaAs *LO*-phonon modes, it does not match at higher temperatures.

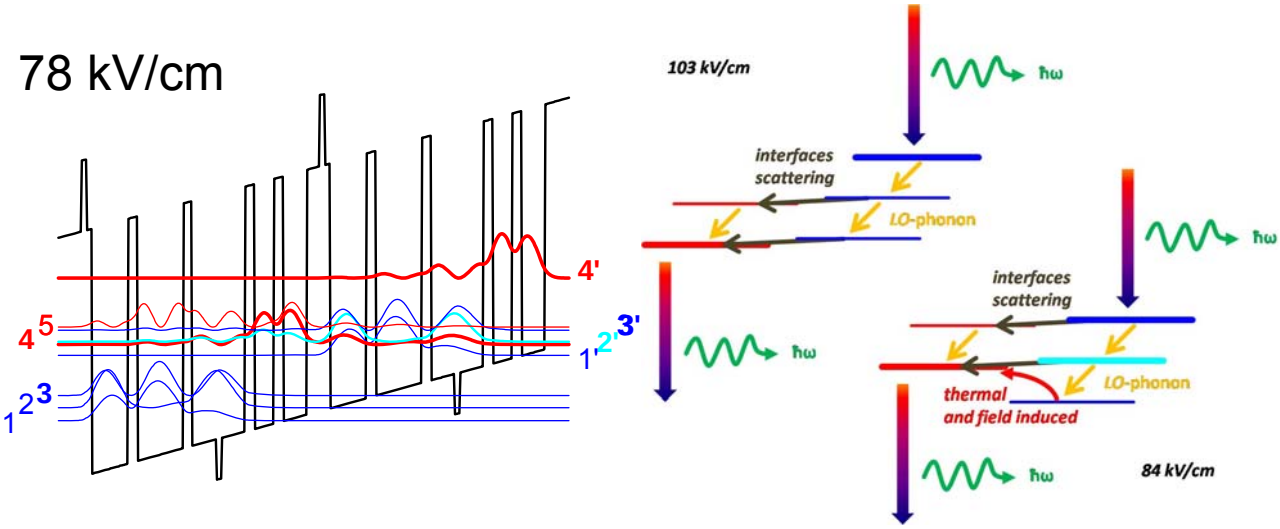

Fig 4-4-3: active region of the 4-alloy reference design at the estimated field at room temperature (left) and the resonance depletion and injection scheme (right) for the low temperature and design case (103 kV/cm) and the room temperature case (84 kV/cm)

With the evaluated electric field at room temperature, the band structure changes as shown in figure 4-4-3 in contrast to figure 4-3-1 (left). For emphasizing this effect the right side of figure 4-4-3 shows the more simplified depletion and injection scheme. At low temperatures, the electric field raises until the two depletion states (1 and 2) are in resonance with the optical phonon energy. At this point the scheme looks like the 103 kV/cm case. With increasing temperature, carriers exhibit more energy which enables a resonant scattering at an energetically lower separation, similar to the far infrared emission designs (see figure 2-1-3). This is shown in the right scheme (84 kV/cm), with an injection between state 2' and 4. Carriers which are scattered down to the ground state are easily excited by thermal energy and scattered into state 4 or 2' due to the high fields. This strong current path prevents the device from reaching its design field, but it doesn't disable a sufficient population inversion and therefore lasing. Shorter devices with higher losses require larger gain, which is achieved by higher current densities and increasing electric field, as shown in subchapter 4.1.3 in figure 4-1-9b. This behavior cannot be simulated with the simple one-dimensional approach, as the in-plane dispersion relation becomes important.

The effect of the high field in combination with the thermal excitation becomes more obvious, when comparing with another sample (for design see figure 4-3-1, right). Due to the shorter emission energy, the field also had to be increased by 60 %. The design uses a similar depletion scheme with two phonon resonances below the lower laser level and two levels in resonance for injection. The low

temperature voltage defect is around 80 meV, slightly dropping over the current. At room temperature, the voltage defect has decreased to 15 to 20 meV, which is even below one optical phonon.

4.4.2 Injection behavior investigations

The original design, using two phonons instead of one for depletion was chosen, to prevent carriers from thermal backfilling into the lower laser state. With a room temperature voltage defect of 40 meV, it became necessary to investigate the injection and depletion mechanisms and the possibility of the performance suffering from thermal backfilling. Therefore the 4-alloy design was taken and modified into two different schemes. The first variation aimed to force the device into using two phonons even at higher temperatures by more diagonal depletion transitions, avoiding the strong leakage path. The second variation added a third phonon resonance beneath the original two and was aiming at three injection resonances, slightly increasing the period length and reducing the electric field. Figure 4-4-4 shows both variations at their design field.

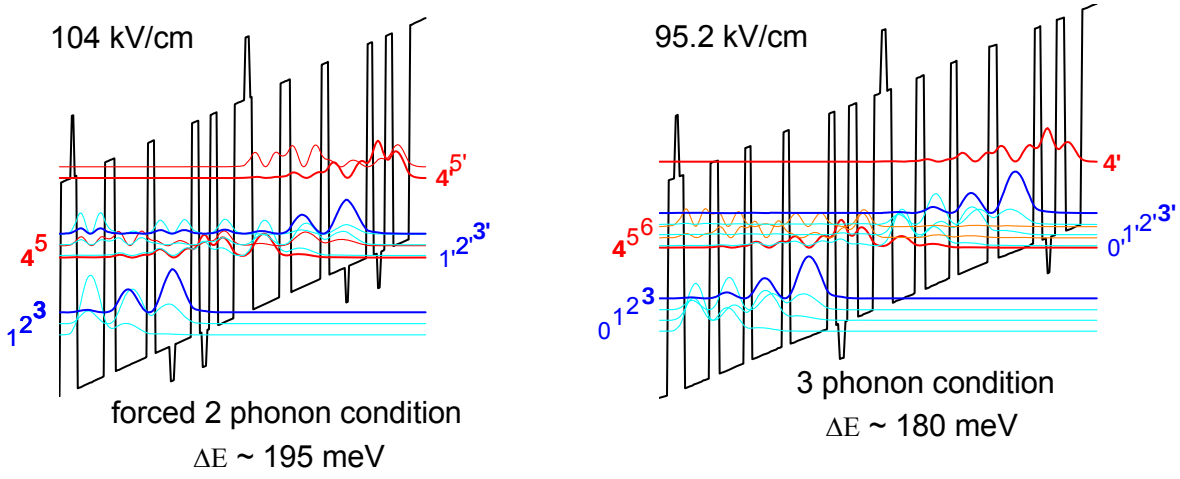

Fig 4-4-4: active region of the 4-alloy reference variations using the forced resonances (left) and the three phonon resonances (right). The layer sequences are **1.5**/***0.6***/**0.6**/4.3/**1.6**/4.9/**1.2**/2.5/*0.6*/2.6/**1.1**/0.6/*0.6*/0.6/**1.1**/2.6 for the left design and **1.1**/***0.6***/**0.9**/3.8/**1.4**/4.2/**1.2**/5.0/**1.0**/5.7/**1.2**/0.7/*0.6*/0.6/**1.3**/2.6 for the right design (both in nm). The four material compositions are indicated as: ***AlAs in bold and italic***, **$Al_{0.635}In_{0.365}As$ in bold**, $Ga_{0.4}In_{0.6}As$ in regular and *InAs in italic style*. The silicon doped layers are indicated by an underline. In comparison to the 4-alloy reference, thicker layers are red, thinner ones blue and new layers green.

Forced two phonon resonance scheme

When forcing the depletion scheme into using two phonons, the coupling strength of state 2' and 4 gets reduced from 7.7 meV to 5.1 meV, limiting the maximum current and forcing the field to increase further. This coupling strength is the minimum energy separation between the two states in resonance. Besides this, the quality of the design was equal, using a slightly higher field and shorter emission

wavelength. From the negative differential resistance, the transit time of 3.6 ps under lasing conditions was estimated, 20 % higher than the 4-alloy reference.

Unfortunately, the forced two phonon design was not immediately reaching the designed resonance condition, but successfully decreased the maximum current possible at fields below the resonance. This decrease in performance, yielding a threshold current density of 1.5 kA/cm^2 and a maximum output power of 250 mW, corresponds to a wall-plug efficiency of 0.5 %. On the other side, the measured voltage defect was 73 meV at room temperature, corresponding to two GaAs *LO*-phonons, proving that it is possible to force the design into its scheme but not recommended as the lifetime increase is mostly contributed to the lifetime of the ground state when lasing.

Three phonon resonance scheme

With three phonons for depletion the design should prevent thermal backfilling much better even with an earlier resonance than designed for. Figure 4-4-5 shows the measured voltage defect for the

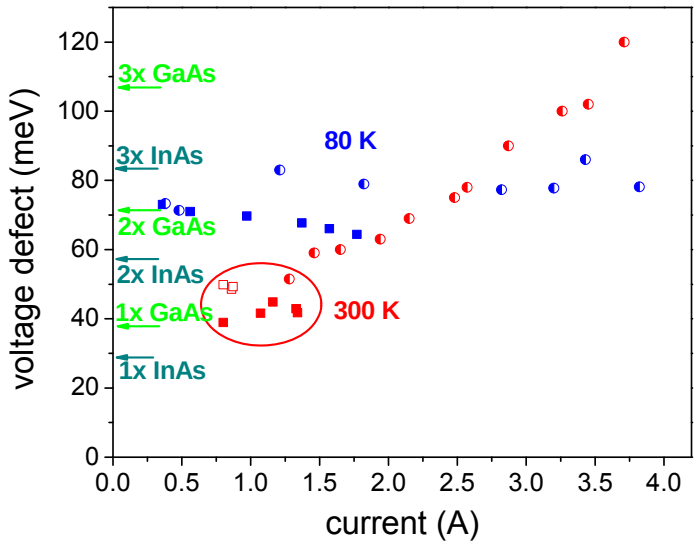

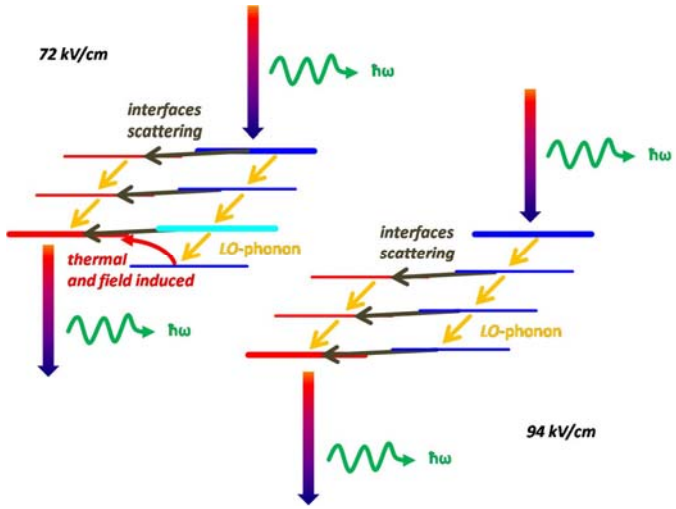

Fig 4-4-5: voltage defect (left) for the 4-alloy reference design (square) and the three-phonon design (circle) for low (blue) and room temperature (red). The lower picture shows the injection schematics for the condition at threshold (72 KV/cm) and the final (design) condition (94 kV/cm)

three phonon design at low and high temperatures in comparison to the other mentioned designs. The injection schematics are displayed below in figure 4-4-5.

The coupling strength was decreased from 7.7 meV to 6.3 meV, on the other side the injection scheme allowed different scattering paths, enabling the device to start lasing with two phonons in resonance. At low temperatures, it remained in a stable phonon condition until the negative differential resistance was reached. This could either mean that two phonons were sufficient and the thermal excitation was strong enough or, more likely, the slight thermal excitation of the carriers already at 80 K is sufficient for resonant depletion with three phonons. At room temperature, the lasing occurred with a voltage defect of 52 meV, which is below two InAs *LO*-phonon energies. It is interesting to see, that the device was able to built up its three-phonon resonance with increasing current, but not by one large step, but over multiple steps with preferred resonances for the interface scattering.

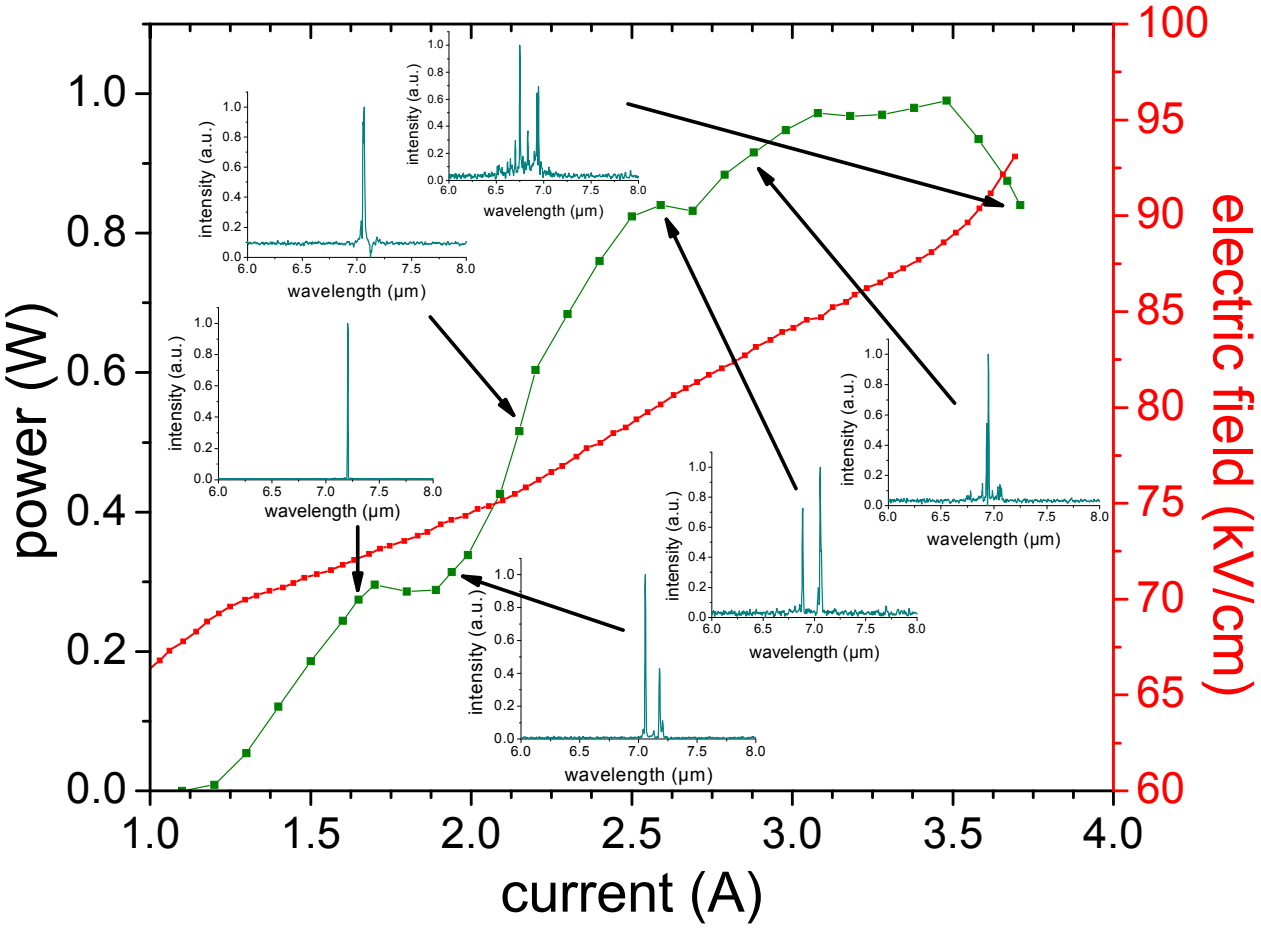

Fig 4-4-6: power (green) and electric field (red) over current at room temperature for the three-phonon design. At threshold with 1.1 kA/cm^2, the change in the differential resistance curve indicates the clamping of the lasing field. Six different spectra are displayed with black arrows indicating the current point, they correspond to.

Figure 4-4-6 shows the calibrated power measurement and the corresponding electrical field at room temperature, which shows a slight clamping at threshold. At specific current points, indicated by arrows, the corresponding spectrum is presented.

Whenever the current reaches its maximum for the arranged resonance condition, the field increases until another resonance condition, suitable for more current is found. This change rips the field clamping apart and results in wavelength shifting. Due to irregularities during the growth, the stages are not all identical and therefore they are shifting at slightly different currents. This difference in currents prevents the macroscopic voltage-current curve from large jumps but enables the device to operate at two different wavelengths in a small current range. It starts at threshold of 1.15 A with an emission wavelength of 7.22 µm. Above 1.75 A the first stages shift towards 7.06 µm. At 2.2 A all stages have shifted to 7.06 µm until another shift towards 6.88 µm occurs at 2.6 A. Finally at 3.4 A the emission spectra shifts again towards a peak wavelength of 6.70 µm. This shift in the transition of more than 13 meV, can be also found in the simulation. Between the electric field of 72.5 kV/cm and 93 kV/cm the expected emission changes from 163 meV to 178 meV, corresponding wavelengths from 7.61 µm to 6.97 µm. This difference of 5 % in wavelength is still in the tolerance of the *MBE* growth, when comparing with the deviation of the reference samples.

Besides this interesting behavior within the emission spectra, the general device performance was good, yielding a threshold current density of 1.1 kA/cm^2. When taking a closer look into the different slope efficiencies, three different ranges can be distinguished. In the first resonance condition, the slope efficiency was measured to be 630 mW/A, increasing to 1.62 W/A during the second resonance condition. At the third resonance condition it drops again to 340 mW/A. This results into 1.0 W of optical power with an overall efficiency of 1.8 %, uncorrected for two facets and collection efficiency.

4.4.3 Transit time and negative differential resistance

A main limitation for high performance when using low doped active regions arises from the limited maximum current density (see equation 2.2.20 & 20b). For increasing the maximum current density, equation 2.2.20b shows only two options. On one side, the doping can be raised, which also increases waveguide losses which directly decrease slope efficiency and increase threshold current density. On the other side, the transit time for an electron can be reduced. Injectorless devices show very short transit times in comparison to injectorbased devices. The design shown in the low threshold chapter has a transit time of 3.0 ps, while the three phonon resonance scheme had a transit time of 3.8 ps in experiment. Injectorbased devices can have low transit times around 5.0 ps [Eva07] but normally are around 8.0 ps [Wan09], due to the many scattering processes in the miniband.

All optimization before was aiming for a very high overlap of the upper laser state and the previous ground state with an energy minimum for fast scattering processes. A different concept, using strong coupling and also a short period length reached a very low value of 2.1 ps [Liu09] on the cost of

performance, as the threshold current density at 300 K reached 3 kA/cm^2. Also latest models of in-plane scattering and dephasing processes [Khu09] indicate an improvement by stronger coupling.

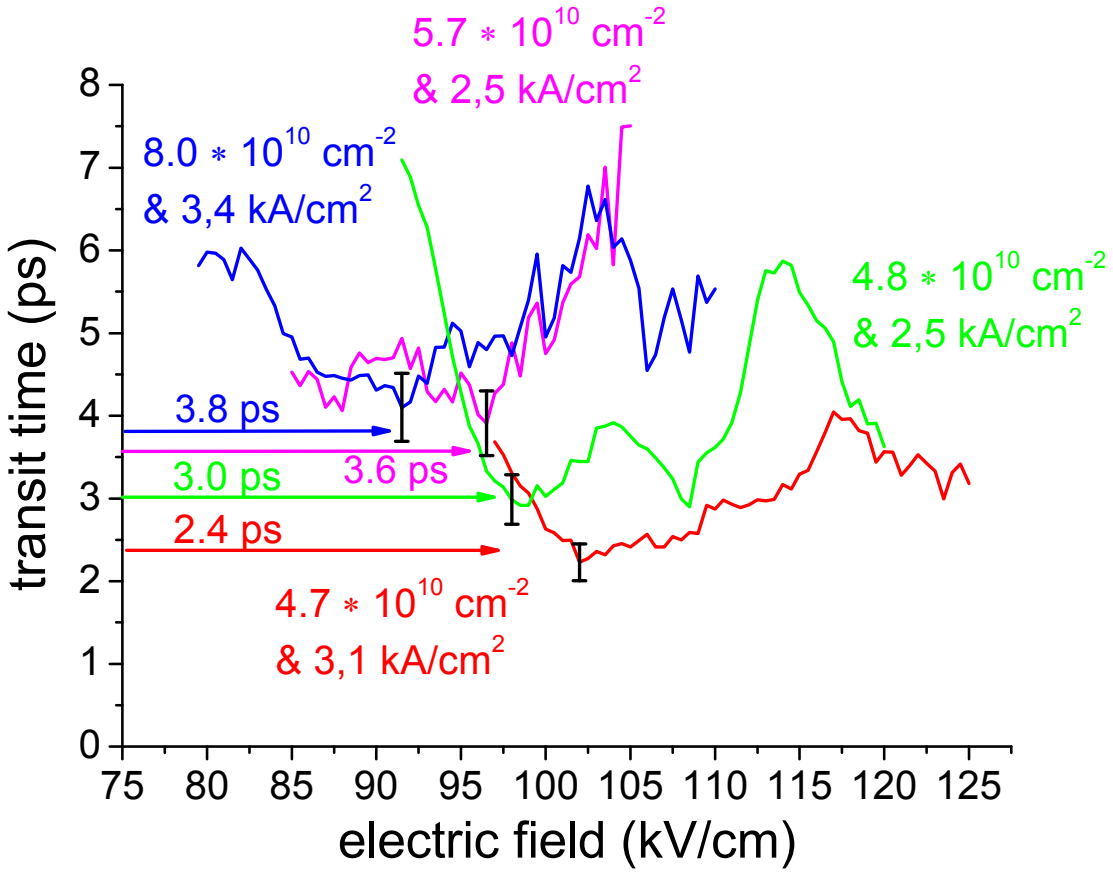

Fig 4-4-7: transit time for various samples, with the solid lines representing the transit times versus the applied field, while the arrows indicate the corresponding experimental values from the negative differential resistance measurement. The black error bars show the doping uncertainty of roughly 10 %. The simulation used an in plane scattering time of 60 fs and a lattice temperature of 295 K, estimating the carrier temperature to 400 K. The lowest value indicates the transit time and the corresponding maximum current density. Besides the different samples (colors), the corresponding doping sheet densities and maximum current densities are given for each design.

For estimation on the injection performance and the corresponding negative differential resistance, a very simple model of in-plane scattering was applied on the one dimensional Schrödinger solver. Every scattering between states, being localized in different periods, are competing with a very fast in plane scattering process with $\tau_{||}$ being the only parameter to be changed. For evaluating the average transit time, electrons at the lower laser state and their scattering behavior by simple rate equations are considered. The scattering by acoustical phonons, optical phonons and interface defects like impurities and roughness are considered. On each state, the scattering mechanisms can be expressed in their probability and the corresponding lifetime. With this information a simulated scattering of 1000 electrons is preformed until they reach the next upper laser level, ignoring electron-electron scattering

and loss mechanisms as ionization for example. Figure 4-4-7 shows the combined results of experiment and simulation.

From previously, with various doping levels, grown structures, like the design shown in figure 4-1-2 (green), the most suitable in plane scattering time constant was determined as 60 fs. With this time constant and the lattice temperature of 295 K, the three phonon design (blue) was evaluated and found to be in agreement with the model. It is also in good agreement with the value determined by Faist [Fai07].

Two different concepts were then applied on the original injectorless scheme (green) and their transit time estimated before the growth. The first idea was to apply the previously mentioned strong coupling approach (red), and the second one was an additional asymmetric depletion scheme (pink), which improved the characteristic temperature of a short injector design [Viz09]. Figure 4-4-8 shows the two schemes in principle, with the dominant current path of two phonon scatterings and a vertical transport being indicated.

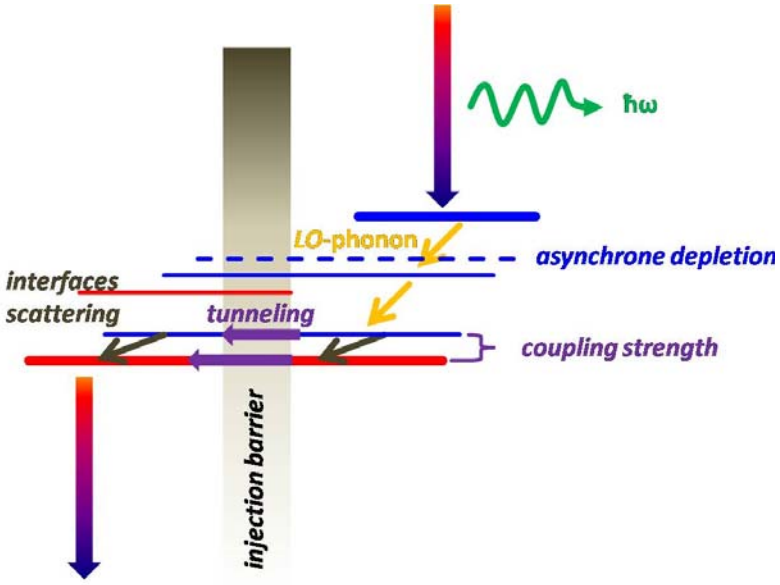

Fig 4-4-8: strong coupling and asymmetric (dashed blue line) depletion principles.

Many different scattering processes can transport the electron from the ground state (lowest blue) to the upper laser level (thick red), a transport through the injection barrier is still required. A weak coupling means that the two states are energetically close but spatially further separated with a smaller overlap, while a strong coupling means a larger overlap but an energetically larger separation.

$$E = 2\hbar\omega_c \qquad (4.4.1)$$

The lifetime for interface defect and acoustical phonon scattering increases with larger energy separation, while the tunneling time decreases, according to the coupling energy (equation 4.4.1). Besides the lifetimes, also the gain curve is broadened by a stronger coupling. All previously mentioned designs had a coupling strength of 4.0 to 6.0 meV at resonance for the ground state and the upper laser state. The simulations indicated that a coupling around 10 meV should increase the maximum current density at equal doping about 20 %, while maintaining the quality factor.

As second step, the regularly symmetric depopulation by two optical phonons was changed towards a smaller and a larger energy separation for improving the characteristic temperature, also

called asymmetric scheme. With increasing lattice temperature, the electron distribution heats up and shifts away from the optical phonon energies. Therefore an energy separation below the optical phonon energy could help depleting the lower laser level. Because the second step is less critical in the depletion and to suppress effects from thermal backfilling, the ground state and the intermediate state are then separated by an energy step larger than the optical phonon energy. In addition, the strong coupling was also applied to this sample. All samples had similar thicknesses in period, active zone and waveguide. They also used equal doping levels and were grown one after the other without any changes being applied in between the growths.

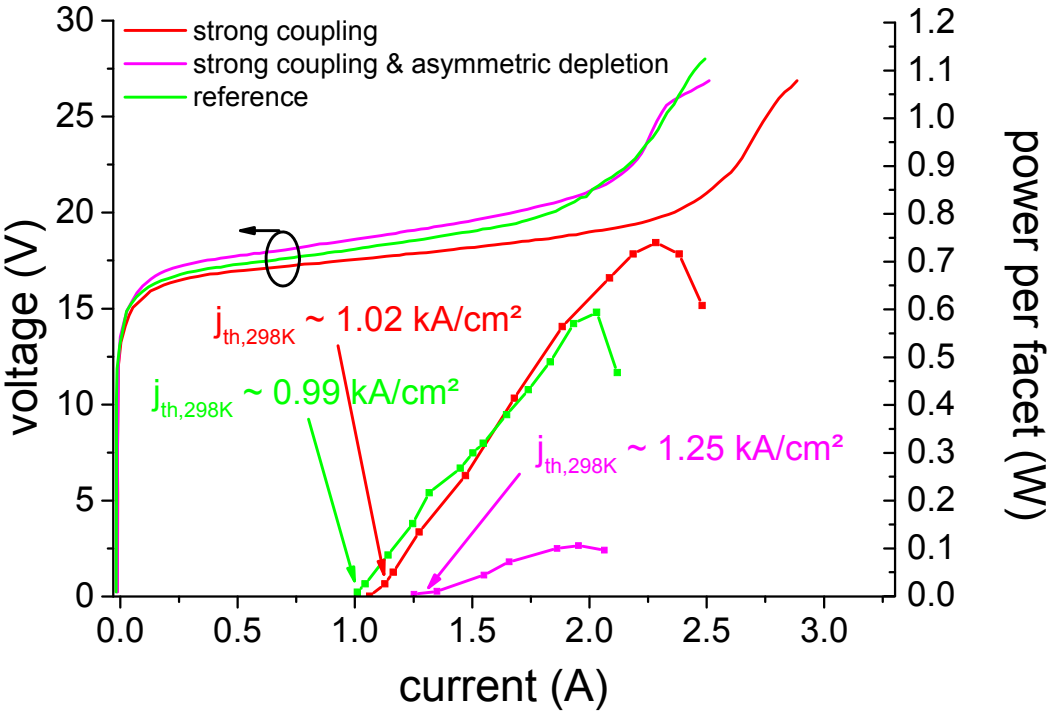

Fig 4-4-9: performance of the reference (green), the strong coupling (red) and the asymmetric depletion (pink) sample. The voltage current curves are measured at 80 K, while the output power versus current was measured at room temperature.

Figure 4-4-9 shows the negative differential resistances of the two samples together with the corresponding reference measured at liquid nitrogen. Small variations in each period, caused by flux and temperature shifts during the growth, modify the negative differential resistance of each period slightly. Therefore the voltage-current characteristics seldom show a sharp jump, but quite often a negative differential region. When differentiating with respect to current density, the reference showed a maximum at 1.67 kA/cm^2, while the strong coupling sample increased to 2.05 kA/cm^2. Shortly after the first occurrence of a negative differential behavior, the output power starts decreasing. With equal doping densities, a higher output power, 740 mW instead of 600 mW, and better efficiency, 1.8 %

instead of 1.4 % at room temperature, were reached. This corresponds to an improvement of 24 %, as predicted by equation 2.2.20. For further improvements, this injection behavior has to be optimized for every design independently.

Conclusion

This thesis covers many aspects of injectorless devices ranging from theoretical description of the devices to technological issues. While injectorless quantum cascade lasers had already achieved record low pulsed threshold current densities of 0.73 kA/cm^2, their pulsed threshold power was still slightly higher with 70 MW/cm^3 compared to injectorbased devices. The best injectorbased devices reach values of 46 MW/cm^3 for coated [Die06] and 56 MW/cm^3 for uncoated devices [Wan07] in January 2010. With the implementation of InAs and AlAs within the active region design, the performance of the devices was successfully increased. Their pulsed threshold current density reached record low values of 0.45 kA/cm^2, yielding a power density of 38 MW/cm^3 for coated devices [Boe09]. Uncoated device reached values of 54 MW/cm^3 with a threshold current density of 0.57 kA/cm^2 [Kat08]. Tab 5.1 summarizes the results in comparison to the best performing injectorless devices from 2007.

$j_{th,300K}$	**0.73 kA/cm^2**	**#1**	**0.45 kA/cm^2**	**- 22 %**	**#1**
T_{max}	430 K	#2	440 K	~	#1’
T_0	90 K	#1	150 K	**+ 67 %**	**#1**
$P_{max,296K}$	**240 mW**	**#2**	**1300 mW**	**+ 440 %**	**#2**
WPE	**2.4 %**	**#2**	**7.1 %**	**+ 196 %**	**#2**
dP/dI	260 mW/A	#2	1300 mW/A	**+ 400 %**	**#2**

Tab 5.1: Summary of best performing injectorless devices using two alloy (orange) and multialloy structures (green). WPE stands for wall plug efficiency and the number (#) indicates different designs or doping levels. WPE takes two facets and collection efficiency of 70 % into account.

But also in comparison to injector based devices, the performance was improved. A comparison of pulsed threshold current density at 300 K and overall efficiency (*WPE*) with state of the art injector-based devices is shown in figure 5-1. The threshold current density is roughly a factor two lower compared to the best injectorbased devices. This is in good agreement with the experimentally verified higher gain coefficient. The wall-plug efficiency is comparable to most injectorbased but hasn’t reached high performance injector-based devices [Lya09][Wan09]. Considering the development of the last years, in which injector based devices increased their performance from 9.3 % up to 15.1 %, the injectorless designs have tripled their overall efficiency from 2.4 % to 7.1 %.

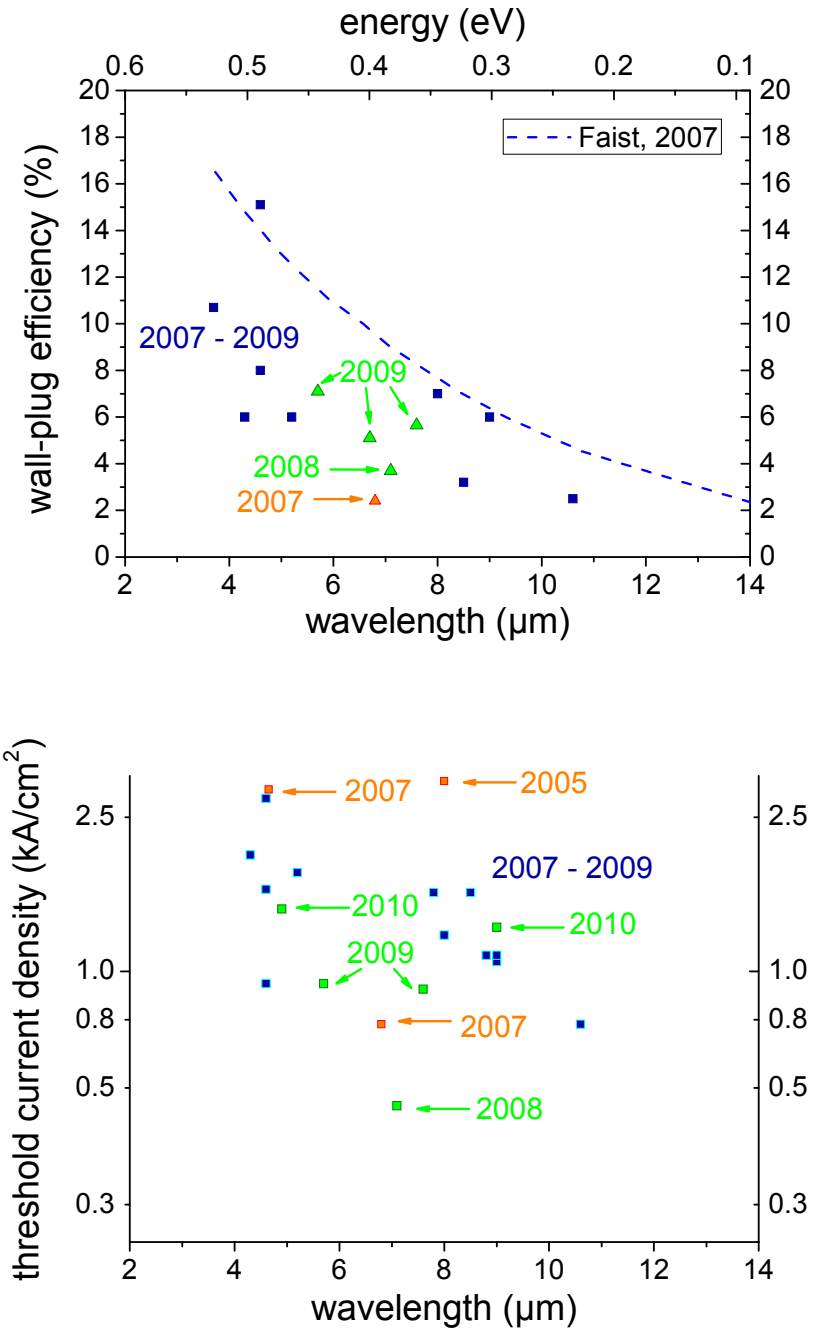

Fig 5-1: Comparison of overall efficiency (top) and pulsed threshold current density (bottom) between injector-based devices (dark blue filled) and injectorless devices using two alloys (orange filled) and newly developed multi alloy devices (green filled). The blue line indicates the theoretical dependency over the emission wavelength of the overall efficiency. All devices have both facets and collection efficiency taken into account.

Besides the very successful designs around 7 µm emission wavelength, short wave and long wave designs have been investigated, showing a general improvement, compared to previous injectorless designs.

Besides the achieved improvements in pulsed operation, continuous wave operation for injectorless devices was realized for the first time [Kat08][Kat09b]. This was possible due to improved active region designs in combination with a more sophisticated process, combing dry and wet etching, different insulation techniques and the in-depth investigation of thermal resistances in dependency of process and setup technology. The best continuous wave threshold current density was achieved with 1.76 kA/cm^2.

For further improving the threshold performance of injectorless devices, either completely new concepts in design or new material systems like GaSb have to be chosen. The change towards GaSb for injectorless devices will require intense research on the epitaxial side, consuming money and manpower. First devices will most likely suffer from bad material quality as mixed group-V interfaces come into play, limiting the performance.

Otherwise small but steady improvements within the latest concepts can be made, when investigating barrier thicknesses and doping levels furthermore. A larger improvement can be expected on the performance side of injectorless devices, as they are still slightly behind the injector based devices, although their slope efficiencies should be much larger. With the threshold current and power densities having outdated the injectorbased devices, injectorless devices have proven their competitiveness. With three generations of workers on injectorless devices, they are mature enough for applications by now. This requires not only continuous wave but also single mode operation for gas sensing or communication technologies.

Appendix A - Abbreviations and Symbols

CW	continuous wave, in opposition to pulsed operation
CCD	charge coupled device
DBR	distributed Bragg reflector
dc	duty cycle, in pulsed operation
FIR	far infrared
FWHM	full width half maximum
HR	high reflective (coating)
LIV	light-current-voltage (characteristics)
LD	laser diode
LO	longitudinal optical (phonons)
LA	longitudinal acoustical (phonons)
MBE	molecular beam epitaxy
MCT	mercury cadmium tellurid (detector)
MIR	mid infrared
ML	monolayer, roughly half the lattice constant
MOCVD	metal-organic chemical vapor deposition
PECVD	plasma enhanced chemical vapor deposition
QCL	quantum cascade laser
RIE	reactive ion etching
SEM	scanning electron microscope
THz	terahertz, 10^{12} Hz
TE	transversal electric
TM	transversal magnetic

WPE	wall plug efficiency, also called overall efficiency
XRD	x-ray diffraction

A	area of device
α_i	internal losses
α_m	mirror losses
α_{tot}	total losses
$\bar{c}, c$	effective speed of light and vacuum speed of light
C	heat capacity per unit of volume
δ	skin depth of electromagnetic wave
e	elementary charge
ε	complex dielectric constant
E_c	conduction band energy
$E_{g,eff}$	effective band gap
E_n	energy of state *n*
$E_{x,y,z}$	electric field component in x,y and z direction of electromagnetic wave
g_c	gain coefficient
g_p	peak material gain
g_{mod}	modal gain, determined by confinement factor and material gain
γ_{if}	line width of transition between state *i* and *f*
$H_{x,y,z}$	magnetic field component in x,y and z direction of electromagnetic wave
$\hbar$	planck's constant divided by two π
Γ	confinement factor, fraction of wave being guided within the active region
j	current density

j_{th}	threshold current density
j_{max}	maximum current density
j_{heat}	heat flux
k_o	wave number of the vacuum
k_B	Boltzmann constant
λ	wavelength, but also number of mutants in evolution algorithm
λ	thermal conductivity, only in case of thermal simulations
L	length of optical resonator
L_p	length of period/stage
M^2	beam quality factor of Gaussian beam
m_{eff}	effective mass of carrier, material and energy dependent
n_i	carrier density of state *i*
n_s	sheet carrier density, volume doping density times layer thickness
n	refractive index
n_{eff}	complex effective refractive index
n'_{eff}	real part of effective refractive index
η_i	injection efficiency into state *i*
$\varphi_n(x)$	carrier envelope function of state *n*
P_{el}	electrical power
$R_{1,2}$	power reflectivity of facet 1,2
R_{th}	thermal resistance of device
S	photon density
σ_c	gain cross section coefficient
σ	electric conductivity

τ_{if}	lifetime for the transition between state *i* and *f*
$\tau_{i,f}$	overall lifetime of state *i* or *f*
τ_{trans}	transit time for carriers per period/stage
T	temperature
T_0	characteristic temperature, describing thermal dependences
μ_0	vacuum permeability
μ	number of parents in evolution algorithm
V_c	potential of conduction band, defined by materials
V_{el}	potential caused by external field
w_0	beam waist at facet
$w(z)$	beam waist in propagation direction
ω	angular frequency of electromagnetic wave
ω_{LO}	frequency of optical phonon mode
χ	susceptebility
z_{if}	dipole matrix element between state *i* and *f*
z_r	Rayleigh length

Appendix B - References

[Ada10] R. Adams, A. Vizbaras, C. Grasse, S. Katz, G. Boehm, M. Jang, M.-C. Amann, and M. Belkin, „Terahertz sources based on difference-frequency generation near exit facets in dual wavelength mid-infrared quantum cascade lasers“, Conference on Lasers and Electro-Optics, 2010 (submitted).

[Ama09] M. Amanti, M. Fischer, G. Scalari, M. Beck, and J. Faist, “Low-divergence single-mode terahertz quantum cascade laser”, Nature Photonics, 2009. **3**, pp. 586-590.

[App07] R. Appleby, and R. Anderton, “Millimeter-Wave and Suibmillimeter-Wave Imaging for Security and Surveillance”, Proc. IEEE, 2007, **95**, pp. 1683-1690.

[Bak07] C. Baker, T. Lo, W. Tribe, B. Cole, M. Hogbin, and M. Kemp, “Detection of Concealed Explosives at a Distance using Terahertz Technology”, Proc. IEEE, 2007, **95**, pp. 1559-1565.

[Bel07] M. Belkin, F. Capasso, A. Belyanin, D. Sivco, A. Cho, D. Oakley, C. Vineis, and G. Turner, “Terahertz quantum-cascade-laser source based on intracavity difference frequency generation”, Nature photonics, 2007, **1**, pp. 288-292.

[Bel08] M. Belkin, J. Fan, F. Capasso, et al., “Terahertz quantum cascade lasers with copper metal-metal waveguides operating up to 178 K”, Optics Express, 2008, **16**, pp. 3242-3248.

[Bel08b] M Belkin, F. Capasso, F. Xie, A. Belyanin, M. Fischer, A. Wittmann, and J. Faist, “Room temperature terahertz quantum cascade laser source based on intracavity difference frequency generation”, Appl. Phys. Lett., 2008, **92**, 201101.

[Bel09o] M. Belkin, personal communication

[Ben09] E. Benveniste, S. Laurent, A. Vasanelli, C. Manquest, C. Sirtori, F. Teulon, M Carras, and X. Marcadet, “Measurement of gain and losses of a midinfrared quantum cascade laser by wavelength chirping spectroscopy”, Appl. Phys. Lett., 2009, **94**, 081110.

[Bla07] S. Blaser, A. Bächle, J. Faist, et al., „Low-consumption (below 2W) continuous wave singlemode quantum-cascade lasers grown by metal-organic vapour-phase epitaxy“, Electron. Lett., 2007, **43**, pp. 1201-1202.

[Boc90] U. Bockelmann, and G. Bastard, “Phonon scattering and energy relaxation in two-, one-, and zero-dimensional electron gases”, Phys. Rev. B, 1990, **42**, pp. 8947-8951.

[Boe09] G. Boehm, S. Katz, R. Meyer, and M.-C. Amann, „Al(In)As-Ga(In)As strain-compensated active regions for injectorless quantum cascade lasers”, J. Crystal Growth, 2009, **311**, pp. 1932-1934.

[Bor02] T. Borca-Tasciuc, J. Meyer, I. Vurgaftmann et al., “Thermal conductivity of $AlAs_{0.07}Sb_{0.93}$ and $Al_{0.9}Ga_{0.1}As_{0.07}Sb_{0.93}$ alloys and $(AlAs)_1/(AlSb)_{11}$ digital-alloy superlattices”, J. Appl. Phys., 2002, **92**, pp. 4994-4998.

[Bot89] W. Both, A. Bochkarev, A. Drakin, and B. Sverdlov, “Thermal Resistivity of Quaternary Solid Solutions InGaAsSb and GaAlAsSb Lattice-matched to GaSb”, Cryst. Res. Technol., 1989, **24**, pp. K161-K166.

[Bou09] A. Bousseksou, Y. Chassagneux, J. Coudevylle, R. Colombelli, C. Sirtori, G. Patriarche, G. Beaudoin, and I. Sagnes, *“Surface-plasmon distributed-feedback quantum cascade lasers operating pulsed, room temperature”*, Appl. Phys. Lett., 2009, **95**, 091105.

[Bra09] G. Bracher, “Waveguide concepts for InP-based terahertz quantum cascade lasers”, WSI Diploma Thesis, 2009.

[CasH78] H. C Casey, and M. B. Panish, “Heterostructure Lasers”, Academic Press, 1978.

[Cha74] L. Chang, L. Esaki, and R. Tsu, “Resonant tunneling in semiconductor double barriers”, Appl. Phys. Lett., 1974, **24**, pp. 593-595.

[Com02] F. Compagnone, A. Di Carlo, and P. Lugli, “Monte carlo simulation of electron dynamics in superlattice quantum cascade lasers”, Appl. Phys. Lett., 2002, **80**, pp. 920-922.

[Con50] E. Conwell, and V. F. Weisskopf, “Theory of Impurity Scattering in Semiconductors”, Phys. Rev., 1950, **77**, pp. 388-390.

[Dar06] S. Darvish, S. Slivken, A. Evans, J. Yu, and M. Razeghi, “Room-temperature, high-power, and continuous-wave operation of distributed-feedback quantum-cascade lasers at λ ~ 9.6 µm”, Appl. Phys. Lett., 2006, **88**, 201114.

[Det05] J. Detlefsen, “Mikrowellensystemtechnik”, 2005.

[Dev06] J. Devenson, D. Barate, O. Cathabard, R. Teissier, and A. Baranov, “Very short wavelength (λ=3.1-3.3 µm) quantum cascade lasers”, Appl. Phys. Lett., 2006, **89**, 191115.

[Dev07a] J. Devenson, O. Cathabard, R. Teissier, and A. Baranov, “High temperature operation of λ≈3.3 µm quantum cascade lasers”, Appl. Phys. Lett., 2007, **91**, 141106.

[Dev07b] J. Devenson, O. Cathabard, R. Teissier, and A. Baranov, “InAs/AlSb quantum cascade lasers emitting at 2.75-2.97 µm”, Appl. Phys. Lett., 2007, **91**, 251102.

[Dey09] D. Dey, W. Wu, O. Memis, and H. Mohseni, “Injectorless quantum cascade laser with low voltage defect and improved thermal performance grown by metal-organic chemical-vapor deposition”, Appl. Phys. Lett., 2009, **94**, 081109.

[Die06] L. Diehl, D. Bour, S. Corzine, J. Zhu, G. Hoefler, M. Loncar, M. Troccolli, and F. Capasso, “High-power quantum cascade lasers grown by low-pressure metal organic vapor-phase epitaxy operating in continuous wave above 400 K”, Appl. Phys. Lett., 2006, **88**, 201115.

[Die07] O. Dier, “ Das Materialsystem (AlGaIn)(AsSb): Eigenschaften und Eignung für GaSb-basierte Vertikalresonator-Laserdioden”, WSI PhD Thesis, 2002.

[Doe09] V. Doering, „Development and Characterization of Active Regions for THz Quantum Cascade Lasers Based on InP“, WSI Diplma Thesis, 2009.

[Eic91] J. Eichler, and H.-J. Eichler, „Laser – Grundlagen,Systeme,Anwendungen“, Springer Verlag, 1991.

[Esa70] L. Esaki, and R. Tsu, “Superlattice and negative differential conductivity in semiconductors”, IBM J. of Research and Dev., 1970, **14**, pp. 61.

[Esc09] M. Escarra, A. Hoffman, K. Franz, S. Howard, R. Cendejas, X. Wang, J. Fan, and C. Gmachl, “Quantum cascade lasers with voltage defect of less than one longitudinal optical phonon energy”, Appl. Phys. Lett., 2009, **94**, 251114.

[ETH09] http://www.photonics.ethz.ch/research/core_competences/technology/epitaxial__growth/mbe, © 2009 ETH Zurich

[Eva07] A. Evans, S. darvish, S. Slivken, J. Nguyen, Y. Bai, and M. Razeghi, “Buerid heterostructure quantum cascade lasers with high continuous-wave wall plug efficiency”, Appl. Phys. Lett., 2007, **91**, 071101.

[Fai94] J. Faist, F. Capsso, D. L. Sivco, A. L. Hutchinson and A. Y. Cho, “Quantum Cascade Laser”, Science, 1994, **264**, pp. 553-556.

[Fai95] J. Faist, F. Capasso, C. Sirtori, D. Sivco, A. Hutchinson, and A. Cho, “Continuous wave operation of a vertical transition quantum cascade laser above T=80 K”, Appl. Phys. Lett., 1995, **67**, pp. 3057-3059.

[Fai07] J. Faist, "Wallplug efficiency of quantum cascade lasers: Critical parameters and fundamental limits", Appl. Phys. Lett., 2007, **90**, 253512.

[Fer89] R. Ferreira, and G. Bastard, "Evaluation of some scattering times for electrons in unbiased and biased single and multiple-quantum well structures", Phys. Rev. B, 1989, **40,** pp. 1074-1086.

[Fis08] M. Fischer, G. Scalari, C. Walther, and J. Faist, "Terahertz quantum cascade lasers based on $In_{0.53}Ga_{0.47}As/In_{0.52}Al_{0.48}As/InP$", J. Crystal Growth, 2008, **311**, pp. 1939-1943.

[Fou91] Y. Foulon, and C. Priester, "Confinement and parallel-conduction effective mass in an ultrathin strained quantum-well system", Phys. Rev. B, 1991, **44**, pp. 5889-5892.

[Fra09] K. Franz, P. Liu, J. Raftery, M. Escarra, A. Hoffmann, S. Howard, Y. Yao, Y. Dikmelik, X. Wang, J.-Y. Fan, J. Khurgin, and C. Gmachl, "Short Injector Quantum Cascade Lasers", J. Quant. Elec., 2009, in press.

[Fri05] A. Friedrich, G. Scarpa, G. Boehm, and M.-C. Amann, "Quantum-cascade lasers without injector regions operating above room temperature", Appl. Phys. Lett., 2005, **86**, 161114.

[Fri06] A. Friedrich, C. Huber, G. Boehm, and M.-C. Amann, „Low-threshold room temperature operation of injectorless quantum cascade lasers: influence of doping density", Electron. Lett., 2006, **42**, pp. 1228-1229.

[Fri07] A. Friedrich, G. Boehm, and M.-C. Amann, "Short-Wavelength intersubband staircase lasers, with and without AlAs blocking barriers", Semicond. Sci. Technol., 2007, **22**, pp. 218-221.

[Gor55] J. Gordon, H. Zeiger, and C. Townes, "The Maser – New Type of Microwave Amplifier, Frequency Standard and Spectrometer", Phys. Rev., 1955, **99**, pp. 1264-1274.

[Gor96] V. Gorfinkel, S. Luryi, and B. Gelmont, "Theory of Gain Spectra for Quantum Cascade Lasers and Temperature Dependence of their Characteristics at Low and Moderate Carrier Concentrations", IEEE J. Quantum Electron., 1996, **32**, pp. 1995-2003.

[Gra10] C. Grasse, G. Boehm, M. Mueller, T. Gruendl, R. Meyer, and M.-C. Amann, *„Empirical modeling of the refractive index for (AlGaIn)As lattice matched to InP"*, Semicond. Sci. Technol., 2010, in press.

[Gre04] R. Green, C. Pflügl, J. Cockburn, G. Strasser, et al., „High-performance distributed feedback quantum cascade lasers grown by metalorganic vapor phase epitaxy", Appl. Phys. Lett., 2004, **85**, pp. 5529-5531.

[Gre09] T. Gresch, J. Faist, and M. Giovannini, "Gain measurements in strain-compensated quantum cascade laser", Appl. Phys. Lett., 2009, **94**, 161114.

[Gro04] R. Gross, and A. Marx, "Festkörperphysik," Lecture Script, 2004, WMI, Garching.

[Hal62] R. Hall, G. Fenner, J. Kingsley, T. Soltys, and R Carlson, "Coherent light emission from GaAs junctions", Phys. Rev. Lett., 1962, **9**, pp. 366-368.

[Hak73] B. Hakki, and T. Paoli, "cw degradation at 300 K of gaAs double-heterostructure junction lasers. II. Electronic gain", J. Appl. Phys., 1973, **44**, pp. 4113-4119.

[Hak74] B. Hakki, and T. Paoli, "Gain spectra in GaAs double-heterostructure injection lasers", J. Appl. Phys., 1975, **46**, pp. 1299-1306.

[Hof99] D. Hofstetter, and J. Faist, "Measurement of semiconductor laser gain and dispersion curves utilizing Fourier transforms of emission spectra," IEEE Phot. Technol. Lett., 1999, **11**, pp.1372-1374.

[Hof07] A. Hoffman, S. Schartner, S. Howard, K. Franz, F. Towner, and C. Gmachl, „Low voltage-defect quantum cascade laser with heterogeneous injector regions", Optics Express, 2007, **15**, pp. 15818-15823.

[Hsu09] A. Hsu, B. Williams, and Q. Hu, “Four-Well Highly Strained Quantum Cascade Lasers grown by metal-organic chemical vapor deposition”, CLEO conference, 2009, CThL2.

[Iof] Ioffe Insitut, St. Petersburg, Russia, http://www.ioffe.rssi.ru/SVA/NSM/Semicond/ index.html

[Iot01] R. C. Iotti, and F. Rossi, “Nature of charge transport in quantum-cascade lasers”, Phys. Rev. Lett., 2001, **87**, 146603.

[Jav61] A. Javan, W. Bennett, and D. Herriott, „Population inversion and continuous optical maser oscillation in a gas discharge containing a He-Ne mixture”, Phys. Rev. Lett., 1961, **6**, pp. 106-110.

[Kas09] K. Kashani-Shirazi, K. Vizbaras, A. Bachmann, S. Arafin, and M.-C. Amann, „Low.-Threshold Strained Quantum-Well GaSb-based Lasers emitting in the 2.5- to 2.7-µm Wavelength Range”, IEEE Phot. Technol. Lett., 2009, **21**, pp. 1106-1108.

[Kat07] S. Katz, “Herstellung und Untersuchung von Quantenkaskadenlasern mit zweistufigen Barrieren”, WSI Diploma Thesis, 2007.

[Kat08] S. Katz, G. Boehm, and M.-C. Amann, „Low-threshold injectorless quantum cascade laser with four material compositions“, Electron. Lett., 2008, **44**, pp. 580-581.

[Kat08b] S. Katz, A. Friedrich, G. Boehm, and M.-C. Amann, „Continuous Wave operation of injectorless quantum cascade lasers at low temperatures“, Appl. Phys. Lett., 2008, **92**, 181103.

[Kat09] S. Katz, A. Vizbaras, G. Boehm, and M.-C. Amann, „High-performance injectorless quantum cascade lasers emitting below 6 µm“, Appl. Phys. Lett., 2009, **94**, 151106.

[Kat09b] S. Katz, A. Vizbaras, G. Boehm, and M.-C. Amann, „Injectorless Quantum Cascade Laser Operating in Continuous Wave above Room Temperature”, Semicond. Sci. Technol., 2009, **24**, 122001.

[Kaz71] R. Kazarinov, and R. Suris, “Possibility of the Amplification of Electromagnetic Waves in a Semiconductor with a Supperlattice”, Sov. Phys. Semicond., 1971, **5**, pp. 707-709.

[Khu09] J. Khurgin, Y. Dikmelik, P. Liu, A. Hoffman, M. Escarra, K. Franz, and C. Gmachl, „Role of interface roughness in the transport and lasing characterstics of quantum cascade lasers“, Appl. Phys. Lett., 2009, **94**, 091101.

[Kit84] C. Kittel, and H. Krömer, “Physik der Wärme”, R. Oldenbourg Verlag, 1984.

[Koe09] K. Koksal, B. Gonul, and M. Oduncuoglu, “Critical layer thickness of GaIn(N)As(Sb) QWs on GaAs and InP substrates for (001) and (111) orientation”, Eur. Phys. J. B, 2009, **69**, pp. 211–218.

[Kos02] A. Kosterev, and F. Tittel, „Chemical Sensors based on Quantum Cascade Lasers“, J. Quantum Electron., 2002, **38**, pp. 582-591.

[Kub09] T. Kubis, C. Yeh, P. Vogl, A. Benz, G. Fasching, and C. Deutsch, „Theory of nonequilibrium quantum transport and energy dissipation in terahertz quantum cascade lasers”, Phys. Rev. B, 2009, **79**, 195323.

[Kum09] S. Kumar, Q. Hu, and J. Reno, „186 K operation of terahertz quantum-cascade lasers based on a diagonal design“, Appl. Phys. Lett., 2009, **94**, 131105.

[Lam08] N. Laman, S. Harsha, D. Grischkowsky, and J. Melinger, “High-Resolution Waveguide THz Spectroscopy of Biological Molecules”, Bio. Phys. J., 2008, **94**, pp. 1010-1020.

[Le07] K. Le, and S. Kim, “Model for cross-plane thermal conductivity of layered quantum semiconductor structures and application of thermal modeling of GaInAs/AlInAs-based quantum cascade lasers”, Phys. Stat. Sol. A, 2007, **205**, pp. 392-396.

[Lee02] S. Lee, and A. Wacker, "Nonequilibrium Green's function theory for transport and gain properties of quantum cascade structures", Phys. Rev. B, 2002, **66**, 245314.

[Lee06a] A. Lee, B. Williams, S. Kumar, Q. Hu, and J. Reno, "Real-Time Imaging Using a 4.3-THz Quantum Cascade Laser and a 320 x 240 Microbolometer Focal Plane Array", Phot. Technol. Lett., 2006, **18**, pp. 1415-1417.

[Lee06b] A. Lee, Q. Qin, S. Kumar, B. Williams, Q. Hu, and J. Reno, „Real time terahertz imaging over a standoff distance (> 25 meters)", Appl. Phys. Lett., 2006, **89**, 141125.

[Lee07] A. Lee, Q. Qin, S. Kumar, B. Williams, Q. Hu, and J. Reno, „High-power and high temperature THz quantum-cascade lasers based on lens-coupled metal-metal waveguides", Optics Lett., 2007, **32**, pp. 2840-2842.

[Lew09] R. Lewicki, J. Doty, R. Curl, F. Tittel, and G. Wysocki, "Ultrasensitive detection of nitric oxide at 5.33 μm by using external cavity quantum cascade laser-based Faraday rotation spectroscopy", PNAS, 2009, **106**, pp. 12587-12592.

[LiuC00] H.C. Liu, and F. Capasso, "Intersubband Transitions in Quantum Wells: Physics and Device Applications II", Academic Press, 2000.

[Liu09] P. Liu, A. Hoffman, M. Escarra, K. Franz, J. Khurgin, Y. Dikmelik, X. Wang, J.-Y. Fan, and C. Gmachl, „Quantum Cascade Lasers with Ultra-Strong Coupling Injection", Proceedings of CLEO, 2009, CThL1, Baltimore.

[Loe07] T. Loeffler, K. Siebert, N. Hasegawa, T. Hahn, and H. Roskos, „All-optoelectronic Terahertz Imaging Systems and Examples of their Application", Proc. IEEE, 2007, **95**, pp. 1576-1582.

[Lop06] A. Lops, V. Spagnolo, and G. Scamarcio, "Thermal modeling of GaInAs/AlInAs quantum cascade lasers", J. Appl. Phys., 2006, **100**, 043109.

[Lya08] A. Lyakh, C. Pflügl, L. Diehl, Q. Wang, F. Capasso, X. Wang, J. Fan, T. Tanbun-Ek, R. Maulini, A. Tsekoun, R. Go, and C. K. Patel, "1.6 W high wall plug efficiency, continuous-wave room temperature quantum cascade laser emitting at 4.6 μm", Appl. Phys. Lett., 2008, **92**, 111110.

[Lya09] A. Lyakh, R. Maulini, A. Tsekoun, R. Go, C. Pflügl, L. Diehl, Q. Wang, F. Capasso, and K. Patel, "3W continuous wave room temperature single facet emission from quantum cascade lasers based on nonresonant extraction design approach", Appl. Phys. Lett., 2009, **95**, 141113.

[Mai60] T. Maiman, "Stimulated Optical Emission in Ruby", Nature, 1960, **187**, pp. 493-494.

[Mar05] R. Martini, and E. Whittaker, "Quantum cascade laser-based free space optical communications", J. Opt. Fiber Commun. Rep., 2005, **2**, pp. 279-290.

[Mat74] J. Matthews, and E. Blakeslee, "Defects in epitaxial multilayers", J. Crystal Growth, 1974, **27**, pp. 118-125.

[Mel02] Melles Griot, "Optics Guide – Gaussian Beam Propagation" & "Optics Guide – Real Beam Propagation", 2002.

[Nel08] D. Nelson, J. McManus, S. Herndon, M. Zahniser, B. Tuzson, L. Emmenegger, „New method for isotopic ratio measurements of atmospheric carbon dioxide using a 4.3 μm pulsed quantum cascade laser", Appl. Phys. B., 2008, **90**, pp 301-309.

[Ord84] M. Ordal, L. Long, R. J. Bell, S. Bell, R. R. Bell, R. Alexander, and C. Ward, "Optical properties of the metals Al, Co, Cu, Au, Fe, Pb, Ni, Pd, Pt, Ag, Ti, and W in the infrared and far infrared", Appl. Optics, 1983, **22**, pp. 1099-1120.

[Ord85] M. Ordal, R. Bell, R. Alexander, L. Long, and M. Querry, "Optical properties of fourteen metals in the infrared and far infrared: Al, Co, Cu, Au, Fe, Pb, Mo, Ni, Pd, Pt, Ag, Ti, V, and W", Appl. Optics, 1983, **24**, pp. 4493-4499.

[Pal85] E. Palik, “Handbook of optical constants of solids”, Academic Press, 1985.

[Pat08] C. K. N. Patel, “Laser photoacoustic spectroscopy helps fight terrorism: High sensitivity detection of chemical warfare agent and explosives”, Eur. Phys. J. Special Topics, 2008, **153**, pp. 1-18.

[Pat09] C. K. N. Patel, “High power quantum cascade lasers and applications”, Plenary Talk, 2009, IPRM, Newport Beach.

[Peo85] R. People, and J. Bean, “Calculation of critical layer thickness versus lattice mismatch for Ge_xSi_{1-x}/Si strained layer heterosctructures”, Appl. Phys. Lett., 1985, **47**, pp. 322-324.

[Piz98] P. Pizani, T. Boschi, F. Lanciotti, J. Groenen, R. Carles, P. Maigne, and M. Gendry, “Alloying effects on the critical layer thickness in $In_xGa_{1-x}As$/InP heterostructures analyzed by Raman scattering”, Appl. Phys. Lett., 1998, **72**, pp. 436-438.

[Rec73] I. Rechenberg, “Evolutionsstrategie. Optimierung technischer Systeme nach Prinzipien der biologischen Evolution”, Frommann Holzboog, 1973.

[Rev07] D. Revin, J. Cockburn, M. Steer, R. Airey, M. Hopkinson, and A. Krysa, “InGaAs/AlAsSb/InP strain compensated quantum cascade lasers”, Appl. Phys. Lett., 2007, **90**, 151105.

[Rez77] E. Rezek, N. Holonyak, B. Vojak, G. Stillman, J. Rossi, D. Keune, and J. Fairing, “LEP InGaPAs DH laser with multiple thin-layer (>50nm) active region”, Appl. Phys. Lett., 1977, **31**, pp. 288-290.

[Rod05] J. Rodriguez, P. Christol, L. Cerutti, F. Chevrier, and A. Joullié, “MBE growth and characterization of type-II InAs/GaSb superlattices for mid-infrared detection”, J. Crystal Growth, 2005, **274**, pp. 6-13.

[Sal02] G. Salviati, C. Ferrari, L. Lazzarini et al., “Structural characterization of InGaAs/InP heterostructures grown under compressive and tensile stress”, Appl. Surf. Sci., 2002, **188**, pp. 36-48.

[Sca02] G. Scarpa, “Design and Fabrication of Quantum Cascade Lasers”, WSI PhD Thesis, 2002.

[Sch66] F. Schäfer, W. Schmidt, and J. Volze, „Organic dye solution laser“, Appl. Phys. Lett., 1966, **9**, pp. 306-309.

[Sch07] E. F. Schubert, “Physical Foundations of Solid-State Devices”, Lecture Notes, 2007, Troy, New York,

[Sem06] M. Semtsiv, M. Wienold, S. Dressler, and W. Masselink, “Short-wavelength ($\lambda \sim 3.3$ µm) InP-based strain compensated quantum cascade laser”, Appl. Phys. Lett., 2006, **89**, 211124.

[Sha83] A. Sharma, N. Ravindra, S. Auluck, and V. Srivastava, “Temperature-dependent effective masses in III-V compound semiconductors”, Phys. Stat. Sol., 1983, **120**, pp. 715-721.

[Sha02] J. Shao, “Effective Mass and valence-band structure in $Ga_xIn_{1-x}As$/InP and $G_xIn_{1-x}P$/AlGaInP Quantum Wells”, PhD Thesis, 2002, Stuttgart.

[Sho10] J. Shorter, D. Nelson, B. McManus, M. Zahniser, and D. Milton, “Multicomponent breath analysis with infrared absorption using room-temperature quantum cascade lasers”, IEEE Sensors J., 2010, **10**, pp. 76-84.

[Sir94] C. Sirtori, F. Capasso, J. Faist, and S. Scandolo, “Nonparabolicity and a sum rule associated with the bound-to-bound and bound-to-continuum transitions in quantum wells”, Phys. Rev. B., 1994, **50**, pp. 8663-8674.

[Sir97] C. Sirtori, J. Faist, F. Capasso, D. Sivco, A. Hutchinson, and A. Cho, “Pulsed and continuous wave operation of long wavelength infrared ($\lambda = 9.3$ µm) quantum cascade lasers”, IEEE J. Quantum Electron., 1997, **33**, pp. 89-93.

[Sli07] S. Slivken, A. Evans, W. Zhang, and M. Razeghi, "High-power, continuous-operation intersubband laser for wavelengths greater than 10 μm", Appl. Phys. Lett., 2007, **90**, 151115.

[Sun05] G. Sun, R. Soref, and J. Khurgin, "Active region design of a terahertz GaN/$Al_{0.15}Ga_{0.85}N$ quantum cascade laser", Superlattices & Microstructures, 2005, **37**, pp. 107-113.

[Too08] F. Toor, D. Sivco, H. Liu, and C. Gmachl, "Effect of waveguide sidewall roughness on the threshold current density and slope efficiency of quantum cascade lasers", Appl. Phys. Lett., 2008, **93**, 031104.

[Var69] Y. P. Varshni, "Temperature dependence of the energy gap in semiconductors", 1969, Physica, 1969, **34**, pp. 149-154.

[vdW89] C. G. van de Walle, "Band lineups and deformation potentials in the model-solid theory", Phys. Rev. B, 1989, **39**, pp. 1871-1883.

[Vis96] T. Visser, B. Demeulenaere, J. Haes, D. Lenstra, R. Baets, and H. Blok, „Confinement and Modal Gain in Dielectric Waveguides", J. Lightwave. Techno., 1996, **14**, pp. 885-887.

[Vit07] M. Vitiello, T. Gresch, A. Lops, V. Spagnolo, G. Scamarcio, N. Hoyler, M. Giovannini, and J. Faist, "Influence of InAs, AlAs δ layers on the optical, electronic, and thermal characteristics of strain-compensated GaInAs/AlInAs quantum-cascade lasers", Appl. Phys. Lett., 2007, **91**, 161111.

[Viz09] A. Vizbaras, S. Katz, G. Boehm, and M.-C. Amann, „Short-injector quantum cascade laser emittingat 8 μm wavelength with high slope efficiency", IEEE Phot. Technol. Lett., 2009, **21**, pp. 1384-1386.

[Viz09b] K. Vizbaras, K. Kashani-Shirazi, and M.-C. Amann, „Simultaneous two-level lasing in GaInAsSb/GaSb strained quantum-well lasers", Appl. Phys. Lett., 2009, **95**, 071107.

[Vur01] I. Vurgaftman, J. Meyer, and L. Ram-Mohan, "Band parameters for III–V compound semiconductors and their alloys", J. Appl. Phys., 2001, **89**, pp. 5815-5875.

[Wal07] C. Walter, M. Fischer, G. Scalari, R. Terazzi, N. Hoyler, and J. Faist, „Quantum cascade lasers operating from 1.2 to 1.6 THz", Appl. Phys. Lett., 2007, **91**, 131122.

[Wan74] S. Wang, "Principles of Distributed Feedback and Distributed Bragg-Reflector Lasers", J. Quantum Electron., 1974, **10**, pp. 413-427.

[Wan01] M. Wanke, F. Capasso, C. Gmachl, A. Tredicucci, D. Sivco, A. Hutchinson, G. Chu, and A. Cho, "Injectorless Quantum Cascade Laser", Appl. Phys. Lett., 2001, **78**, pp. 3950-3952.

[Wan07] X. Wang, J. Fan, T. Tanbun-Ek, and F.-S. Choa, "Low threshold quantum cascade lasers of room temperature continuous-wave operation grown by metal-organic chemical-vapor deposition", Appl. Phys. Lett., **90**, 211103.

[Wan09] Q. Wang, C. Pflügl, L. Diehl, F. Capasso, T. Edamura, S. Furuta, M. Yamanishi, and H. Kan, "High performance quantum cascade lasers based on three-phonon resonance design", Appl. Phys. Lett., 2009, **94**, 011103.

[Wel78] W. T. Welford, and R. Winston, "The Optics of Nonimaging Concentrators", Academic Press, New York, 1978.

[Wil03] B. S. Williams, "Terahertz quantum cascade lasers", MIT PhD Thesis, 2003.

[Wil03b] B. Williams, H. Callebaut, S. Kumar, Q. Hu, and J. Reno, "3.4 THz quantum cascade laser based on longitudinal-optical phonon scattering for depopulation", Appl. Phys. Lett., 2003, **82**, pp. 1015-1017.

[Wil05] B. Williams, S. Kumar, Q. Hu, and J. Reno, "Operation of terahertz quantum-cascade lasers at 164 K in pulsed mode and at 117 K in continuous-wave mode", Optics Express, 2005, **13**, pp. 3331-3339.

[Wit07] W. Withayachumnankul, G. Png, X. Yin, S. Atakaramians, I. Jones, H. Lin, B. Ung, J. Balakrishnan, B. Ng, B. Ferguson, S. Mickan, B. Fischer, and D. Abbott, "T-Ray Sensing and Imaging", Proc. IEEE, 2007, **95**, pp. 1528-1558.

[Wit08] A. Wittmann, Y. Bonetti, J. Faist, E. Gini, and M. Giovannini, "Intersubband linewidths in quantum cascade laer designs", Appl. Phys. Lett., 2008, **93**, 141103.

[Wit09] A. Wittmann, Y. Bonetti, M. Fischer, J. Faist, S. Blaser, E. Gini, „Distributed Feedback Quantum Cascade Lasers at 9 µm Operating in Continuous Wave up to 423 K", IEEE Phot. Technol. Lett., 2009, **21**, pp. 814-816.

[Xu09] G. Xu, V. Moreau, Y. Chassagneux, A. Bousseksou, R. Colombelli, G. Patriarche, G. Beaudoin, I. Sagnes, *"Surface emitting photonic crystal mid-infrared quantum cascade lasers"*, CLEO conference, 2009, CThL7.

[Yan05] Q. Yang, C. Mann, F. Fuchs, K. Köhler, and W. Bronner, „High-temperature ($T \geq 400$ K) operation of strain-compensated quantum cascade lasers with thin InAs insertion layers and AlAs blocking barriers", J. Crystal Growth, 2005, **278**, pp. 714-717.

[Yas09] H. Yasuda, T. Kubis, P. Vogl, N. Sekine, I. Hosako, and K. Hirakawa, „Nonequilibrium Green's function calculation for four-level scheme terahertz quantum cascade laser", Appl. Phys. Lett., 2009, **94**, 151109.

[Yeh88] P. Yeh, "Optical waves in layered media", John Wiley & Sons, New York, 1998.

Appendix C - Process Details for CW Devices

Continuous wave process – Au-Heatsink

Sample cleaning ❐

~60	heißes Aceton
~20	HCl-Dip:HCl:H_20 = 1:5
~60	heißes Propanol

Siliconnitrid-Mask (PECVD – cold Deposit) ❐

Soll-Dicke: 600+ nm (~ 10 nm/min)
Carrier Cleaning & Chamber Cleaning after Deposit

Lithography (Positiv Process ~ 1.8 µm thickness AZ5214) ❐

40 s	Nitrogen-Blow
	photoresist AZ5214 on sample (vacuum at spin coater)
40 s	program 4, 3000 rpm
120 s	115° prebake on hot plate
10 min	cooling of sample

Randweg exposure & development ❐

50 s	18 mW/cm² Edge-Removal exposure ❐
40 s	Development, AZ400K:H_2O 1:4

Mesa exposure & development ❐

stripes in (0/1/-1)-direction, parallel with large „flat“; ***18 mW/cm², 5 s***

possible Masks:	QCL-WS (14/12/10 µm + Heatpads)
	QCL-cw(2) (14/12/10µm)
	QCL-cw(3) (9/7/5 µm +- Heatpads)
40 s	Development, AZ400K:H_2O 1:4

Siliziumnitrid-Mask-Etching (PECVD) ❐

0 sccm O_2, 38 sccm CF_4 => SiN-cold ~ 1.8 nm/s
SiN-hot ~ 0.35 nm/s

Photoresist-Removal ❐

5 min	Acetone (cold), spraying device
1 min	Ultrasonic, Acetone (cold), 10 % maximum power
2 min	Acetone (hot)
2 min	Propanol (hot)

Barrel-Etcher ❐

10 min / 500 ml/min O_2 / 600 W

Mesa-Etching by RIE ❐

U_{bias} ~ 280-300 V, 6 sccm Cl at *cgf of 1.7* => 1.2 µbar, ~ 11-17 nm/s
Control etching by plascal spectrometer

Mesa-Smoothening by HBr ❐

HBr : H_2O : H_2O_2	=	20 : 60 : 2	(for small mesas)
HBr : H_2O : H_2O_2	=	20 : 120 : 2	(for small mesas + heatpads)

~ 8-12 nm/s GaInAs & 10-14 nm/s InP etch rates
(etch depth depends on desired underetch and RIE etch depth)

Direkt nach letztem Ätzen in die PECVD !!!

Siliziumnitrid-Mask Removal (PECVD) ❐

0 sccm O_2, 38 sccm CF_4 => SiN-cold ~ 1.8 nm/s
SiN-hot ~ 0.35 nm/s

Siliziumnitrid-Passivation (PECVD) ❐

12 sccm SiH_4, 60 sccm N_2 => SiN-cold ~ 10 nm/min
SiN-hot ~ 5.2 nm/min (105 % T_{ist})
Thickness: 400 nm (depends on wavelength and voltage drop)

Siliziumdioxid-Sputtering ❐

1200 V, => SiN-cold ~ 7.5 – 9.5 nm/min

Thickness: 250 nm (depends on wavelength and voltage drop)

Lithography (Positiv Process ~ 3.0 µm thickness AZ4533) ❐

40 s Nitrogen-Blow
photoresist AZ4533 on sample (vacuum at spin coater)
40 s program 4, 3000 rpm
120 s 100° prebake on hot plate
10 min cooling of sample

Randweg exposure & development ❐

50 s 18 mW/cm² Edge-Removal exposure ❐
70 s Development, AZ400K:H_2O 1:4

Contact Windows exposure & development ❐

Alignment according to mesas & 1st and 4th Cross,
parallel with large „flat“; ***18 mW/cm², 5 s***

possible Masks: QCL-WS (7/5/3 µm windows)
QCL-cw(2) (6/4/2 µm windows)

90 s + 40 s Development, AZ400K:H_2O 1:4

Contact Window Etching (PECVD) ❐

0 sccm O_2, 38 sccm CF_4 => SiN-cold ~ 1.8 nm/s
SiN-hot ~ 0.35 nm/s
SiO ~ 0.11 nm/s

(very slow, but lowest etch rate for the photoresist AZ4533 ~ 0.35 nm/s)

Photoresist-Removal ❐

5 min Acetone (cold), spraying device
1 min Ultrasonic, Acetone (cold), 10 % maximum power
2 min Acetone (hot)
2 min Propanol (hot)

Barrel-Etcher ❐

10 min / 500 ml/min O_2 / 600 W

Lithography (Negativ Process ~ 1.8 µm thickness AZ4533) ❐ => for Lift-off

40 s Nitrogen-Blow
photoresist AZ5214 on sample (vacuum at spin coater)
40 s program 4, 3000 rpm
90 s 90° prebake on hot plate
10 min cooling of sample

Randweg exposure & development ❐

50 s 18 mW/cm² Edge-Removal exposure ❐
30 s Development, AZ400K:H_2O 1:4

Metal-Liftoff exposure & development ❐

Alignment according to mesas & 2nd and 3rd Cross,
parallel with large „flat“; ***18 mW/cm², 2.2 s***

possible Masks: QCL-cw(2) *(large stripes covering mesas)*

45 s 135° post bake
20 s Flood-Exposure ***18 mW/cm²,***

40 s + 20 s Development, AZ400K:H_2O 1:4

Barrel-Etcher ❐

30 s / 100 ml/min O_2 / 100 W (removes roughly 50 nm)

VT-118 Ti/Pt/Au Evaporation ❐

HCl-Dip directly before evaporation (1:4 HCl:H_2O)
40 nm Ti, 40 nm Pt, 400 – 600 nm Au (30° rotating until 60 % of thickness, then 0°)

Metal-Liftoff ❐

20 min Acetone (cold), soaking in
1 min Ultrasonic, Acetone (cold), 10 % maximum power
5 min Acetone (cold), spraying device
Repeat step 2 and 3 until all mesas are separated
2 min Acetone (hot)
2 min Propanol (hot)

Lithography (Positiv Process ~ 7 µm thickness AZ4533) ❐

40 s Nitrogen-Blow
photoresist MAP1275 on sample (vacuum at spin coater)
40 s program 4, 3000 rpm
10 min 100° prebake on hot plate / oven
10 min cooling of sample

Randweg exposure & development ❐

99 s 18 mW/cm² Edge-Removal exposure ❐
100 s Development, AZ400K:H_2O 1:4

Electroplating Windows exposure & development ❐

Alignment according to mesas & 1st and 4th Cross,
parallel with large „flat“; ***18 mW/cm², 5 s***

possible Masks: QCL-cw(2) (galvanic, 4-3-2 mm)
QCL-cw(3) (galvanic, 4-4-4-2 mm)
60 s + 40 s Development, AZ400K:H_2O 1:4

Barrel-Etcher ❐

3 min / 100 ml/min O_2 / 150 W

Electroplating ❐

30 min	30 min	30 min	30 min	
0.5 mA	1.0 mA	3.0 mA	4.0 mA	=> ~ 5-6 µm Au-.heatsink

(current per quarter of 2” wafer)

Photoresist-Removal ❐

4 min Acetone (cold), spraying device
4 min Acetone (hot)
2 min Propanol (hot)
(no Barrel-Etcher!)

Wafer-thinning ❐ (down to 120-140 µm)

HBr+Methanol, 40 rpm, 1 drop/s of 5 % HBr-solution => ~ 6-8 µm/min

n-Anlage Ge/Au/Ni/Au Evaporation ❐

HCl-Dip directly before evaporation (1:4 HCl:H_2O)
13 nm Ge, 33 nm Au, 20 nm Ni, 250 nm Au

Appendix D - Evolution Algorithm

The original evolution algorithm contains far more than thousand lines of code, therefore the work principle shall be explained in a shorter text.

"Get Scan Parameters"

At the begin of the evolution algorithm, the program reads the limits of each parameter like wavelength (maximum and minimum), upper state lifetime (minimum), dipole matrix element (minimum), lower laser states lifetimes (maximum), injection lifetime (maximum), period length (maximum). Besides these parameters, also the depletion and injection scheme can be predefined: The number of states in resonance above the upper laser state, offering parallel injection paths, or the number of states being used for resonant depletion for example.

"Get Structure Parameters"

The next step reads in the original structure and the defined upper and lower limits of each layer, regarding thickness and material composition. These limitations are critical and should be chosen carefully. The random deviation of material compositions is problematic towards growth within *MBE* systems, as compositions cannot be changed from one layer to another randomly. Therefore a few predefined materials were chosen, which can be grown with good interfaces and the layer thicknesses were varied instead.

"Create 1st Parent Generation"

For each layer, a purely random value regarding thickness and material composition will be chosen within the predefined upper and lower boundaries. This step is repeat and all different layer sets are saved until the whole parent generation is created. Additionally an array for saving the quality of each structure and the corresponding standard deviation is predefined.

"Call Routines for Evolution Scan"

Cycling through all generations, the following steps are repeated as following:

"Mutate"

As input for this subroutine the upper and lower boundaries for each layer's thickness and composition are required. Randomly any parental structure is chosen and each of its layers randomly deviated following a Gaussian distribution, according to the standard deviation of its parental structure. The algorithm seemed most successful when the number of mutants exceeded the number of parents by a factor of 2 at least, meaning that each parent creates multiple deviations from himself.

"Evaluate Parents"

The program cycles through all parental structures at first, creates the structure based on their layer set and calculates the corresponding modes, using a simple one-dimensional Schrödinger Solver. Then it evaluates all parental structures step by step, jumping to the next structure with one parameter being out of the limitations for saving computational time. The sequence for checking the quality is the following:

1. Check confined sates, retrieve all states which are confined and save them
2. Locate all confined states to their corresponding period
3. Check if the strain is balanced or compensated sufficiently
4. Check for upper lasing level in first period with correct transition energy
5. Calculate dipole matrix elements (QR 4)
6. Check for sufficient high dipole matrix element
7. Calculated LO-phonon scattering times
8. Check upper laser state lifetime, ignore unconfined states (QR 3)
9. Check depletion scheme for sufficient fast depletion
10. Check depletion scheme for resonant tunneling (QR 2)
11. Calculate Interface Scattering for upper laser level and ground state
12. Check injection behavior (QR 1)

According to the corresponding schemata a quality group (*QR*) between one and five can be attributed to each structure. While group five indicates that not a single parameter for the transition was met, group one shows a working device. From quality group three or better, a quality factor according to equatition 2.1.14 can be calculated. Every structure in group one with a quality factor higher than all previous ones gets instantaneously saved in an independent structure file.

"Sort Quality"

This small routine sorts the layer sets according to their group and then by their quality factor.

"Evaluate Mutants & Sort Quality"

The program cycles now through all mutant structures similar to the previous cycling through all parental structures. Afterwards it sorts them into the same list than the parental structures, also according to their group and their quality factor.

"Survival of the Fittest"

At this step, the best structures corresponding to the number of parents per generation are taking as next generation. For each structure which was already a parental structure before, the standard deviation for mutation is decreased by the factor of 1.22, while for each mutant who turned into a parental structure, the standard deviation of mutation is increased by a factor of 1.22. The reason for this

change can be explained by the strategy, that either mutation is successful and shall be expanded further or that the optimum is close to the parental structure. To avoid finding only local minima, the number of parents and mutants per generation has to be sufficiently large, for small deviations and optimization around 20’000 for parents and 60’000 for mutants are suitable, while larger boundaries will require larger generations.

Appendix E - Detailed Dielectric Function

In chapter 2.4 equation 2.2.15 is used for calculating the complex refractive index. This equation is suitable for the mid infrared range, while it needs to be expanded for frequencies close to the phonon frequencies by their linewidth. In general, the frequency dependent dielectric function can be written as:

$$\varepsilon(\omega) = 1 + \chi(el) + \chi(ion)$$

with $\chi(el)$ and $\chi(ion)$ being the susceptibility of the electronic and ionic polarization, respectively. While the electronic polarization can be seen as static for the mid and far infrared range, the ionic polarization strongly changes. This can be expressed by [Gro04]

$$\chi(ion) = \frac{\omega_T^2}{\omega_T^2 - \omega^2 - j\gamma\omega}\left(\varepsilon_{(0)} - \varepsilon_{(\infty)}\right)$$

using a damped oscillator approximation. This approximation can be transformed into the first part of the used dielectric function, yielding

$$\varepsilon(\omega) = \varepsilon_{(\infty)} \cdot \left(\frac{\omega_L^2 - \omega^2 - j\gamma\omega}{\omega_T^2 - \omega^2 - j\gamma\omega}\right)$$

which can be resolved into a real and an imaginary part.

For doped layers, a simple drude expression can be added as explained in chapter 9 [Pal85], which leads to the following expression

$$\varepsilon(\omega) = \varepsilon_{(\infty)}\left[\left(\frac{\omega_L^2 - \omega^2 - j\gamma\omega}{\omega_T^2 - \omega^2 - j\gamma\omega}\right) - \frac{\widetilde{\omega}_p^2}{\omega^2\eta}\left(1 + \frac{j}{\omega\tau}\right)\right]$$

yielding

$$\varepsilon'(\omega) = \varepsilon_{(\infty)}\left[\frac{(\omega_L^2 - \omega^2)(\omega_T^2 - \omega^2) + \gamma^2\omega^2}{(\omega_T^2 - \omega^2)^2 + \gamma^2\omega^2} - \frac{\widetilde{\omega}_p^2}{\omega^2\eta}\right]$$

and

$$\varepsilon''(\omega) = \varepsilon_{(\infty)}\left[-\gamma\omega\frac{(\omega_L^2 - \omega_T^2)}{(\omega_T^2 - \omega^2)^2 + \gamma^2\omega^2} - \frac{\widetilde{\omega}_p^2}{\omega^3\tau\eta}\right]$$

as real and imaginary part.

For estimating the complex refractive index of silicon dioxide and silicon nitride, their wavelength dependence reflectance was measured (see figure 1). In combination with an fitting algorithm, the real and imaginary part can be determined. The reflectivity measured with the silicon

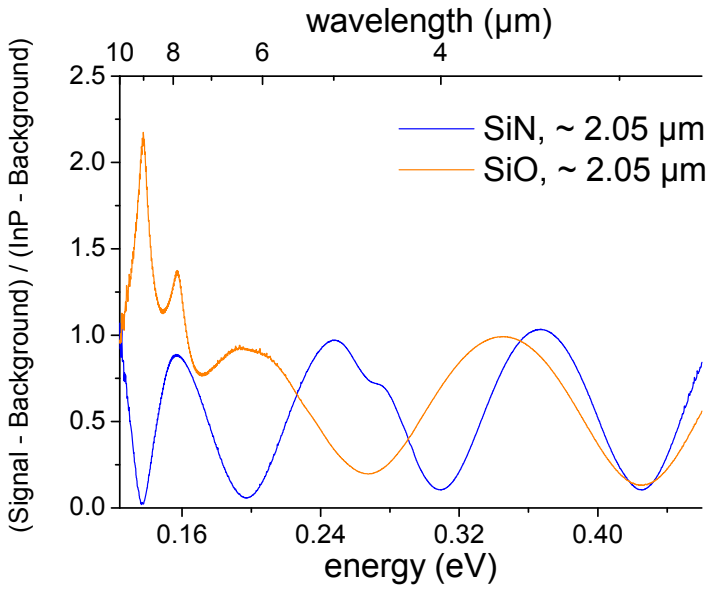

Fig 1: measured reflectivities for silicon dioxide and silicon nitritde in the mid infrared range

dioxide sample shows two peaks, indicating to different ionic polarization modes. Both of them are attributed to the Si-O-Si stretching vibrations, but different if the bond is facing a void of the amorphous material or not [Kyu00].

With two resonances for different bonds, the complex dielectric function had to be expanded with a second damped oscillator, leading to the following approach

$$\varepsilon(\omega) = \varepsilon_{(\infty)} + \frac{\omega_{T1}^2}{\omega_{T1}^2 - \omega^2 - j\gamma_1\omega}\left(\frac{\omega_{L1}^2}{\omega_{T1}^2}\varepsilon_{(\infty)} - \varepsilon_{(\infty)}\right) + \frac{\omega_{T2}^2}{\omega_{T2}^2 - \omega^2 - j\gamma_2\omega}\left(\frac{\omega_{L2}^2}{\omega_{T2}^2}\frac{\omega_{L1}^2}{\omega_{T1}^2}\varepsilon_{(\infty)} - \frac{\omega_{L1}^2}{\omega_{T1}^2}\varepsilon_{(\infty)}\right)$$

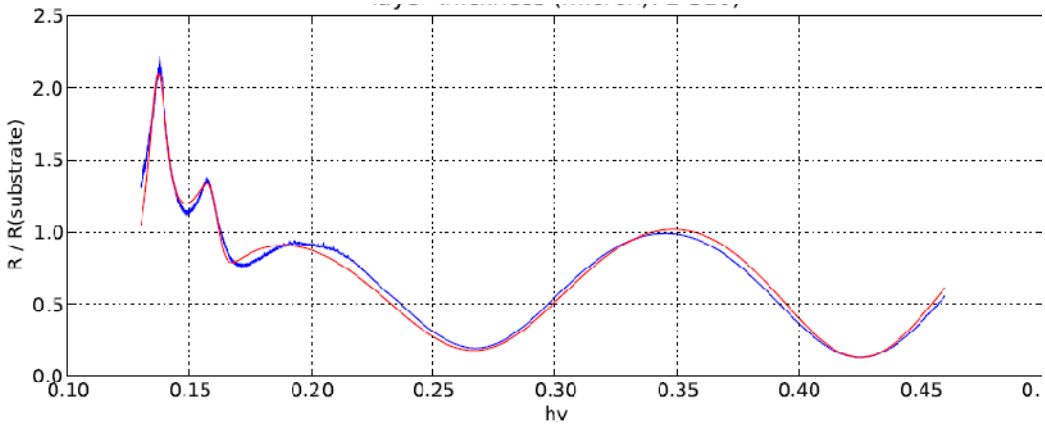

Fig 2: calculated reflectance (red) and measured reflectance (blue). The calculation model is using an asymmetric linewidth with 10 % difference.

which can be used for determining the real and imaginary part of the refractive index by fitting the equation to the measured reflectance (see figure 2).

The estimated real and imaginary parts are shown in figure 3, and the corresponding waveguide losses in figure 4. As narrow ridges can reach lateral confinement factors up to 1 %, leading to very high additional waveguide losses.

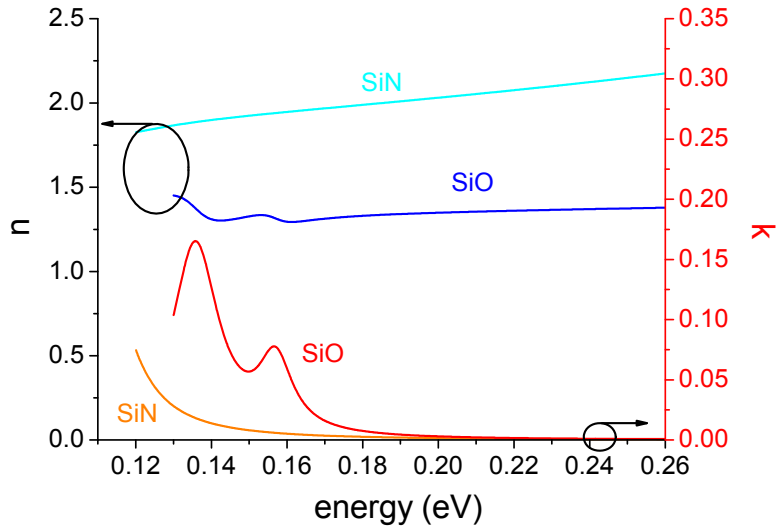

Fig 3: real and imaginary part for amorphous silicon dioxide and nitride

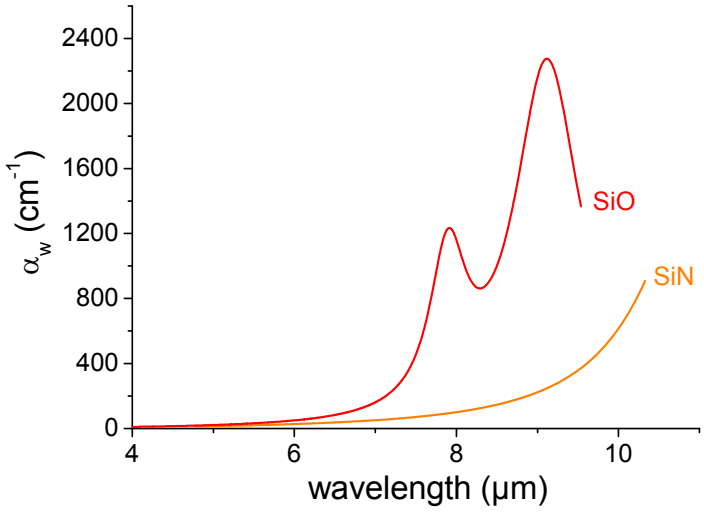

Fig 4: waveguide losses for silicon dioxide and silicon nitride

Appendix F – Preexaminations in Related Fields

GaSb based devices

First device tests

Since the first success of quantum cascade lasers, they were made out of AlGaInAs grown on InP. Although the material quality is not as good as the AlGaAs/GaAs system, the advantages as lower effective mass and larger conduction band offset, easily outclass the disadvantages. On the other side GaSb based devices, using InAs(Sb) as quantum well, offer an even lower effective mass and larger conduction band offset and should therefore perform even better. The growth of GaSb/InAs interfaces on the other side is very complex, as the group V-element switches at every interface, and only a few groups have worked on antimony containing quantum cascade lasers so far [Dev07][Rev07], none of them reaching the performance of InP-based devices.

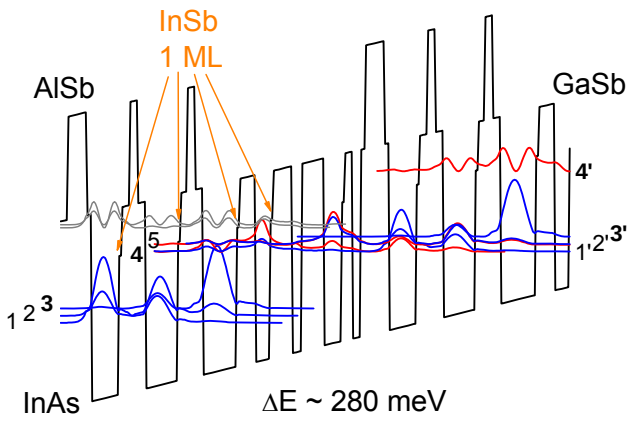

Fig 4-6-1: first design for GaSb based injectorless quantum cascade lasers. InSb monolayers are indicated by orange arrows.

Figure 4-6-1 shows the first injectorless design, using AlSb/GaSb/InAs as layers. Additionally one monolayer of InSb was added at the most important InAs-GaSb interfaces to improve the interface quality and prevent segregation as shown for mid-infrared detectors [Rod05]. The InSb monolayers also worked for strain compensation, as InAs was used as well material. The layer sequence is **0.5**/***2.0***/**0.5**/3.5/*0.34*/**1.0**/***0.8***/**1.0**/4.1/*0.34*/**0.7**/***1.0***/**0.7**/4.6/*0.34*/**2.0**/1.8/*0.34*/**2.4**/1.3/**2.8**/2.2/*0.34*/**1.0**/1.0 in nm, with **GaSb in bold**, ***AlSb in bold and italic***, InAs in regular and *InSb in italic* fond. The doping sheet density was similar to other GaSb-based devices with $1.8 \cdot 10^{11}$ cm^{-2}. The simulation parameters of this design yielded a dipole matrix element of 2.24 nm, an upper laser lifetime around 3.7 ps and an emission energy 280 meV. In combination with the short period of 36.6 nm, the quality factor was larger than 100, which is more than a factor of two in comparison to the best InP based design. To avoid losses into side valleys, the upper laser levels are located more than 50 meV below the InAs *L*-valley. The lowest depletion level is 50 meV above the GaSb valence band (see subchapter 2.2.1) to avoid any effects from the type-II band alignment.

The active region consisted of 35 repeats, with an overall thickness of 1.28 µm. A 200 nm thick GaSb cladding layer and 2.0 µm of $Al_{0.5}Ga_{0.5}AsSb$ as waveguide were added on both sides of the active region. Finally 500 nm of InAsSb, highly doped, were used as contact layer. Between all these layers,

superlattices similar to those used in GaSb-VCSELs [Die07] were used. The process was performed by reactive ion etching, as no sufficiently isotropic etch solution for the complete AlGaInAsSb system was found. The passivation consisted of more than 1.0 µm of sputtered silicon dioxide, followed by the top

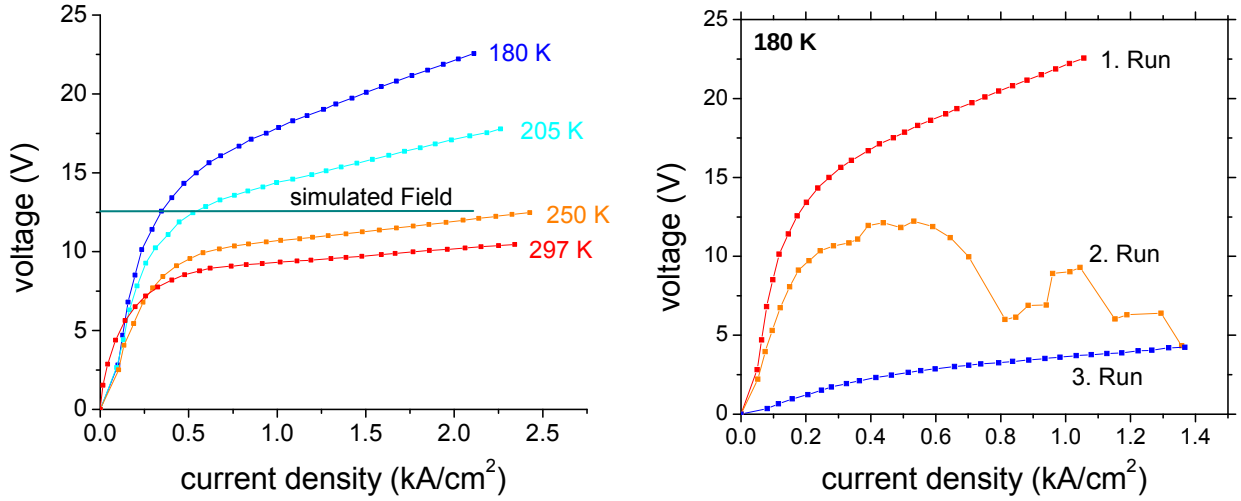

Fig 4-6-2: voltage-current density characteristics of a GaSb based injectorless quantum cascade laser versus temperature (left) and the corresponding segregation behavior (right).

metallization of Ti/Pt/Au. After mechanical thinning, a Ti/Pt/Au back side contact was used, as the substrate is relatively high doped with $5 \cdot 10^{18}$ cm^{-3}.

Figure 4-6-2 shows the VI curves over temperature. Below 180 K the increase in voltage was drastically larger and caused immediate device failures. Above 180 K, the devices worked up to 2.5 kA/cm^2, but many were failing at even lower current densities. The right side of figure 4-6-2 shows the same device measured at 180 K (1st run), kept running until the first indication of upcoming device failure was visible and instantaneously measured (2nd run). Afterwards the ohmic behavior of the contacts and waveguide remained stable (3rd run). As these changes occurred under current and over some minutes, they were attributed to changes within the active region instead of insulation failures, which occur abrupt and fast. Lasing

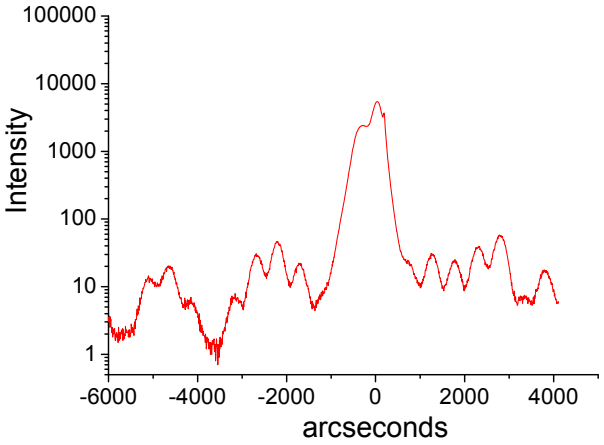

Fig 4-6-3: XRD measurement of GaSb device A2242, using a design similar to the one shown in figure 4-6-1.

was not observed in any case, but it has to be mentioned that all working GaSb based devices exhibit threshold current densities between 1.8 kA/cm^2 and more than 5 kA/cm^2 at 180 K [Dev07].

When investigating the morphology of the GaSb growth by *XRD,* as shown in figure 4-6-3, it becomes obvious why no lasing can be observed.

Further device generations

From the first tests with complex designs but only binary materials, it became obvious that either very intense investigation on optimized growth parameters had to be done, or that already known compositions had to be used. The material composition of $In_{0.5}Ga_{0.5}AsSb$ has shown strongly decreased intersubband scattering rates [Viz09b] and therefore could be interesting for quantum cascade lasers. In combination with GaSb barriers, segregation effects, like the first devices have shown, should be strongly reduced. This segregation behavior was also observed in bulk materials under growth parameters [Die07], similar to those used in the previous devices.

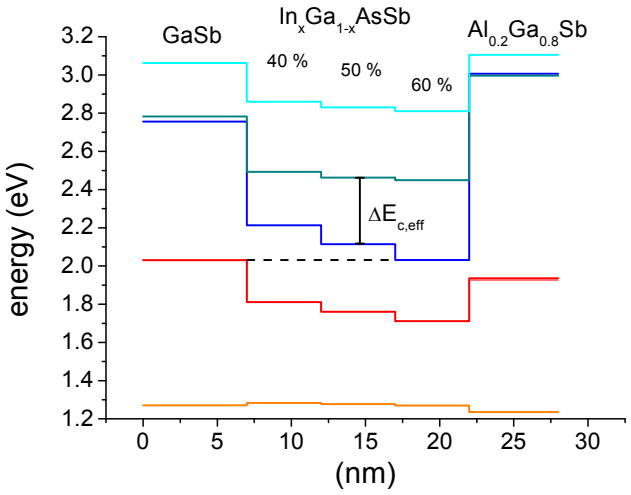

Fig 4-6-4: materials using $In_{0.5}Ga_{0.5}AsSb$ as well material and GaSb as barrier. The broken gap alignment disappears for compositions with more than 40 % Ga-content.

Figure 4-6-4 shows a more simplified material system. When using $In_{0.5}Ga_{0.5}AsSb$ and GaSb only, the broken gap alignment disappears and a remaining effective conduction band offset of 350 meV remains. When designing devices with states above the InGaAsSb *L*-valley, they should still work but will most likely suffer additional current losses.

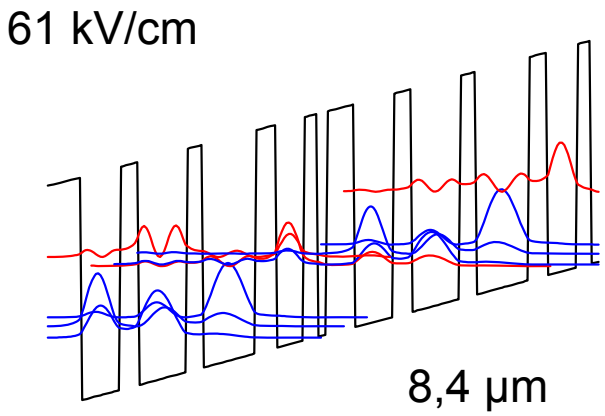

Fig 4-6-5: simple 5-level injectorless design, using $In_{0.5}Ga_{0.5}AsSb$ and GaSb.

Figure 4-6-5 shows a very simple design of an injectorless quantum cascade laser, which uses these materials. The layer sequence is **3.5**/4.8/**2.4**/6.1/**2.1**/6.8/**2.4**/3.6/**1.7** /1.0 in nm, with $In_{0.5}Ga_{0.5}AsSb$ in regular and **GaSb in bold**.

The challenges for GaSb based devices are the growth of good interfaces of materials with different group-V elements or group-V

ratios. Therefore future development on quantum cascade lasers using GaSb as substrate is much more an expitaxial work than anything else. Additionally the material parameters which are used for simulations are less well known than they are for GaInAs.

Far infrared devices

Besides working in the mid infrared range, two different concepts on realizing terahertz emission from quantum cascade lasers were investigated: The direct transition and the difference frequency generation. The first work was carried out with the concept of difference frequency generation by the diploma student A. Vizbaras, in which the general theory was gathered. In cooperation with M. Belkin, a new concept achieved THz emission with higher conversion efficiencies than previous concepts offered [Ada10]. Parallel to this, some first tests on quaternary barriers with GaInAs wells were carried out, which were unsuccessful and showed many possible obstacles for lasing operation. These obstacles shall be briefly described, while the successful difference frequency concept is a main topic of the PhD thesis of A. Vizbaras, who contributed most.

Far infrared devices using AlGaInAs/GaInAs on InP

Most successful designs for direct terahertz generation [Kum09][Bel08] are grown on GaAs, using $Al_{0.15}Ga_{0.85}As$ as barrier material. This material has some advantages in growth, like the perfect lattice matching of the GaAs well and only slight strain in the barrier material. The strain balancing is crucial for terahertz devices, as they require active regions being around 10 µm thick, consisting of a superlattice. Another advantage and reason for success, is the low effective mass, resulting in low waveguide losses, while the binary, ternary superlattice AlGaAs has acceptable heat conductivity.

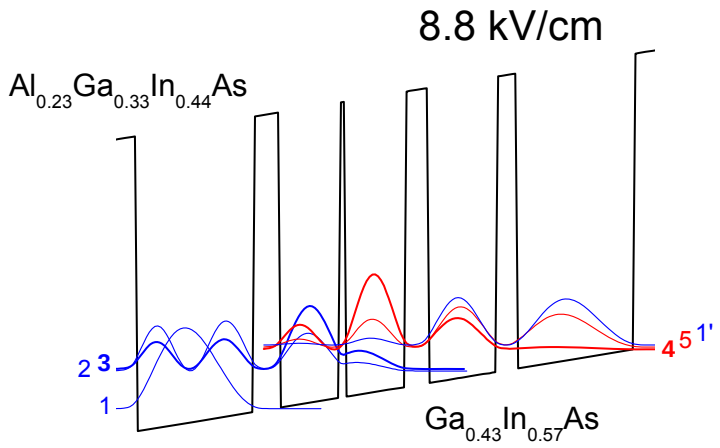

Fig 4-5-1: active region of a quaternary-ternary strain balanced terahertz sample with the layer thicknesses in nm being: **3.3**/21.8/**4.4**/11.2/**1.3**/10.6/**4.2**/13.0 indicating barriers in bold.

GaInAs as well material is offering only one advantage: its lower effective mass, which results into a larger gain coefficient, which increases faster than the corresponding waveguide losses (see equation 2.1.13). Therefore possible growth issues and device designs were investigated, and worked out in detail by the two diploma students V. Doering [Doe09] and G. Bracher [Bra09].

At the begin of their thesis's, there was no measurement setup for the far infrared, no metal-metal process established and growth of thick superlattice structures never done before at this chair. As preliminary investigations, the costs also had to be kept low. Therefore the devices could only be characterized by a pyro-electric detector instead of a silicon bolometer, disabling any chance on measuring electroluminescence.

From the growth point of view AlGaInAs/GaInAs showed serious problems, as all samples grown on n- substrates showed cross hatch. Figure 4-5-1 shows a typical design of a quaternary-ternary device, which was adapted from the successful four-well design by Williams et al. [Wil05]. Even lattice matched AlInAs/GaInAs showed massive growth defects, as slight mismatches in calibration accumulate enough strain over 10 µm of growth to break. Growing finally on n+ substrates solved this problem, forcing the devices to be processed into metal-metal waveguides only, instead of single plasmonic waveguides. Most metal-metal bonding processes reach areas of 5 times 5 mm in area, drastically reducing the yield. Besides the pellet-like lower metal waveguide, which assumable has very high waveguide losses, also bond wires for example can influence the waveguide behavior, due to the microstripe design. Therefore further optimization has to be done on the metallization and integration of contacts into the process design is strongly recommended.

From the current point of view, the difference frequency concept shows much more promising in achieving room temperature operation with mW output power, as already weak room temperature operation was reported [Bel08b]. The concept of direct generation showed an increase in maximum temperature of operation from 164 K in 2005 up to 186 K in 2009 for GaAs devices. This indicates the general problems these devices experience, in terms of reproducibility and reliability. Even a repeated process with the same growth run, can result in record high temperature of 178 K [Bel08] on one side, or not even reach liquid nitrogen temperature [Bel09o] on the other side. Therefore further research in the direct generation was stopped and all efforts were focused on the difference frequency generation.

Appendix G - Publications

High-performance injectorless quantum cascade laser emitting below 6 µm

Appl. Phys. Lett., **94**, 151106, (2009)

S. Katz | A. Vizbaras | G. Boehm | M. C. Amann

Injectorless quantum cascade laser operating in continuous wave above room temperature

Semicond. Sci. Technol., **24,** 122001, (2009)

S. Katz | A. Vizbaras | G. Boehm | M. C. Amann

Injectorless Quantum Cascade Lasers for the Mid-Infrared

Radio Science Bulletin, 2008, **326**, p. 20-28

M. C. Amann | S. Katz

Low-threshold Injectorless Quantum Cascade Laser with Four Material Compositions

Electron. Lett., 2008, **44**, pp. 580-581

S. Katz | G. Boehm | M. C. Amann

Continuous wave operation of injectorless quantum cascade lasers at low temperatures

Appl. Phys. Lett., 2008, **92**, 181103

S. Katz | A. Friedrich | G. Boehm | M. C. Amann

Conferences & Workshops

High Power Injectorless Quantum Cascade Laser Structure in the 6.0 µm Wavelength Range

Proc. of CLEO, 2009, Baltimore

S. Katz | G. Boehm | M. C. Amann

Low-threshold Injectorless quantum cascade lasers

International Quantum Cascade Laser School and Workshop, Monte Verita, Swiss (2008)

S. Katz | M. Maier | G. Boehm | M. C. Amann

Injectorless quantum cascade lasers with threshold current densities below 500 A/cm²

Proc. of 21st ISLC, Sorrent, Italy (2008)

S. Katz | G. Boehm | M. C. Amann

Dual wavelength emission in injectorless quantum cascade lasers

Proc. of 20th IPRM, 2008, Versailles

S. Katz | M. Maier | G. Boehm | M. C. Amann

Contributed Publications & Conferences

Terahertz sources based on difference-frequency generation near exit facets in dual wavelength mid-infrared quantum cascade lasers

Proc. of CLEO, 2010, San Jose **(submitted)**

R. Adams | A. Vizbaras | C. Grasse | S. Katz | G. Boehm | M. Jang | M. C. Amann | M. Belkin

THz quantum cascade laser sources for room-temperature operation

The 40th winter colloquium on the **Physics of Quantum Electronics (PQE-2010)**, January 3-7, Snowbird, Utah, USA (invited talk) (2010).

M. A. Belkin | R. W. Adams | A. Vizbaras | M. Jang | C. Grasse | S. Katz | G. Boehm | M. C. Amann

Highly Temperature-Stable, Long Wavelength Short-Injector Quantum Cascade Laser

10th International Conference on Intersubband Transitions in quantum Wells (**ITQW-2009**), September 6th - 11th, Montreal, Canada, (2009).

A. Vizbaras | S. Katz | G. Boehm | M. C. Amann

Short-Injector Quantum Cascade Laser Emitting at 8 µm Wavelength With High Slope Efficiency

IEEE PHOTONICS TECHNOLOGY LETTERS, **Vol. 21**, No. 19, pp. 1384-1386, (2009).

A. Vizbaras | S. Katz | G. Boehm | M. C. Amann

Al(In)As-(Ga)InAs strain-compensated active regions for injectorless quantum cascade lasers

J. Crystal Growth, 2009, 311, pp. 1932-1934

G. Boehm | S. Katz | R. Meyer | M. C. Amann

Acknowledgments

Without the help of many people, this work wouldn't have been possible.

First of all, I wish to thank Prof. Amann for the opportunity to accomplish my thesis at his chair within the group of E26. Besides this, he was always encouraging me to go further and look into relevant details without losing the scope of the thesis. With many intense discussions during our meetings, he helped to improve the understanding of physics and devices wherever it was necessary.

My thanks also go to Gerhard Boehm for all the wafers he grew for me, some with helpful questions beforehand to ensure good quality and bring together his empirical knowledge of molecular beam epitaxy with my theoretical understanding of the devices. Thanks for the Epi.

I shared a lot of good laughter with my colleague Augustinas Vizbaras, who joined this group as diploma student on terahertz emission by different frequency generation. A topic I had started without a clue about the complexity, which he managed to get running now as PhD student. It was a very good and warm cooperation in our group, always helping

Besides Augustinas, I also want to thank the colleague Roland Enzmann for all his warm words, the opportunity of getting coffee in his office and the good hours outside the institute. When things go wrong, he always could find some words worth a smile.

Dr. Ralf Meyer was always supporting and interested into the work of quantum cascade lasers. His helping mind always found some pool of money, when equipment was needed, which strongly helped improving measurement and device setups.

I also want to thank my other colleagues, Alex Bachmann, Michael Müller, Christian Grasse, Tobias Gründl, Kristijonas Vizbaras and Shamsul Arafin, who contributed to a motivating and convenient work atmosphere at our chair. There was always a helping hand or a second thought, when required.

One should not forget the helpful hands of our technical staff, who keep the labs running. Thanks go to Sepp Grottenthaler, for his help with the dry etching system and all other pumps, pipes and valves. Elke Thiel, Linda Mora and Edith Sckopke were always kindly helping with the daily problems within the cleanroom or outside.

Besides this, I want to thank my family and my wife Claudia for supporting me all time.

It was very pleasant and interesting time, during which I have learned a lot, from quantum mechanics to the maintenance of dry etching systems, and some lessons about life.